INSTITUTE OF PHYSICS
WROCLAW UNIVERSITY OF TECHNOLOGY

Paweł Potasz

Electronic and optical properties of graphene nanostructures

This PhD thesis was prepared under supervision of

prof. dr hab. Arkadiusz Wójs
Institute of Physics, Wroclaw University of Technology,
Wroclaw, Poland

prof. Paweł Hawrylak
Institute for Microstructural Sciences, National Research
Council, Ottawa, Canada

Wrocław 2012

Acknowledgments

I would like to thank my supervisors, prof. Arkadiusz Wójs and prof. Paweł Hawrylak, for giving me the opportunity to work in a very interesting field of research.

I acknowledge Paweł Hawrylak for support and patience. I am grateful for giving me a chance to work in Ottawa. It was crucial experience for my progress.

I also wish to thank my collaborators, Devrim Güçlü, Marek Korkusiński and Oleksander Voznyy. To work with you has been a real pleasure to me. Especially, I would like to thank Devrim for teaching me so much in our joint research. I appreciate your time and effort. I enjoy working with you.

Finally, I would like to thank my family, and all others who support me during that time.

Contents

1 Introduction **3**

1.1 Graphene - two-dimensional crystal 3

1.1.1 Introduction 3

1.1.2 Fabrication methods 10

1.1.3 Mechanical properties 13

1.2 Electronic band structure 14

1.2.1 Tight-Binding model 14

1.2.2 Effective mass approximation 18

1.3 Graphene nanostructures 20

1.3.1 Fabrication methods 20

1.3.2 The role of edges 22

1.3.3 Size quantization effects 24

2 Single particle properties of graphene quantum dots **25**

2.1 Size, shape and edge dependence of single particle spectrum . . 25

2.1.1 Tight-Binding model 25

2.2 Triangular graphene quantum dots with zigzag edges 29

2.2.1 Energy spectrum 29

2.2.2 Analytical solution to zero-energy states 31

2.2.3 Classification of states with respect to irreducible representations of C_{3v} symmetry group 36

2.3 Triangular mesoscopic quantum rings with zigzag edges 44

2.3.1 Energy spectrum 44

2.4 Hexagonal mesoscopic quantum rings 45

2.4.1 Energy spectrum 47

3 Electron-electron interaction in gated graphene nanostructures **53**

3.1 Introduction 53

3.2 Many-body Hamiltonian 54

3.3 Two body scattering - Coulomb matrix elements 55
3.4 Mean-Field HF approximation 56
3.4.1 Hartree-Fock method - application to graphene nanostructures 58
3.4.2 Hubbard model - mean-field approximation 60
3.5 Configuration interaction method 61
3.5.1 Creation of many-body basis 62
3.5.2 Construction of Hamiltonian matrix 64
3.5.3 Diagonalization methods for large matrices 69
3.6 TB+HF+CI method 76

4 Magnetic properties of gated graphene nanostructures 79
4.1 Triangular graphene quantum dots with zigzag edges 79
4.1.1 Analysis as a function of filling factor 79
4.1.2 Analysis as a function of size 83
4.1.3 Comparison of Hubbard, extended Hubbard and full CI results 87
4.1.4 Edge reconstruction effects using DFT 92
4.2 Triangular mesoscopic quantum rings with zigzag edges 99
4.2.1 Properties of the charge neutral system 99
4.2.2 Analysis as a function of filling factor 103
4.3 Hexagonal mesoscopic quantum rings 106
4.3.1 Analysis as a function of size 106
4.3.2 Analysis as a function of filling factor 108

5 Optical properties of graphene nanostructures 111
5.1 Size, shape and type of edge dependence of the energy gap . . . 111
5.2 Optical joint density of states 113
5.3 Triangular graphene quantum dots with zigzag edges 115
5.3.1 Excitons in graphene quantum dots 115
5.3.2 Charged excitons in interacting charged quantum dots . 117
5.3.3 Terahertz spectroscopy of degenerate shell 119

6 Conclusions 123

Chapter 1

Introduction

1.1 Graphene - two-dimensional crystal

1.1.1 Introduction

Graphene is a one-atom thick planar structure of carbon atoms arranged in a honeycomb crystal lattice. It plays an important role since it is a basis for an understanding of the electronic properties of other allotropes of carbon. Graphene can be rolled up along a given direction forming nanotubes, a 1D material, or wrapped up into a ball creating fullerene, a 0D material. It is worth to note that the Nobel Prize in Chemistry in 1996 was awarded jointly to Robert F. Curl Jr., Sir Harold W. Kroto and Richard E. Smalley "for their discovery of fullerenes". Graphite is a 3D anisotropic crystal, consisting of graphene layers bonded by weak van der Waals forces. A separation between graphene adjacent sheets, 0.335 nm is much larger than a distance between neighboring carbon atoms in a honeycomb lattice, 0.142 nm.

A research on graphene has a long history. One of the first papers was written by P. R. Wallace in 1946 at the National Research Council of Canada [1]. It regarded a band structure of graphite, including a single layer - graphene. It was shown that graphene exhibits semi-metalic behavior with an unusual low energy linear dispersion of quasi-particle energy as a function of wave vector. This behavior is in close analogy to the dispersion of massless relativistic particles. A theory of the electronic properties of graphite was further developed by Slonczewski, McClure and Weiss [2, 3]. Semenoff and Haldane discussed an analogy of graphene to (2+1) dimensional quantum electrodynamics (QED) [4,5]. Experimental attempts were performed to separate layers in graphite through intercalation [6–9]. The electronic properties of graphite intercalation compounds were studied by a number of groups [10–12]. Theory

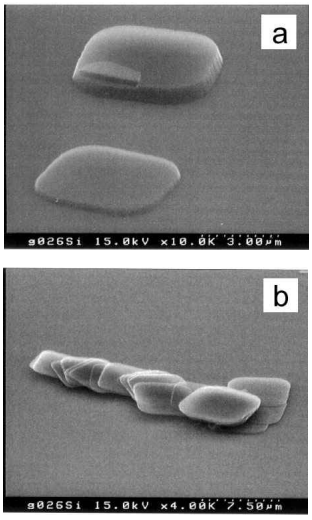

Figure 1.1: SEM images of thin graphite plates on the Si(001) substrate. Reprinted from Ref. [27].

of optical absorption of graphene was developed [13] and compared with experiment [8,13]. Effects of electron-electron interactions and collective excitations, plasmons, were studied [15, 16]. Graphite monolayers were observed already in 1962 by Boehm and collaborators [17]. Boehm obtained thin graphite fragments of reduced graphite oxide identifying some of them as graphene (the name graphene for monolayer was introduced later, in 1986 [18]). Ultrathin graphitic films were also obtained by growth techniques [19–22]. Analysis of their electronic properties was done by surface science techniques avoiding measurements related to quality or continuity of samples. Carrier dynamics in few-nm-thick graphite films was studied in the 90's [23, 24]. Ohashi reported resistivity changes by up to 8% with varying electric field for 20 nm thick samples. Using bottom-up techniques, a group lead by Mullen created "giant hydrocarbons" [25, 26].

In 1999, Ruoff developed a method called "mechanical exfoliation" [27]. They used a tip of Atomic Force Microscope (ATM) to manipulate small pillars patterned in the highly oriented pyrolytic graphite (HOPG) by plasma etching, Fig. 1.1. HOPG is characterized by high atomic purity and smooth surface. Carbon layers could be delaminated due to the weak van der Waals forces between consecutive layers. This method was realized by Geim's group using scotch tape to exfoliate few carbon layers from graphite in 2004 showing ambipolar electric field effect in thin graphene flakes [28], Fig. 1.2. The method of identifying few layer graphene samples required a combination of optical mi-

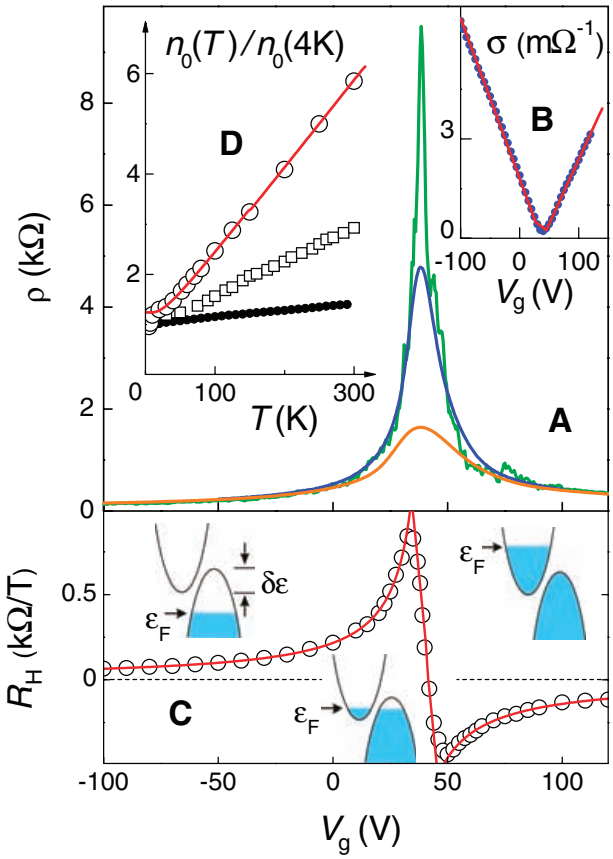

Figure 1.2: Electric field effect in thin graphene flakes. (A) Typical dependences of FLG's resistivity ρ on gate voltage for different temperatures (T=5, 70, and 300 K for top to bottom curves, respectively). (B) Example of changes in the film's conductivity $\sigma = 1/\rho(V_g)$ obtained by inverting the 70 K curve (dots). (C) Hall coefficient R_H versus Vg for the same film; T=5 K. (D) Temperature dependence of carrier concentration n_0 in the mixed state for the film in (A) (open circles), a thicker FLG film (squares), and multilayer graphene ($d \simeq 5$ nm; solid circles). Red curves in (B) to (D) are the dependences calculated from our model of a 2D semimetal illustrated by 0 insets in (C). Reprinted from Ref. [28].

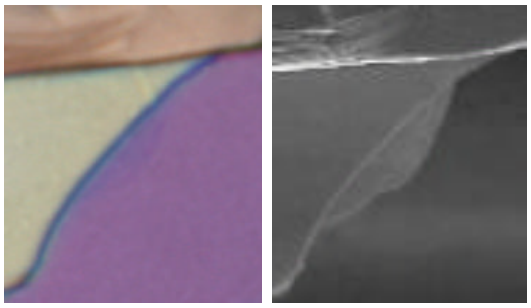

Figure 1.3: Images of a thin graphitic flake in optical (Left) and scanning electron (Right) microscopes. Few-layer graphene is clearly visible in SEM (in the center) but not in optics. Reprinted from supporting materials to Ref. [28].

croscope (OM), scanning electron microscope (SEM) and AFM. Thin graphite fragments, thinner than 50 nm, were completely invisible in OM but clearly seen in high-resolution SEM on SiO_2 substrate, Fig. 1.3. The added optical path shifts the resulting interference colors from violet-blue for pure SiO_2 substrate to blue for samples with graphitic films. These color shifts are sensitive to the number of graphene layers. A contrast is affected by the thickness of the SiO_2 substrate and the best is obtained for 300 nm thick substrate. A thickness of the substrate was crucial because 5 % change can make graphene completely invisible. After a first selection of thinnest fragments, AFM was used to identify fragments with thickness less than $\sim$ 1.5 nm because they were invisible even via the interference shift, Fig. 1.4. While AFM could identify number of graphene sheets in a sample (1, 2 or 3 layers), AFM tip destroyed it, e.g., by scratching their surface. Thus, it was not possible to identify the number of layers in the studied devices. Later, a group lead by Geim has shown a simple method of distinguishing single layer graphene, even with respect to bilayer, by using Raman spectroscopy [29]. Their samples were characterized by high quality. The carrier mobility exceeded 10000 cm2/Vs, which was crucial for the reported ballistic transport over submicron distances. It was shown that in thin graphene flakes a resistivity can be changed by a factor of $\sim$100 using a perpendicular electric field. It was also proven that independently of carrier concentration graphene conductivity is always larger than a minimum value corresponding to the quantum unit of the conductance [28, 30]. The most surprising in their experiment [28] was not the observation and the isolation of graphene but its electronic properties [31]. Atomic planes remained continuous

Figure 1.4: Single-layer graphene visualized by AFM. Narrow ($\simeq$100 nm) graphene stripe next to a thicker area. Colors: dark brown corresponds to SiO_2 surface, bright orange $\sim$ 2nm, light brown $\sim$ 0.5nm - the high of a single layer. Reprinted from supporting materials to Ref. [28].

and conductive under ambient conditions.

In next works, experiments on a single layer graphene were performed [30, 32]. Based on magneto-transport measurements, a single layer was shown to indeed exhibit a linear energy dispersion. Integer quantum Hall effect (IQHE) in graphene is distinctively different to that in conventional semiconductors with a parabolic dispersion. In graphene, Hall plateaus appear at half-integer filling factors with Landau level dispersion proportional to a square root of a magnetic field, Fig. 1.5. Additionally, a unit of the quantized conductance is four times larger than in conventional semiconductors. This is related to four fold degeneracy in graphene (spin degeneracy and valley degeneracy). In 2007, IQHE in graphene was demonstrated at room temperature [33, 34]. This was possible due to a high quality of samples and large cyclotron energies of "relativistic" electrons, and consequently a large separation between neighboring lowest Landau levels, Fig. 1.6.

The relativistic nature of carriers in graphene is also interesting from scientific point of view. Electrons move like they have zero rest mass with a velocity 300 times smaller than a speed of light [35]. Thus, one can probe quantum electrodynamics (QED) without need of expensive accelerators. One of effects characteristic for relativistic particles is Klein tunneling [36, 37]. A relativistic particle can travel through a high potential barrier, in some cases with 100%

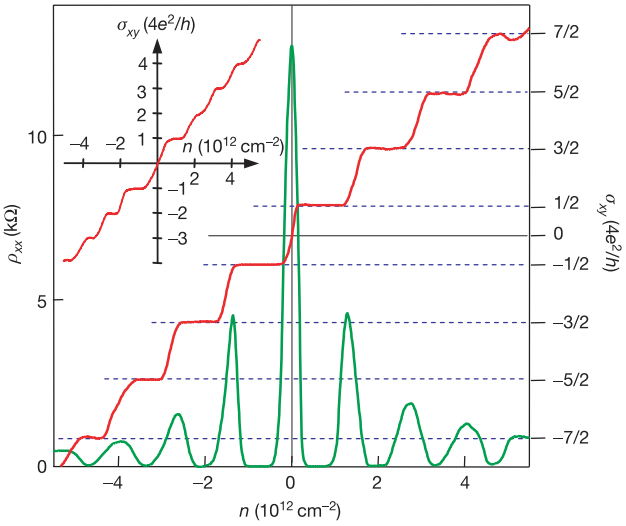

Figure 1.5: Hall conductivity σ_{xy} and longitudinal resistivity ρ_{xx} of graphene as a function of their concentration at $B = 14$ T and $T = 4$ K. $\sigma_{xy} = (4e^2/h)\nu$ is calculated from the measured dependences of $\rho_{xy}(\mathrm{V}_g)$ and $\rho_{xy}(\mathrm{V}_g)$ as $\sigma_{xy} = \rho_{xy}/(\rho_{xy}^2 + \rho_{xx}^2)$. The behaviour of $1/\rho_{xy}$ is similar but exhibits a discontinuity at $V_g \simeq 0$, which is avoided by plotting σ_{xy}. Inset: σ_{xy} in 'two-layer graphene' where the quantization sequence is normal and occurs at integer ν. The latter shows that the half-integer QHE is exclusive to 'ideal' graphene. Reprinted from Ref. [30].

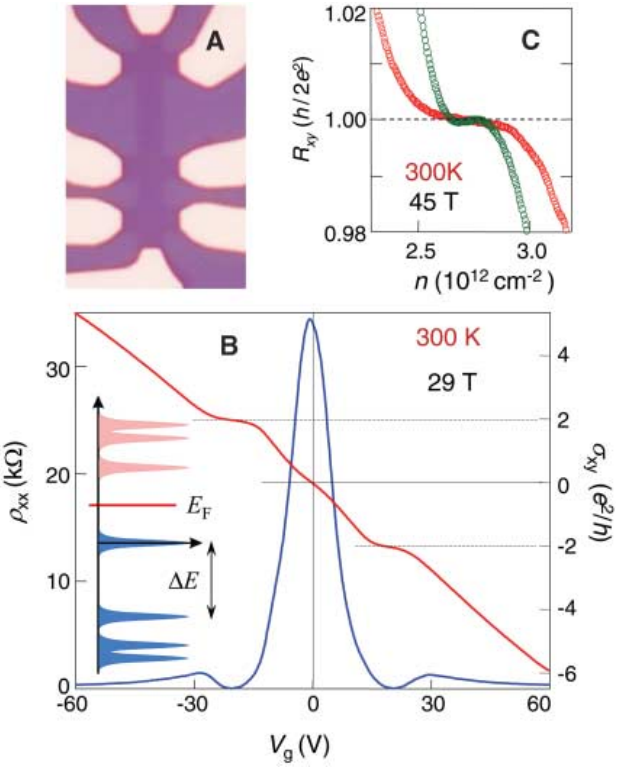

Figure 1.6: Room-temperature QHE in graphene. (A) Optical micrograph of one of the devices used in the measurements. The scale is given by the Hall bar's width of 2 μm. (B) σ_{xy} (red) and ρ_{xx} (blue) as a function of gate voltages (V_g) in a magnetic field of 29 T. Positive values of V_g induce electrons, and negative values of V_g induce holes, in concentrations $n = (7.2{\cdot}10^{10}\ \mathrm{cm}^{-2}\mathrm{V}^{-1})V_g$ (5, 6). (Inset) The LL quantization for Dirac fermions. (C) Hall resistance, R_{xy}, for electrons (red) and holes (green) shows the accuracy of the observed quantization at 45 T. Reprinted from Ref. [33].

probability. It is related to the fact that a barrier for electrons is also a well for holes, resulting in hole bound states inside it. Matching between electron and hole wavefunctions increases a probability of tunneling through the barrier [36]. It has an important consequence. Carriers can not be confined by an electric field which is crucial for applications in electronic devices. Klein tunneling in graphene was confirmed experimentally in 2009 [38, 39].

The possibility of controlling a resistivity in a wide range, high mobility, good quality of crystal and planar structure make graphene a material for electronic applications [40–44]. Recent works on suspended graphene have shown a mobility as large as 200000 cm^2/Vs which is more than 100 times larger than that of modern silicon transistors [45–48]. This mobility remains high even in high electric fields. The mean-free path in a suspended sample after annealing achieves 1 μm, which is comparable with a sample size. Additional, suspended graphene absorbs only 2.3 % of incident white light making it a material for transparent electrodes for touch screens and light panels [49]. Thus, graphene can be a competitor to the industrial transparent electrode material, indium tin oxide (ITO) [50].

Some potential applications in quantum information processing were also proposed. Graphene is built of carbon. ^{12}C has zero nuclear spin and graphene has weak spin-orbit coupling, hence it is expected that electron spin will have a very long coherence time. Thus, it is an ideal material for spin qubits [51–53]. From more immediate applications, graphene can be used as gas sensors. It is related to a maximum ratio of the surface area to a volume. In typical 3D materials, resistivity is not influenced by adsorption of a single molecules on their surface. This is not true in graphene. Adsorption of molecules from surrounding atmosphere causes doping of graphene by electrons or holes depending on the nature of the gas. This can be detected in resistivity measurements [54].

1.1.2 Fabrication methods

A method used by the Manchester group to obtain graphene is called a mechanical exfoliation. It is based on the fact that graphite consists of parallel graphene sheets, weakly bound by van der Waals forces. These forces can be overcome with an adhesive tape. Novoselov and Geim successively removed layers from a graphite flake by repeated peeling a dozen times [28]. Next, graphite fragments were pressed down against a substrate leaving thin films containing also a single layer. Due to an interference effect related to a special thickness of SiO_2 substrate (300 nm), it was possible to distinguish few and a

single layer in a sample, indicated by darker and lighter shades of purple. A mechanical exfoliation allows isolation of high-quality graphene samples with sizes in the 10 μm range, which excludes it from a method used in an industry. The efficient method of obtaining large graphene fragments with high-quality is a challenge. Beyond significant progress in achieving graphene by different methods, mechanical exfoliation remains the best in terms of electrical and structural quality of the obtained graphene. It is related to high-quality of starting single crystalline graphite source, HOPG. Below, we describe only small part of presently developed methods which are most promising for a mass production.

Chemical Vapor Decomposition

The alternative way of obtaining graphene is epitaxial growth of graphitic layers on top of other crystals. It provides high-quality multilayer graphene samples strongly interacting with their substrate. In 2009, a method of growing few layer graphene films by using chemical vapour deposition (CVD) on thin nickel layers was demonstrated [41, 55]. It was shown that the number of graphene layers can be controlled by changing the nickel thickness or growth time during a process. Transport measurements in high magnetic fields showed the half-integer quantum Hall effect, characteristic for monolayer graphene [41]. Their samples revealed good optical, electrical and mechanical properties. A sample size exceeds 1×1 cm^2 with graphene domain's size between 1 to 20 μm. A size of graphene films is limited only by CVD chamber size. It was possible to transfer samples to an arbitrary substrate, e.g by using dry-transfer process. The main problem in this method is related to a wide range of graphene layer thickness. However, it is very promising due to its high compatibility with current CMOS technology. CVD growth process was also used to grow graphene on cooper foils [56]. Obtained films contained only small percent ($<5\%$) of the area having more than a single layer. Samples revealed reasonable quality but a method still requires an improved of growth technique. Li and coworkers have shown an effect of different parameters on growth process [57]. They developed two-step CVD process to obtain large graphene domains with high mobility. Material quality was significantly improved but an effect of structural defects is still to be understood.

Thermal decomposition of SiC

A sublimation process of Si from SiC compound in high temperatures provides a graphitization of carbon atoms on the surface. The samples are heated in ultra high vacuum. By using this technique, Berger and de Heer produced few layers graphene [58, 59]. Their samples were continues over several mm revealing 2D electron gas properties and high mobility. An advantage of this method is a possibility of pattern films into narrow ribbons or other shapes by using conventional lithographic technique [60–62]. Additionaly, insulating SiC substrates can be used so a transfer to other insulator is not required. On the other hand, films were inhomogeneous in thickness with graphene monolayer grains typically 30-200 nm in diameter. An inhomogeneity influences on electronic properties, which depend on the number of layers. Emtsev *et al.* have improved this technique by using argon gas under high pressure [63]. A graphitization in an argon atmosphere enabled to increase a temperature process producing much larger monolayer graphene domains and reducing a number of defects. They obtained arrays of parallel terraces up to 3 μm wide and more than 50 μm long. They measured carrier mobility and reported values only five times smaller than that for exfoliated graphene on substrates in the limit of high doping. Graphene was also epitaxially growth by CVD on SiC [64–66]. The advantage of this method is that CVD growth is less sensitive to SiC surface defects. The high quality of graphene was confirmed by several techniques [66]. Single-atomic-layer could be identified by high spatial resolution ellipsometer. The annealing time and argon pressure are responsible for the growth kinetics of graphene influence on the number graphene layers. Material's properties were studied by STM and TEM [64]. The first carbon layer was about 2Å from the SiC surface as a result of a strong covalent bonds between carbon layer and silicon atoms on the SiC surface. Creation of edge dislocations in the graphene layers as a result of a bending of graphene planes on atomic steps was observed [64]. The conductivity of graphene thin films on SiC substrates was also measured [65]. It depended on the film's thickness and resided in $5 - 6.4 \cdot 10^6$ S/m.

Reduction of graphite oxide (GO)

In this method, graphite is chemically modified to produce graphite oxide (GO), by using the Hummer's method [67]. GO is dispersed in some solvent, e.g., water and can be chemically exfoliated. Graphene sheets are obtained by a chemical, thermal or electrochemical reduction process of oxy-

gen groups [68–71]. The level of oxidization determines electrical conductivity and optical transparency [72]. During this process, a quality of samples is significantly reduced due to a change from sp^2 to sp^3 hybridization for many carbon atoms. It decreases a mobility of samples. On the other hand, films reveal high flexibility and stiffness much better than that of other paper-like materials [69]. The production technique is low cost and can be scaled up to produce larger pieces of graphene.

1.1.3 Mechanical properties

Graphene is a two-dimensional crystal characterized by a high quality. It is continuous on a macroscopic scale [73]. Surprisingly, it is stable under ambient conditions. According to Peierls, Landau, and Mermin works, long range order in 2D should be destroyed by thermal fluctuations [74–77]. Their analysis regarded truly 2D material without defects, but not a 2D system which is a part of larger 3D structure. In this case, a stability of crystal can be supported by a substrate or present disorder. On the other hand, in 2007 graphene suspended above a substrate was demonstrated [45]. These graphene membranes were stable under ambient conditions. It was shown by transmission electron microscopy (TEM) that graphene has high quality lattice with occasional point defects [78]. Stability was enabled through elastic deformations in a third dimension related to interactions between bending and stretching long-wavelength phonons. Above conclusions were explained by a nanobeam electron diffraction patterns which changed with a tilt angle. Diffraction peaks were sharp for normal incidence but broadened for different angles revealing that graphene is not perfectly flat. Samples were estimated to exhibit ripples with $\sim$1 nm hight and few nanometers length. It is expected that they strongly influence electronic properties and can be created in a controllable way by thermally generated strains [79].

Experiments on graphene membranes enable to estimate rigidity, elasticity and thermal conductivity. Lee *et al.* and Bunch *et al.* performed experiments and numerical simulations on graphene strength and elasticity [80, 81]. They determined an intrinsic strength which is a maximum strength that can be supported by the defect-free material. Obtained values correspond to largest Young modulus ever measured, $\sim$1 TPa. Such high value is responsible for graphene robustness and stiffness. It answers the question why large graphene membranes, with up to 100 μm, do not scroll or fold [82]. Additionally, results regarding elastic properties predict high tolerance on deformations well beyond

a linear regime [80]. Graphene also reveals high thermal conductivity, predicted by Mingo *et al.* [83] and measured by Balandin *et al.* [84]. The experiment required unconventional technique for non-contact measurement, the confocal micro-Raman spectroscopy. They heated a sample by different power laser with 488 nm laser light and observed a shift of Raman G peak with an excitation power. Experimental data were fitted to the equation for thermal conductivity of acoustic phonons because of a negligible electron contribution. A value in room temperature exceeds 5300 W/mK, which is larger than that for carbon nanotubes, 3000 W/mK.

1.2 Electronic band structure

1.2.1 Tight-Binding model

Graphene is a two-dimensional crystal built of carbon atoms. Each carbon atom has four valence electrons. Bonds between adjacent atoms are formed from three valence electrons on s, p_x and p_y atomic orbitals. These hybrid orbitals are responsible for a structural stability of a graphene layer. The fourth valence electron is on the p_z orbital that is orthogonal to the graphene plane. It is weakly bound and determines electronic properties of the system. Single particle properties of graphene can be described by using the one orbital tight-binding (TB) Hamiltonian [1].

A graphene lattice is a lattice with a basis, forming so called honeycomb lattice, shown in Fig. 1.7. There are two atoms in a unit cell which form two sublattices. Each sublattice is a triangular Bravais lattice, labeled as A and B and distinguished by red and blue colors in Fig. 1.7. The distance between nearest neighboring atoms in the structure is $a = 1.42$ Å. Primitive unit vectors can be defined as $\mathbf{a}_{1,2} = a/2(\pm\sqrt{3}, 3)$. By using vectors $\mathbf{R} = n\mathbf{a}_1 + m\mathbf{a}_2$, with n, m integers, positions of all atoms in the structure can be obtained. Hamiltonian for a graphene lattice has a following form

$$H = \frac{p^2}{2m} + \sum_{\mathbf{R}} \left(V^A(\mathbf{r} - \mathbf{R}) + V^B(\mathbf{r} - \mathbf{R} - \mathbf{b}) \right), \tag{1.1}$$

where $V^A(\mathbf{r} - \mathbf{R})$ is atomic potential on site $\mathbf{R}$ of A-type atom and $\mathbf{b} = a(0, 1)$ is a vector between two nearest neighboring atoms from the same unit cell. Due to a translation symmetry of the system, and according to Bloch's theorem, a

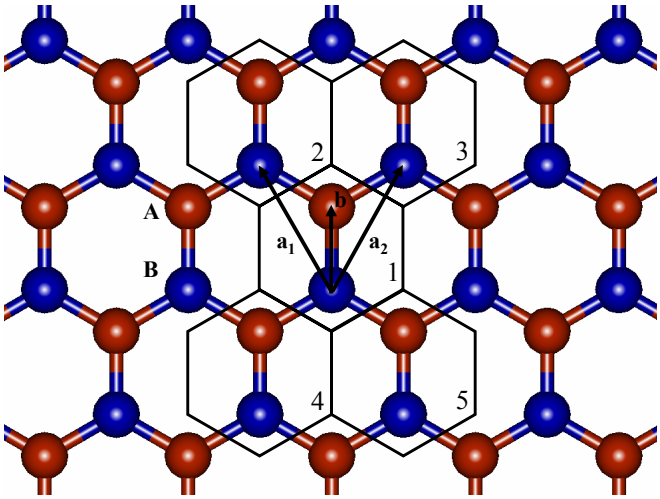

Figure 1.7: (Color online) Graphene honeycomb lattice. There are two atoms in a unit cell, A and B, distinguished by red and blue colors. Primitive unit vectors are defined as $\mathbf{a}_{1,2} = a/2(\pm\sqrt{3}, 3)$. $\mathbf{b} = a(0, 1)$ is a vector between two nearest neighboring atoms from the same unit cell.

wave function for an electron on a graphene lattice can be written as

$$\begin{aligned} \Psi_{\mathbf{k}}(\mathbf{r}) &= \frac{1}{\sqrt{N_c}} \sum_{\mathbf{R}} e^{i\mathbf{k}\mathbf{R}} (A\phi_z^A(\mathbf{r}-\mathbf{R}) + B\phi_z^B(\mathbf{r}-\mathbf{R}-\mathbf{b})) \\ &= A\Psi_{\mathbf{k}}^A(\mathbf{r}) + B\Psi_{\mathbf{k}}^B(\mathbf{r}), \end{aligned} \tag{1.2}$$

where $\phi_z^A(\mathbf{r}-\mathbf{R})$ are p_z orbitals centered at a lattice site $\mathbf{R}$, A and B are expansion coefficients, and N_c is the number of unit cells. Orbitals corresponding to the nearest neighboring atoms are not orthogonal, $\langle \phi_z^A(\mathbf{r}-\mathbf{R}') | \phi_z^B(\mathbf{r}-\mathbf{R}-\mathbf{b}) \rangle \neq 0$, for $|\mathbf{R}' - \mathbf{R} - \mathbf{b}| = a$. For nonorthogonal basis, a generalized eigenvalue problem has to be solved, with a matrix of overlap integrals S. The basis functions can also be orthogonalized and a matrix of overlap integrals becomes a unit matrix. The Schrödinger equation for Hamiltonian given by Eq. 1.1 is written as

$$H\Psi_{\mathbf{k}}(\mathbf{r}) = E(\mathbf{k})\Psi_{\mathbf{k}}(\mathbf{r}). \tag{1.3}$$

We project onto $\Psi_{\mathbf{k}}^A(\mathbf{r})$ and $\Psi_{\mathbf{k}}^B(\mathbf{r})$. When we neglect three center integrals and leave only terms corresponding to neighboring atoms, the Schrodinger equation can be written as

$$\begin{pmatrix} \epsilon - E(\mathbf{k}) & tf(\mathbf{k}) \\ tf^*(\mathbf{k}) & \epsilon - E(\mathbf{k}) \end{pmatrix} \begin{pmatrix} A \\ B \end{pmatrix} = 0, \tag{1.4}$$

where ϵ is an energy related to the presence of atomic potentials of all carbon

atoms in the system and we define a hopping integral

$$t = \langle \phi_z^A (\mathbf{r} - \mathbf{R}) \,|\, \left[V^A (\mathbf{r} - \mathbf{R}) \right] |\phi_z^B (\mathbf{r} - \mathbf{R}' - \mathbf{b}) \rangle \tag{1.5}$$

for $|\mathbf{R} - \mathbf{R}' - \mathbf{b}| = a$, and

$$f(\mathbf{k}) = \sum_{\mathbf{R}'} e^{i\mathbf{k}(\mathbf{R}'-\mathbf{R})}, \tag{1.6}$$

where a summation is over nearest neighbors of an atom on site $\mathbf{R}$. A method of finding the function $f(\mathbf{k})$ is following. In Fig. 1.7 few unit cells are plotted. We label a central unit cell in a position given by a vector $\mathbf{R}$ by 1. An A-type atom from this cell, indicated by a red color, has three nearest neighboring B-type atoms, indicated by blue colors. First one is in the same unit cell, so we get exponential factor $e^{i\mathbf{k}(\mathbf{R}-\mathbf{R})} = 1$. A second one is in a unit cell labeled as 2. This unit cell can be achieved by moving a unit cell in $\mathbf{R}$ by a primitive vector $\mathbf{a_1}$, $\mathbf{R}' = \mathbf{R} + \mathbf{a_1}$. It corresponds to an exponent $e^{i\mathbf{k}(\mathbf{R}'-\mathbf{R})} = e^{i\mathbf{k}\mathbf{a_1}}$. Similarly, third nearest neighbor is in a unit cell labeled as 3, giving an exponent $e^{i\mathbf{k}(\mathbf{R}'-\mathbf{R})} = e^{i\mathbf{k}\mathbf{a_2}}$. Finally, we can write Eq. 1.6 as

$$f(\mathbf{k}) = 1 + e^{i\mathbf{k}\mathbf{a_1}} + e^{i\mathbf{k}\mathbf{a_2}}. \tag{1.7}$$

In Schrodinger equation given by Eq. 1.4, we neglect constant diagonal term ϵ, which just shift entire spectrum by a constant value. The solution can be written as

$$E(k) = \pm |t||f(\mathbf{k})|, \tag{1.8}$$

with a hopping integral $t = -2.5$ eV. $|f(\mathbf{k})|$ can be calculated using Eq. (1.7) which gives

$$|f(\mathbf{k})| = \sqrt{3 + 2\cos \mathbf{k}\mathbf{a_1} + 2\cos \mathbf{k}\mathbf{a_2} + 2\cos \mathbf{k}(\mathbf{a_2} - \mathbf{a_1})}. \tag{1.9}$$

Substituting a solution given by Eq. (1.8) into Eq. (1.4) we can obtain relations between coefficients A and B. For "+"energies, an electron branch (a conduction band), we get $\frac{f(\mathbf{k})}{|f(\mathbf{k})|} B = A$ and substituting it into Eg. (1.2) an eigenfunction can be written as

$$\Psi_{\mathbf{k}}^c (\mathbf{r}) \;=\; \frac{1}{\sqrt{2N_c}} \sum_{\mathbf{R}} e^{i\mathbf{k}\mathbf{R}} (\phi_z^A (\mathbf{r} - \mathbf{R}) - e^{-i\theta_{\mathbf{k}}} \phi_z^B (\mathbf{r} - \mathbf{R} - \mathbf{b})), \tag{1.10}$$

where we define $\exp i\theta_{\mathbf{k}} = \frac{f(\mathbf{k})}{|f(\mathbf{k})|}$ and we got an extra normalization factor $\frac{1}{\sqrt{2}}$ from a condition $|A|^2 + |B|^2 = 1$. A minus sign comes from a definition of a hopping integral, $t = -2.5$ eV. We note that one can positively define a hopping

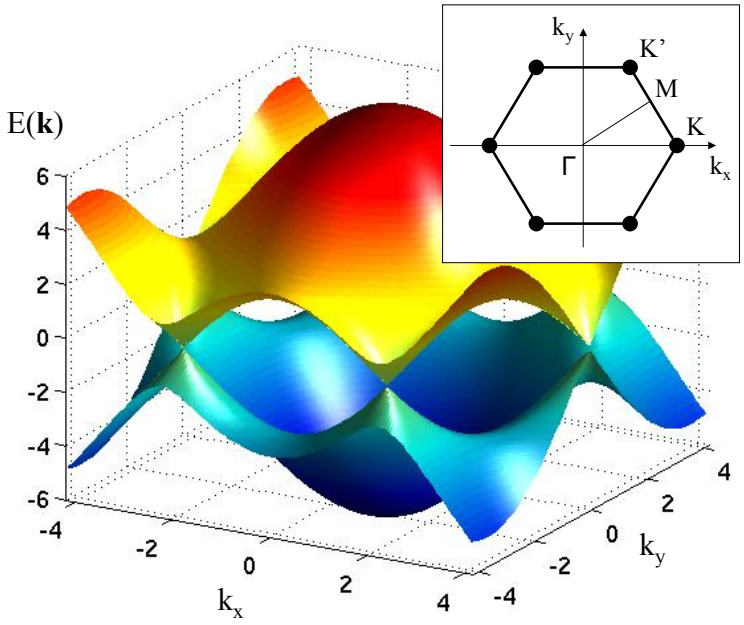

Figure 1.8: The band structure of graphene. The Fermi level is at $E(k) = 0$, where the valence and the conduction band touch each other in six points. These are corners of the first Brillouin zone, seen in a projection of the Brillouin zone shown in the right upper corner inset. From these six points only two are nonequivalent, indicated by K and K'. Other high symmetry points of reciprocal space are also indicated.

integral t and then minus signs appear in off diagonal matrix elements of Eq. (1.4), getting the same result. For "$-$" energies, a hole branch (a valence band), we get

$$\Psi^v_{\mathbf{k}}(\mathbf{r}) = \frac{1}{\sqrt{2N_c}} \sum_{\mathbf{R}} e^{i\mathbf{kR}} (\phi^A_z(\mathbf{r}-\mathbf{R}) + e^{-i\theta_{\mathbf{k}}} \phi^B_z(\mathbf{r}-\mathbf{R}-\mathbf{b})). \quad (1.11)$$

We can emphasize two points of above eigenfunctions: (i) There is a phase relation between two sublattices in a honeycomb lattice, $\theta_{\mathbf{k}}$. (ii) When going from the valence band into the conduction band, a wave function accumulate an extra phase π, $e^{i\pi} = -1$.

The energy spectrum $E(k)$ of graphene given by Eq. (1.8) is shown in Fig. 1.8. For the charge neutral system, each carbon atom gives one electron on p_z orbital. As a result, the Fermi level is at $E(k) = 0$. Signs $\pm$ in Eq. (1.8) correspond to the electron and hole branches, respectively. We note here that electron-hole symmetry is conserved but only for a solution in a nearest neighbor's approximation. From Fig. 1.8, it is seen that a valence and conduction band touch each other in six points. These are corners of the

first Brillouin zone, seen in a projection of the Brillouin zone shown in the right upper corner inset. From these six points only two are nonequivalent, indicated by K and K'. The rest four corners can be obtain by a translation by a reciprocal vectors. In the inset, also other high symmetry points of reciprocal space are indicated, a Γ point in a center of a Brillouin zone and an M point. We can look at a solution of Eq. (1.4) at a Γ point, which corresponds to $\mathbf{k} = 0$. For electron branch, one gets $E(\mathbf{k} = \mathbf{0}) = +3|t|$ and for hole branch $E(\mathbf{k} = 0) = -3|t|$. Thus, Γ point corresponds to energy levels far away from the Fermi energy, $E(\mathbf{k}) = 0$, which can be also seen in Fig. 1.8. Corresponding wave functions for a Γ point are

$$\Psi_{\Gamma}^{c} = \frac{1}{\sqrt{2}} \begin{pmatrix} 1 \\ -1 \end{pmatrix} \tag{1.12}$$

for an electron branch (a conduction band) and

$$\Psi_{\Gamma}^{v} = \frac{1}{\sqrt{2}} \begin{pmatrix} 1 \\ 1 \end{pmatrix} \tag{1.13}$$

for a hole branch (a valence band). These results are in agreement with an intuition, giving an anti-symmetric (anti-bonding) wave function for a conduction band and a symmetric (bonding) wave function for a valence band. In next subsection, we focus on low energy electronic properties which correspond to states around K and K' points.

1.2.2 Effective mass approximation

Graphene band structure given by Eq. (1.8) can be expanded around $\mathbf{K}$ and $\mathbf{K}'$ points in a Taylor series. The function given by Eq. (1.7) can be written as

$$f(\mathbf{K} + \mathbf{q}) = 1 + e^{i(\mathbf{K}\mathbf{a_1} + \mathbf{q}\mathbf{a_1})} + e^{i(\mathbf{K}\mathbf{a_2} + \mathbf{q}\mathbf{a_1})}, \tag{1.14}$$

where $\mathbf{q}$ is some small vector. We restrict to linear terms in $\mathbf{q}$ in a Taylor expansion and write Eq. (1.14) as

$$\begin{aligned} f(\mathbf{K} + \mathbf{q}) &= 1 + e^{i\mathbf{K}\mathbf{a_1}}(1 + i\mathbf{q}\mathbf{a_1}) + e^{i\mathbf{K}\mathbf{a_2}}(1 + i\mathbf{q}\mathbf{a_2}) \\ &= 1 + e^{i\mathbf{K}\mathbf{a_1}} + e^{i\mathbf{K}\mathbf{a_1}} i\mathbf{q}\mathbf{a_1} + e^{i\mathbf{K}\mathbf{a_2}} + e^{i\mathbf{K}\mathbf{a_2}} i\mathbf{q}\mathbf{a_2} \\ &= f(\mathbf{K}) + e^{i\mathbf{K}\mathbf{a_1}} i\mathbf{q}\mathbf{a_1} + e^{i\mathbf{K}\mathbf{a_2}} i\mathbf{q}\mathbf{a_2} \\ &= e^{i\mathbf{K}\mathbf{a_1}} i\mathbf{q}\mathbf{a_1} + e^{i\mathbf{K}\mathbf{a_2}} i\mathbf{q}\mathbf{a_2}, \end{aligned} \tag{1.15}$$

where we have used a fact that $f(\mathbf{K}) = 1 + e^{i\mathbf{K}\mathbf{a_1}} + e^{i\mathbf{K}\mathbf{a_2}} = 0$. From six corner points, we choose one, $\mathbf{K} = \frac{2\pi}{a}(\frac{2}{3\sqrt{3}}, 0)$. By using a definition of vectors $\mathbf{a}_{1,2}$, $\mathbf{a}_{1,2} = a/2(\pm\sqrt{3}, 3)$ we get

$$\begin{aligned} \mathbf{K}\mathbf{a_1} &= \frac{4\pi}{3\sqrt{3}a} \cdot (a\sqrt{3}/2) = \frac{2\pi}{3} \\ \mathbf{K}\mathbf{a_2} &= \frac{4\pi}{3\sqrt{3}a} \cdot (-a\sqrt{3}/2) = -\frac{2\pi}{3}. \end{aligned} \tag{1.16}$$

One can easily check that

$$1 + e^{i\frac{2\pi}{3}} + e^{-i\frac{2\pi}{3}} = 0.$$

Substituting Eq. (1.16) into Eq. (1.15) one gets

$$\begin{aligned} f(\mathbf{K}+\mathbf{q}) &= e^{i\frac{2\pi}{3}} i\mathbf{q}\mathbf{a_1} + e^{-i\frac{2\pi}{3}} i\mathbf{q}\mathbf{a_2} \\ &= i\left(-\frac{1}{2} + i\frac{\sqrt{3}}{2}\right) a\left(q_x\frac{\sqrt{3}}{2} + \frac{3}{2}q_y\right) \\ &+ i\left(-\frac{1}{2} - i\frac{\sqrt{3}}{2}\right) a\left(-q_x\frac{\sqrt{3}}{2} + \frac{3}{2}q_y\right) \\ &= \frac{3}{2}a\left(-q_x - iq_y\right). \end{aligned}$$

Eq. (1.4) around point $\mathbf{K} = \frac{2\pi}{a}(\frac{2}{3\sqrt{3}}, 0)$ for small $\mathbf{q}$, can be written as

$$\begin{pmatrix} 0 & -\frac{3}{2}ta\left(q_x + iq_y\right) \\ -\frac{3}{2}ta\left(q_x - iq_y\right) & 0 \end{pmatrix} \begin{pmatrix} A \\ B \end{pmatrix} = E_{\mathbf{K}}\left(\mathbf{q}\right) \begin{pmatrix} A \\ B \end{pmatrix}, \tag{1.17}$$

where we took into account fact that $f^*(\mathbf{K}+\mathbf{q}) = -\frac{3}{2}ta\left(q_x - iq_y\right)$. Eq. (1.17) has a solution for energy eigenvalues

$$E_{\mathbf{K}}\left(\mathbf{q}\right) = \pm\frac{3}{2}a|t||\mathbf{q}| \tag{1.18}$$

and corresponding wave functions

$$\Psi_{\mathbf{K}}\left(\mathbf{q}\right) = \frac{1}{\sqrt{2}} \begin{pmatrix} 1 \\ \pm e^{-i\theta_{\mathbf{q}}} \end{pmatrix} \tag{1.19}$$

with $\theta_{\mathbf{q}} = \arctan\frac{q_x}{q_y}$ an angle in a reciprocal space and $\pm$ signs for a conduction and valence band, respectively. Similar calculations can be done around point $\mathbf{K}' = \frac{2\pi}{a}(-\frac{2}{3\sqrt{3}}, 0)$. For small $\mathbf{q}$ one gets Eq. (1.4) for $\mathbf{K}'$ as

$$\begin{pmatrix} 0 & \frac{3}{2}ta\left(q_x - iq_y\right) \\ \frac{3}{2}ta\left(q_x + iq_y\right) & 0 \end{pmatrix} \begin{pmatrix} A \\ B \end{pmatrix} = E_{\mathbf{K}'}\left(\mathbf{q}\right) \begin{pmatrix} A \\ B \end{pmatrix}. \tag{1.20}$$

Eq. 1.20 has a solution for energy eigenvalues

$$E_{\mathbf{K}'}(\mathbf{q}) = \pm\frac{3}{2}a|t||\mathbf{q}| \tag{1.21}$$

and corresponding wave functions

$$\Psi_{\mathbf{K}'}(\mathbf{q}) = \frac{1}{\sqrt{2}}\begin{pmatrix} 1 \\ \mp e^{i\theta_{\mathbf{q}}} \end{pmatrix} \tag{1.22}$$

By introducing a Fermi velocity $v_F = \frac{3ta}{2\hbar}$, we can write Eq. (1.18) and Eq. (1.21) as

$$E(\mathbf{q}) = \pm\hbar v_F|\mathbf{q}|. \tag{1.23}$$

This solution is identical to the solution of the Dirac Hamiltonian for relativistic massless fermions. Here, a speed of light is played by a Fermi velocity. One can estimate $v_F \simeq 10^6\ m/s$ which is 300 times smaller than a speed of light. We look at the eigenfunctions given by Eq. (1.19) and Eq. (1.22). They consist of two components, in an analogy to spinor wave functions for fermions. Here, a role of spin is played by two sublattices, A and B. Rotations within a spinor's subspace can be described by Pauli matrices $\sigma = (\sigma_x, \sigma_y, \sigma_z)$. Thus, the eigenfunctions given by Eq. (1.19) and Eq. (1.22) are usually called pseudospinors.

1.3 Graphene nanostructures

Considerable interest in graphene is related to potential electronic applications, e.g., as transistors, transparent electrodes or photodetectors. In the case of, e.g., a transistor, a current need to be changed in a controllable way. Graphene is a semiconductor with a zero-energy band gap. Additionally, as a result of Klein paradox, it is difficult to confine particles by an electrostatic gate. The problem of controlling a transfer of carriers can be solved by using a spatial confinement. As a result of size quantization, an energy gap opens. Semi-metallic graphene becomes a semiconducting nanostructure. Thus, a new field associated with graphene nanostructures is developing. Among graphene nanostructures, strips of graphene (ribbons) and graphene islands (quantum dots) are of particular attention.

1.3.1 Fabrication methods

Graphene can be patterned into strips with different widths by use of e-beam lithography and an etching mask, as proposed by P. Kim's group [85,

86]. One can start from high quality graphene sample obtained by mechanical exfoliation. Next, graphene is deposited onto heavily p-doped Si substrates covered by SiO_2 layer. Strips of graphene can be covered by a protective etch mask from a cubical-shaped molecule having one Si atom at each corner, with corners being linked via oxygen atoms. This compound is called hydrogen silsesquioxane (HSQ). The unprotected graphene is etched away by an oxygen plasma. By using this technique, Kim's group were able to perform transport experiments on sample with a variety of widths, from 20–500 nm and lengths $\sim$ 1 μm. They noted that transport properties strongly depend on both boundary scattering and trapped charges in the substrate.

The other method of creating ribbons was proposed by Jia *et al.* They used Joule heating and electron beam irradiation [87]. Samples were exposure to electron irradiation for 20 min. and next heated by directional high electrical current. The theoretical background of the need of these two steps was pointed in Ref. [87–89]. During the heating, carbon atoms on sharp edges vaporize, so they were able to create structures with smooth edges.

Li *et al.* chemically derived graphene nanoribbons (GNRs) with well defined edges [90]. The width of ribbons varied from $\sim$ 10 to $\sim$ 50 nm with length $\sim$ 1 μm. Graphene nanostructures with irregular shapes were also reported. They observed ribbons with 120^o kink and zigzag edges. While above work regarded the thinnest ribbons with $\sim$10 nm width, Cai *et al.* proposed a method of creating ribbons with width less than $\sim$1 nm [91]. They started from colligated monomers, which define the width of the ribbon. These monomers were deposited onto the clean substrate surfaces by sublimation from a sixfold evaporator. They used two-step annealed process with different temperatures for straight and so called chevron-type ribbons. Many other chemical approaches to create graphene quantum nanostrucuters with different shapes are also proposed [92–96]. A relevant problem regards the dependence of the electronic properties on chirality of the graphene nanoribbon. It is related to the angle at which a ribbon is cut. GNRs, having different chiralities and widths, were chemically synthesized by unzipping a carbon nanotube [97, 98]. By using STM the presence of 1D GNR edge states was confirmed. Jaskólski *et al.* predicted general rules to the existence of edge states [99]. The comparison of experimental results with the theoretical prediction based on the Hubbard model and density functional theory (DFT) calculations provided an evidence for the formation of spin-polarized edge states [98, 100–102]. It was shown that electronic and magnetic properties can be tuned by changing the edge chirality and the width [103]. Partially unzipped carbon nanotubes were also

studied [104, 105]. Topological defects similar to that at the interface between two graphene layers were considered. An appearance of spatially localized interface states was predicted [104].

McEuen *et al.* studied graphite quantum dots, with thickness from few to tens of nanometers and lateral dimensions $\sim$1 μm [106]. They were placed onto a Si wafer with a 200 nm thermally grown oxide and connected to electrodes. Electrical transport measurements show Coulomb blockade phenomena. By analyzing a period of Coulomb oscillations in gate voltage, they demonstrated that the dot area extends into the graphite piece lying under the electrodes. Graphene quantum dots were experimentally fabricated starting from graphene sheet. Ponomarenko *et al.* produced structures with different sizes with oxygen plasma etching and a protection mask obtained by using high-resolution electron-beam lithography [107]. Their method allows to create quantum dots even with 10 nm radius but not with well defined shape. Ensslin *et al.* studied a tunable graphene quantum dots fabricated based on reactive ion etching (RIE) patterned graphene [108–112]. Close to the dot, $\sim$ 60 nm, wide graphene nanoribbon were placed. Using Coulomb diamond measurements, the charging energy was estimated. Coulomb resonances were demonstrated. They were also able to detect individual charging events [109]. They detect excited states via direct transport experiments. A rich variety of excited state spectrum in an external magnetic field was observed [113–116]. More regular structures were also created [117, 118]. Graphene QDs were supported on Ir(111) surface. Diameter of quantum dots varies from 2–40 nm and reveals soft edges, which was confirmed by a comparison with TB and DFT calculations.

Promising alternative to previously mentioned works is created graphene nanostructures by cutting graphene into desired shapes. It was shown that few layer [119] and single layer [120] graphene can be cut by using metallic particles. The process was based on anisotropic etching of thermally activated nickel particles. The cuts were directed along proper crystallographic orientation with the width of cuts determined by a diameter of metal particles. By using this technique, they were able to produce ribbons, equilateral triangles and other graphene nanostructures.

1.3.2 The role of edges

Two types of edges in a honeycomb lattice are of particular interest due to their stability: armchair and zigzag. They were experimentally observed near single-step edges at the surface of exfoliated graphite by Scanning tun-

neling microscopy (STM) and spectroscopy (STS) [121–125] and Raman spectroscopy [126–128]. Jia *et al.* have shown that zigzag and armchair edges are characterized by different activation energy [87]. According to their molecular dynamics calculations, 11 eV for zigzag and 6.7 eV for armchair, activation energies were estimated. This enabled them to eliminate an armchair edge with respect to zigzag one by applying higher bias voltages and consequently increasing electrical current flowing through the sample, which heated the sample.

The dynamics of edges was also studied [129, 130]. The measurements were performed in real time by side spherical aberration-corrected transmission electron microscopy with sensitivity required to detect every carbon atom, which remains stable for a sufficient amount of time. The most prominent edge structure was of the zigzag type. Koskinen, Malola and Häkinen predicted, by using DFT calculations, the stability of reconstructed ZZ_{57} edges [131]. The variety of stable combinations of pentagons, heptagons or higher polygons was observed [129, 132].

Theoretical calculations predicted edge states in the vicinity of the Fermi energy for structures with zigzag edges [100, 133–145]. These edge states were clearly identified experimentally [121–125]. They form a degenerate band in graphene ribbons [100, 133–135, 137]. It was also shown by using Hubbard model in a mean-field approximation that in graphene nanoribbons electrons on edge states reveal ferromagnetic order within an edge and anitferromagnetic order between opposite zigzag edges [134, 146, 147]. Son et al. have shown by using first-principles calculations that magnetic properties can be controlled by the external electric field applied across the ribbon [135]. The electric field lifts the spin degeneracy by reducing the band gap for one spin channel and widening of a gap for the other. In consequence, one can change antiferromagnetic coupling between opposite edges into ferromagnetic one. In the following years, graphene ribbons have been widely investigated [148–153].

The effect of edges was also studied in graphene quantum dots (GQD). It was shown that the type of edges influences the optical properties [136,154,155]. In GQDs with zigzag edges, edge states can collapse to a degenerate shell on the Fermi level [136, 138–141, 143–145]. The relation between the degeneracy of the shell to the difference between the number of atoms corresponding to two sublattices in the bipartite lattice was pointed [138, 139, 141, 145]. One of systems with the degenerate shell is triangular graphene quantum dot (TGQD). Hence, the electronic properties of TGQDs were extensively studied [95, 136, 138–141, 144, 145, 156–165]. For a half-filled degenerate shell,

TGQDs were studied by Ezawa using the Heisenberg Hamiltonian [138], by Fernandez-Rossier and Palacios [139] using mean-field Hubbard model, by Wang, Meng and Kaxiras [141] using DFT. It was shown that the ground state corresponds to fully spin polarized edges, with a finite magnetic moment proportional to the shell degeneracy. In Section 4.1, we describe our results regarding TGQDs obtained within exact diagonalization techniques [144, 165].

1.3.3 Size quantization effects

As a result of spatial confinement of carriers in graphene nanostructures, the discretization of the energy spectrum and an opening of the energy gap are expected. In graphene ribbons, the gap opening was predicted by using TB model or starting from Dirac Hamiltonian [133, 166, 167]. Ribbons with armchair edges oscillates between insulating and metallic as the width changes. An analytic scaling rules for the size of the band gaps were obtained as a function of width, primarily in inverse proportion [100]. The experimental observation of the opening of the energy gap for the narrowest ribbons was pointed, with a scaling behavior in agreement with theoretical predictions [85, 86, 90].

Ponomarenko *et al.* have shown that for GQDs with a diameter $D < 100$ nm, quantum confinement effects start playing a role [107]. They observed Coulomb peak oscillations as a function of gate voltage with randomly varied distances. These results were in agreement with a prediction for chaotic Dirac billiards, expected behavior for Dirac fermions in an arbitrary shape confinement [168]. An exponential decrease of the energy gap as a function of the diameter for Dirac fermions was predicted theoretically by Recher and Trauzettel [169].

In few nm GDQs with well-defined edges, high symmetry standing waves by using STM were observed [117, 118, 170]. These observations are in good agreement with TB and DFT calculations. Akola *et al.* have shown that a structure of shells and super-shells in the energy spectrum of circular quantum dots and TGQD is created [140, 142]. According to their calculations, TGQD with the edge length at least $\sim$ 40nm is needed to observe clearly the first super-shell oscillation. TB calculations predict an opening of the energy gap for arbitrary shape GQDs. An exponential decrease of the energy gap with the number of atoms is predicted [154, 155, 170]. This behavior is quantitatively different for structures with zigzag and armchair edges, which is related to the edge states present in systems with zigzag edges [155].

Chapter 2

Single particle properties of graphene quantum dots

2.1 Size, shape and edge dependence of single particle spectrum

2.1.1 Tight-Binding model

We start from writing TB Hamiltonian in a nearest neighbors approximation in a second quantization form. It can be written as

$$H_{TB} = t \sum_{<i,l>,\sigma} c^{\dagger}_{i\sigma} c_{l\sigma}, \tag{2.1}$$

where $c^{\dagger}_{i\sigma}$ and $c_{i\sigma}$ are creation and annihilation operators on a lattice site i and $< i, l >$ indicates a summation over nearest neighbor site. A hopping integral t is defined by Eq. (1.5) for A and B type neighbor atoms. This Hamiltonian can be used to describe finite size systems by applying appropriate boundary conditions on edges, e. g. putting a hopping integral to auxiliary atoms connected to edge atoms (these with only two neighbors) $t = 0$. We show a method of building a TB Hamiltonian matrix on an example of TGQD consisting of $N = 22$ atoms. We linked indices j, from $j = 0$ to $j = 21$, to all atomic p_z orbitals, shown in Fig. 2.1. A wavefunction of the system is built of a linear combination of these 22 orbitals, which determines a size of the TB Hamiltonian matrix. Nonzero matrix elements for Hamiltonian given by Eq. (2.1) corresponds to elements between p_z orbitals from neighboring sites. All of them equal to hopping integral t, which is a constant. Thus, t can be factored out from a matrix. Matrix elements are "1", when calculated between orbitals corresponding to neighboring sites or "0", in other case. Hamiltonian matrix

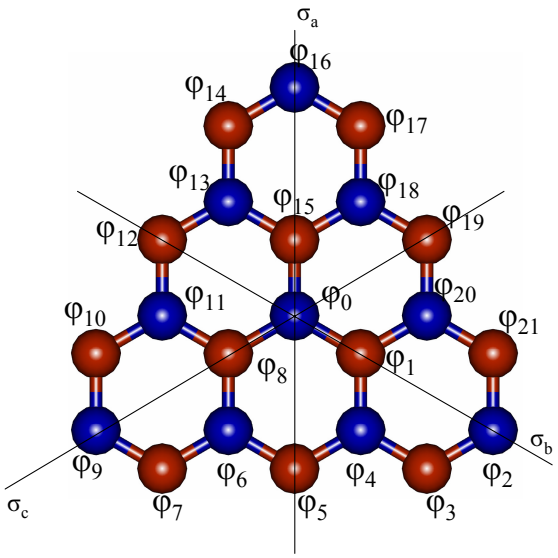

Figure 2.1: Linking up indices j to all atomic p_z orbitals for TGQD consisting of $N = 22$ atoms.

is diagonalized numerically, and eigenvalues and eigenvectors in an ascending order, with indices from "1" to "22", are obtained.

In Fig. 2.2, TB energy spectra in the vicinity of the Fermi level, $E = 0$, for graphene quantum dots with a similar number of atoms, $N \sim 100$, but different shapes and edges, are shown. All spectra are symmetric with respect to $E = 0$. We note that this symmetry is broken, when hopping integrals to next-nearest neighbors are included. Fig. 2.2(a) and (b) correspond to structures with armchair edges, hexagonal and triangular shapes, respectively. As a result of size quantization, an energy gap opens with a comparable magnitude in both systems. Additionally, energy spectra look almost identical, in a sense of the degeneracy of consecutive levels. Starting from the Fermi level, we observe first double degenerate state, next two single and two degenerate levels in both cases. Thus, one can conclude that the shape of graphene quantum dots with armchair edges does not play an important role. In Fig. 2.2(c) and (d) energy spectra for structures with zigzag edges are shown, with hexagonal and triangular shapes, respectively. The energy gap in a hexagonal dot with zigzag edges is smaller compared to the energy gap present in the armchair quantum dot. On the other hand, in the triangular graphene quantum dot (TGQD) with zigzag edges, a degenerate shell at the Fermi level appears (7 degenerate states in this case). A detailed analysis of the energy spectra of TGQDs will be presented in Section 2.2.

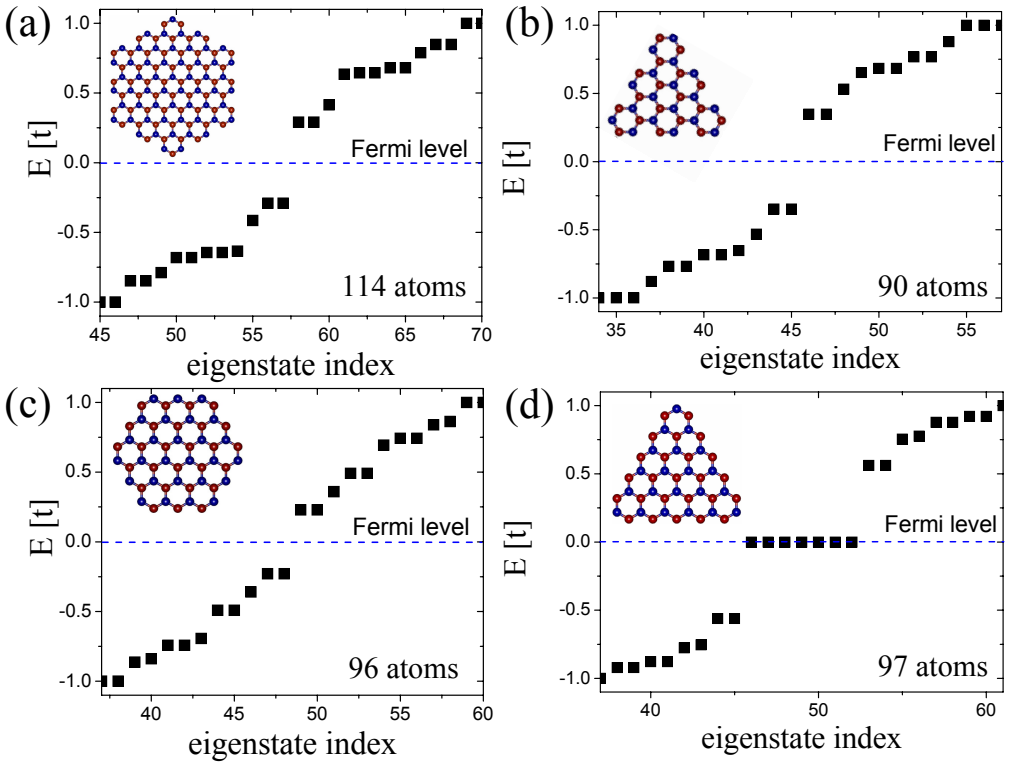

Figure 2.2: TB energy spectra in the vicinity of the Fermi level, $E = 0$, for graphene quantum dots with a similar number of atoms, $N \sim 100$, but different shapes and edges. Energy spectra for (a) hexagonal and (b) triangular quantum dots with armchair edges, and for (c) hexagonal and (d) triangular quantum dots with zigzag edges. Edge effects appear only in systems with zigzag edges.

In Fig. 2.3, electronic densities of the highest valence energy levels corresponding to structures with the energy spectra shown in Fig. 2.2 are presented. In all presented systems, these states are doubly degenerate, thus we plot a sum of electronic densities of these two states. Thanks to that, electronic densities preserve a symmetry of systems. We also note that identical electronic densities are obtained for the lowest energy levels from the conduction band. Eigenfunctions for a valence state Ψ_v with an energy $E_v = -|E|$ and for a conduction state Ψ_c with an energy $E_v = |E|$ are identical on lattice sites corresponding to sublattice A, and have opposite signs on lattice sites corresponding to sublattice B. This fact was also seen in the case of eigenstates of infinite graphene at Γ point, Eq. (1.12) and Eq. (1.13). Thus, electronic densities defined as $|\Psi|^2$ are identical in both cases. For the hexagonal structure with armchair edges, Fig. 2.3(a), an electronic density spreads over the entire structure. Starting from the center, alternating hexagons with an increasing size characterized by higher and lower densities are seen. In the triangular structure with armchair edges, Fig. 2.3(b), the electronic density is localized in the center of the structure, avoiding corners. A large concentration of the density with a triangular shape rotated by $\frac{\pi}{6}$ with respect to the corners is observed. In Fig. 2.3(c), the electronic density of valence states for the hexagonal dot with zigzag edges is plotted. These states are strongly localized on six edges. We note that observed edge effects are responsible for faster closing of an energy gap with increasing size with respect to systems with armchair edges. This statement can be confirmed by comparing energy gaps from Fig. 2.2(c) with (a) and (b). The energy gap as a function of size will be studied in detail in Sec. 5.1. On the other hand, no edge effects are observed in Fig. 2.3(d), in TGQD with zigzag edges. Here, the electronic density of highest valence states is localized in the center of the structure. However, in this system a degenerate shell appears. In Sec. 2.3.1 we show that edge states in TGQD collapse to this degenerate shell. We note that similar patterns of electronic densities plotted in Fig. 2.3 were observed in larger structures for quantum dots with all considered shapes.

In Fig. 2.4 the density of states (DOS) for GQD consisting of around 600 atoms with different shapes is plotted. Due to a similarity between energy spectra from Fig. 2.2(a) and (b), for hexagonal and triangular dots with armchair edges, only DOS for the first one is shown. In order to smooth the discrete energy spectra, we use a Gaussian function $f(E) = \exp\left(-(E - E_i)^2/\Gamma^2\right)$ with a broadening $\Gamma = 0.024|t|$. DOS for a system with armchair edges and $N = 546$ atoms vanishes close to the energy E=0, in analogy with infinite graphene (not

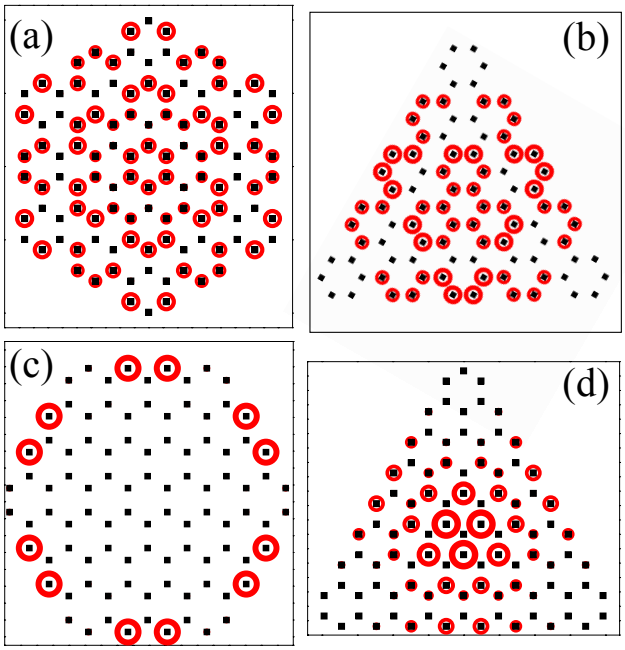

Figure 2.3: Electronic densities of the highest valence energy levels corresponding to structures with the energy spectra shown in Fig. 2.2. Only in hexagonal structure with zigzag edges on (c), these states are edge states.

shown). Systems with zigzag edges have an additional contribution from edge states, seen as peaks at $E = 0$ point. This peak is significantly higher for TGQD, $N = 622$ atoms, comparing to the hexagonal dot, $N = 600$ atoms, due to a collapse of edge states to the degenerate shell with the energy E=0. Farther from the Fermi level, DOS looks similarly for quantum dots with all shapes and is comparable to DOS for infinite graphene, with characteristic van Hove singularities at $E = \pm t$.

2.2 Triangular graphene quantum dots with zigzag edges

2.2.1 Energy spectrum

In Sec. 2.1.1, we have shown that an energy spectrum of TGQDs is characterized by the degenerate shell. We carry out a detail analysis of single particle properties of these systems, but first we describe their atomic structure. Each TGQD can be characterized by the number of atoms on the one edge N_{edge}. The total number of atoms in the structure is given by

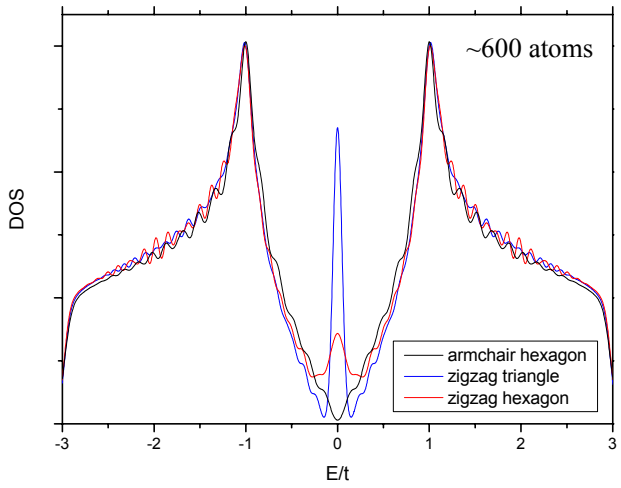

Figure 2.4: The density of states (DOS) for GQD consisting of around $N = 600$ atoms with different shapes. DOS for the system with armchair edges vanishes close to the energy $E = 0$, in analogy with infinite graphene. Systems with zigzag edges have an additional contribution from edge states, seen as a peak at $E = 0$ point.

$N = N_{edge}^2 + 4N_{edge} + 1$. Additionally, a difference between the number of atoms corresponding to each sublattice, A and B, changes with a size and can be written as $N_A - N_B = N_{edge} - 1$, N_A and N_B is the number of A and B type of atoms. This feature is crucial for the explanation of an origin of the degeneracy in TB energy spectra which will be done in Sec. 2.2.2.

In Fig. 2.5 TB energy spectra of two TGQDs with different sizes are shown. Fig. 2.5(a) corresponds to the structure consisting of $N = 78$ atoms or $N_{edge} = 7$ and Fig. 2.5(b) to the structure consisting of $N = 97$ atoms or $N_{edge} = 8$. There are $N_{deg} = 6$ and $N_{deg} = 7$ degenerate states on the Fermi level, respectively. The number of degenerate states N_{deg} in these structures is related to the number edge atoms as $N_{deg} = N_{edge} - 1 = N_A - N_B$. In next subsection, we show that this is a general rule for all TGQDs. By increasing the size of triangles, the degeneracy of a zero-energy shell increases.

We study the electronic densities corresponding to the degenerate zero-energy levels. We focus on the structure with $N = 97$ atoms and the energy spectrum shown in Fig. 2.5(b). There are $N_{deg} = 7$ degenerate energy levels. Due to a perfect degeneracy of these states, arbitrary linear combinations of eigenfunctions giving seven linear independent vectors can be constructed. Thus, in order to preserve a triangular symmetry of eigenstates, the degeneracy is slightly removed by applying a very small random energy shift on each atomic

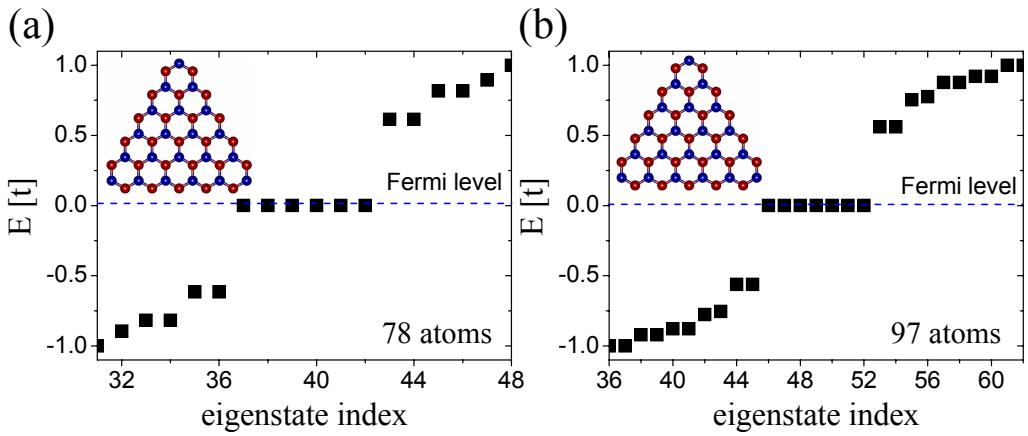

Figure 2.5: TB energy spectra of TGQDs consisting of (a) $N = 78$ atoms ($N_{edge} = 7$) and $N = 97$ atoms ($N_{edge} = 8$). There are (a) $N_{deg} = 6$ and (b) $N_{deg} = 7$ degenerate states on the Fermi level.

site. Thanks to that, the seven-fold degeneracy is slightly removed into two doubly degenerate and three non-degenerate states, with electronic densities shown in Fig. 2.6(a-e). A radius of circles is proportional to the electronic density on an atomic site. In the case of the double degenerate state, a sum of electronic densities corresponding to these two states is plotted. For single states, a scaling factor is two times larger than for doubly degenerate states. Five of these states, Fig. 2.6(a-c), are strongly localized on edges. Last two states, shown in Fig. 2.6(d) and (e), fill the center of the triangle and a center of edges avoiding corners. While these two states contribute to the electronic density of the center of the triangle, it is small in comparison to the electronic density localized on edges. This is shown in Fig. 2.6(f), where the total charge density of the zero-energy shell is plotted. Proportions between Fig. 2.6(a-e) and Fig. 2.6(f) are not maintained. We note that all states are localized only on A sublattice, indicated by red color.

2.2.2 Analytical solution to zero-energy states

The results, presented in this section, were published in a paper "Zero-energy states in triangular and trapezoidal graphene structures", by P. Potasz, A. D. Güçlü, and P. Hawrylak, Ref. [145].

Our goal is to find zero-energy solutions to TB Hamiltonian given by Eq. 2.1. This corresponds to solving a singular eigenvalue problem and can be

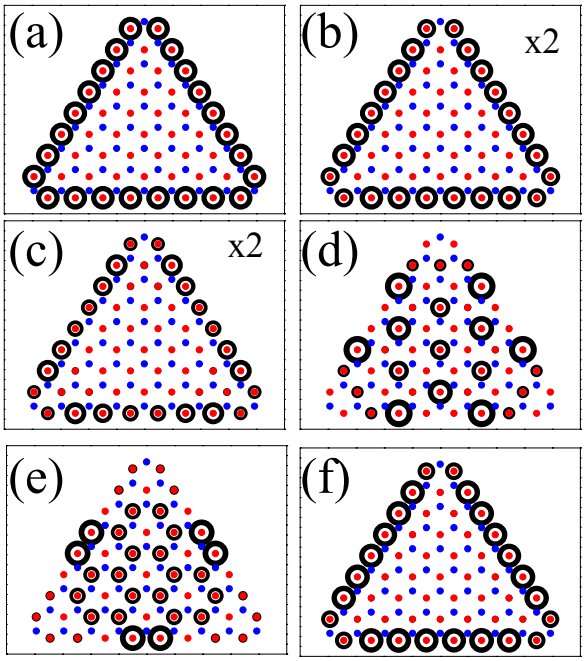

Figure 2.6: (a-e) Electronic densities of $N_{deg} = 7$ degenerate energy levels with $E = 0$ for structure consisting of $N = 97$ atoms. (a-c) Five states strongly localized on edges. (d-e) Two states localized in the center of the triangle. (f) The total charge density of the zero-energy shell. All states are localized only on A sublattice, indicated by red color. A radius of black circles is proportional to the electronic density on an atomic site.

written as

$$H_{TB}\Psi = 0. \tag{2.2}$$

In this case, there is no coupling between two sublattices, which can be seen also from Eq. (1.4) for infinite graphene. A given row of a Hamiltonian matrix, e. g. corresponding to i-th A-type orbital, contains only nonzero elements in j-th columns, corresponding to neighboring B-type orbitals. Acting by the Hamiltonian matrix on an arbitrary vector Ψ written in a basis of localized ϕ_z orbitals, one gets a set of equations for searching expansion b_n coefficients. Each equation, for a given site i, e. g. A-type, is a sum of coefficients b_j corresponding to B-type nearest neighbors multiplied by matrix elements, equated to zero. However, all matrix elements are equal due to a constant hopping integral and can be eliminated from the equations. Thus, the equations for searching expansion coefficients can be written as

$$\sum_{<i,j>} b_j = 0, \tag{2.3}$$

The summation is over j-th nearest neighbors of the atom i, and we dropped a summation over spins. In other words, the sum of coefficients around each site must vanish. Eqs. (2.3) are independent for A-type and B-type atoms. Let us first focus on the sublattice labeled by A, represented by red colors in Fig. 2.7, where TGQD with $N = 33$ atoms is plotted. For convenience, each atom is labeled by two integer numbers n and m with $0 \leq n, m \leq N_{edge} + 1$. We added to the structure three auxiliary atoms, which will later help to introduce boundary conditions. They are indicated by open circles in Fig. 2.7. We will now show that coefficients $b_{n,m}$ for all atoms in the triangle can be expressed as a linear combination of coefficients corresponding to atoms on one edge, i.e., $b_{n,0}$ from a bottom row of atoms in Fig. 2.7. When we take the first two coefficients on the left from the bottom row, $b_{0,0}$ and $b_{1,0}$, we can obtain one coefficient from the second row, $b_{0,1}$. By using Eq. (2.3) it can be written as $b_{0,1} = -(b_{0,0} + b_{1,0})$. We can take also coefficients $b_{1,0}$ and $b_{2,0}$, and obtain coefficient $b_{1,1}$, which can be written as $b_{1,1} = -(b_{1,0} + b_{2,0})$. In this way, we can calculate all coefficients from the second row using coefficients from the bottom row. They are just equal to the sum of two lower lying coefficients with a minus sign. Having all coefficients from the second row, using the same method, we can obtain all coefficients corresponding to atoms in the third row. For the first coefficient on the left from the third row we obtain $b_{0,2} = -(b_{0,1} + b_{1,1}) = (b_{0,0} + 2b_{1,0} + b_{2,0})$. The second coefficient on the left

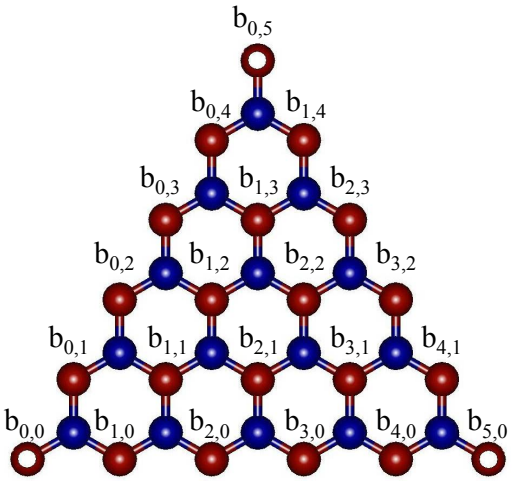

Figure 2.7: TGQD with $N_{edge} = 4$ atoms on the one edge. Under each A–type atom are corresponding coefficients. Open circles indicate auxiliary A–type atoms in the three corners, which will help to introduce three boundary conditions. For zero-energy states all coefficients can be expressed as superpositions of coefficients from the one edge (the lowest row of atoms in our case).

from the third row can be written as $b_{1,2} = -(b_{1,1} + b_{2,1}) = (b_{1,0} + 2b_{2,0} + b_{3,0})$. These coefficients are also expressed using coefficients from the bottom row. In this way, all coefficients from the third row can be obtained. By going rows one by one, we can obtain all coefficients in the structure regardless of the size of the triangle. One can see that coefficients from a given row are expressed by using similar formulas. Similar to the construction of Pascal triangle, these coefficients can be written in a suitable form using binomial coefficients

$$b_{n,m} = (-1)^m \sum_{k=0}^{m} \begin{pmatrix} m \\ k \end{pmatrix} b_{n+k,0}. \tag{2.4}$$

Here, it is important to emphasize that the only unknown are the $N_{edge} + 2$ coefficients ($b_{n,0}$'s) from the first, the bottom row; the rest are expressed as their superpositions, as it is seen from Eq. (2.4). In addition, we must use the boundary conditions: the wave function has to vanishes on three auxiliary atoms in each corner, see Fig. 2.7. This gives three boundary conditions ($b_{0,0} = b_{N_{edge}+1,0} = b_{0,N_{edge}+1} = 0$), reducing the number of independent coefficients to $N_{edge} - 1$. The number of linear independent coefficients corresponds to the maximal number of created linear independent vectors - a dimension of linear space.

The same analysis can be done for B-type atoms indicated by blue (dark grey) circles. In this case, it is convenient to include some of boundary con-

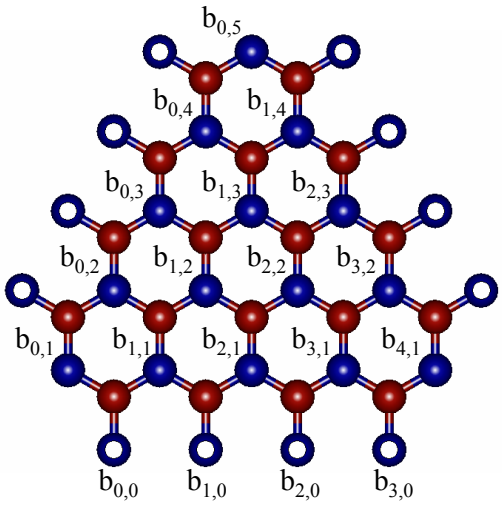

Figure 2.8: TGQD from Fig. 2.7. Above each B–type atom (indicated by blue circles) are corresponding coefficients. We only left coefficients corresponding to auxiliary B–type atoms from the bottom. For zero-energy states, a coefficient from lower left corner ($b_{0,1}$) determines all other coefficients. Introducing four boundary conditions from auxiliary atoms, we obtain only trivial solution.

ditions at the beginning as shown in Fig. 2.8, where we only keep coefficients belonging to auxiliary atoms from the bottom edge. As a consequence, the coefficient $b_{0,1}$ determines all other coefficients in the triangle. Since there are four auxiliary atoms (equivalently four boundary conditions) but only one independent coefficient, we can not obtain any nontrivial solution. Hence, zero-energy states can only consist of coefficients of one type of atoms – these lying on the edges (A-type atoms). A general form for the eigenvectors for zero-energy states in the triangle can be written as

$$\Psi_{E=0} = \sum_{n=0}^{N_{edge}+1} \sum_{m=0}^{N_{edge}+1-n} \left[(-1)^m \sum_{k=0}^{m} \begin{pmatrix} m \\ k \end{pmatrix} b_{n+k,0} \right] \phi^A_{n,m}, \tag{2.5}$$

where N_{edge} is the number of atoms on the one edge and $\phi^A_{n,m}$ is p_z orbital on A-type site (n, m). In this expression the only $N_{edge}-1$ coefficients corresponding to atoms from the first, the bottom row are independent. We can construct $N_{edge} - 1$ linear independent eigenvectors, which span the subspace with zero-energy states. Thus, the number of zero-energy states in the triangle is $N_{deg} = N_{edge} - 1$. This can be also related to the imbalance between the number of atoms belonging to each sublattice, $N_{deg} = N_A - N_B$.

Using the Eq. (2.5) we can then construct an orthonormal basis for zero-energy states. First, we make a choice for the N_{deg} independent coefficients

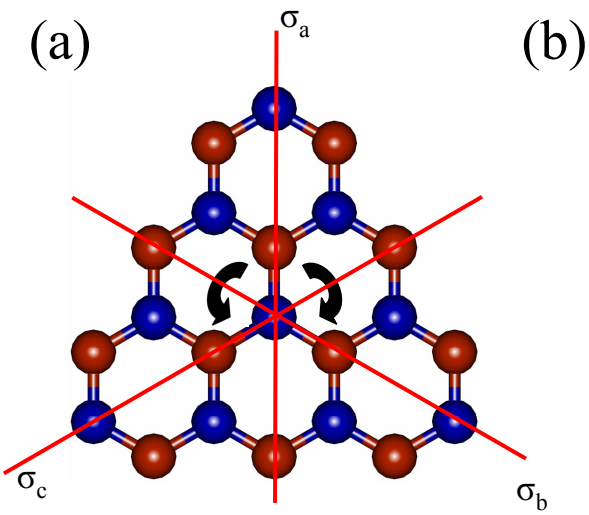

	E	$2C_3$	$3\sigma_v$
A_1	1	1	1
A_2	1	1	−1
E	2	−1	0

Figure 2.9: (a) TGQD with all symmetry operations in a C_{3v} symmetry group. Three red lines correspond to three reflection planes and two black arrows correspond to two rotations over $2\pi/3$. (b) Character table of the C_{3v} symmetry group.

$b_{n,0}$, from which we obtain N_{deg} linear independent vectors, for instance by choosing only one nonzero coefficient for all N_{deg} collections, different one for each eigenvector. Resulting eigenvectors can then be orthogonalized using standard Gram-Schmidt process. The last step is the normalization K_{norm} of the eigenvectors, using expression

$$K_{norm} = \sum_{n=0}^{N_{edge}+1} \sum_{m=0}^{N_{edge}+1-n} \left| \sum_{k=0}^{m} \binom{m}{k} b_{n+k,0} \right|^2 .$$

2.2.3 Classification of states with respect to irreducible representations of C_{3v} symmetry group

TGQDs are structures with well defined symmetry. They transform according to symmetry operations of an equilateral triangle, which correspond to the C_{3v} symmetry group. There are six symmetry operations in the group, shown in Fig. 2.9(a): identity $\hat{E}$, three reflections $\hat{\sigma_a}$, $\hat{\sigma_b}$, $\hat{\sigma_c}$ with respect to planes going along secants of three triangle's angles, and two rotations $\hat{C}_{1,2}$ over $\pm 2\pi/3$ with a rotational axis going through the center of the triangle. In the Hilbert space, symmetry operators can be represented by unitary matrices. These matrices are called matrix representations of operators. All these matrices commute with a TB Hamiltonian matrix: $[H_{TB}, \sigma_\nu] = [H_{TB}, C_i] = 0$, with $\nu = a, b, c$ and $i = 1, 2$, where we used the same notation for operators in a ma-

trix representation as for symmetry operations. Thus, it is possible to classify energy states according to eigenvalues of symmetry operators. For example, a matrix corresponding to a reflection operator can have two eigenvalues, $+1$ and -1. One can find eigenstates of TB Hamiltonian which change (an antisymmetric state) or not (a symmetric state) a sign of the eigenfunctions under a reflection with respect to one of three reflection planes. We want to classify states not with respect to a single operator but with respect to all symmetry operators in a given group. In other words, one has to find a set of basis vectors, which in a simple situation of non-degenerate states (we concentrate on a degeneracy related to the symmetry of the system, not on an accidental degeneracy), do not mix with each other after transformation under all symmetry operations. In this basis, all symmetry operators will be represented by block diagonal matrices. In the case of 1×1 block, after acting on an arbitrary basis vector, there will be no mixing with other basis vectors. In the case of $n \times n$ block, there can be mixing only between n vectors. Such representations are called reducible and blocks correspond to the so called irreducible representations and can not be reduced at the same time for all symmetry operators by any transformation of the basis vectors.

In Fig. 2.9(b), a character table corresponding to the C_{3v} symmetry group is shown. Left column contains three irreducible representations labeled as A_1, A_2, E. Top row corresponds to symmetry operators divided into three classes. Elements of the table are characters of irreducible representations, which are traces of matrices in this case. Characters corresponding to the identity operator $\hat{E}$, which is always represented by the unit matrix, determine the dimension of the irreducible representation. Thus, the irreducible representations A_1, A_2 are one dimensional while the irreducible representation E is two dimensional. Characters for other symmetry operators describe how basis vectors behave after transformation under symmetry operators. Elements from a given class always behave in the same way. Basis vectors transforming according to A_1 irreducible representation do not change, while these transforming according to A_2 irreducible representation change sign under three reflections. Thus, basis vectors transforming according to A_1 irreducible representation are fully symmetric while these transforming according to A_2 irreducible representation are fully antisymmetric, what is schematically shown in Fig. 2.10(a) and (b), respectively. In the case of 2D irreducible representation E situation is more complicated because different linear combinations of two basis vectors can be chosen. One of the choice is such that one basis vector changes sign, and the second one does not, under reflection giving character (trace) of the represen-

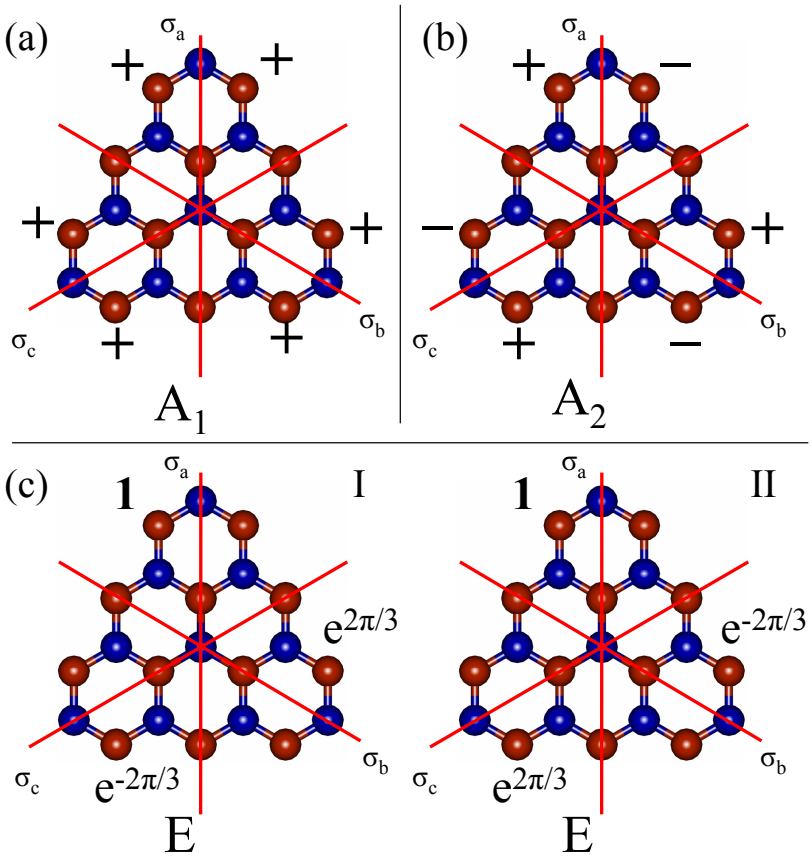

Figure 2.10: Basis vectors constructed as linear combinations of p_z orbitals of TGQD can be classified according to irreducible representations of the symmetry group. (a) Vectors transforming according to A_1 irreducible representation do not change sign under three reflections (fully symmetric states). (b) Vectors transforming according to A_2 irreducible representation change sign under three reflections (fully antisymmetric states). (c) Vectors transforming according to E irreducible representation acquire extra phase $e^{\pm 2\pi/3}$ under rotations.

tation matrix equal to zero in agreement with the character table. On the other hand, one can choose two basis vectors of irreducible representation E such that they acquire extra phase $e^{2\pi/3}$ under rotations, schematically shown in Fig. 2.10(c).

We estimate the number of basis vectors transforming according to each irreducible representation. It can be calculated using a following formula [171]

$$a_\Gamma = \frac{1}{h}\sum_i \chi(\hat{R}_i)\chi_\Gamma(\hat{R}_i), \tag{2.6}$$

where $\Gamma = A_1, A_2, E$, $h = 6$ is a number of elements in the group, $\chi(\hat{R}_i)$ and $\chi_\Gamma(\hat{R}_i)$ are characters of the symmetry operator $\hat{R}_i$ of reducible and irreducible

representations, respectively. Characters of the reducible representation can be easily evaluate: it is the number of orbitals which remain unchanged under a given symmetry operation. For example, for a triangle from Fig. 2.9(a), $\chi(C_{1,2}) = 1$ and $\chi(\sigma_{a,b,c}) = 4$, and $\chi(E) = 22$ as the number of atoms. Thus, using Eq. (2.6) one can get

$$a_{A_1} = 6$$
$$a_{A_2} = 2$$
$$a_E = 7.$$

We can now construct basis vectors for each irreducible representation. A following formula for unnormalized basis vectors is used [171]

$$\Psi_n^{\Gamma} = \sum_i D_{\Gamma}(\hat{R}_i)\hat{R}_i\phi_j, \tag{2.7}$$

where $D_{\Gamma}(\hat{R}_i)$ is a matrix of an operator $\hat{R}_i$ for Γ irreducible representation. Index j run over all 22 atomic orbitals but, e.g. for A_1 subspace, only $a_{A_1} = 6$ linear independent vectors will be obtained, thus $n = 1, 2, ..., 6$. We use indices of p_z orbitals from Fig. 2.1. We apply Eq. 2.7 first to ϕ_0 and ϕ_1 which for A_1 representation gives

$$\begin{aligned}
\Psi_1^{A_1} &= 1\cdot\hat{E}\phi_0 + 1\cdot\hat{\sigma_a}\phi_0 + 1\cdot\hat{\sigma_b}\phi_0 + 1\cdot\hat{\sigma_c}\phi_0 + 1\cdot\hat{C}_1\phi_0 + 1\cdot\hat{C}_2\phi_0 = 6\phi_0 \\
\Psi_2^{A_1} &= 1\cdot\hat{E}\phi_1 + 1\cdot\hat{\sigma_a}\phi_1 + 1\cdot\hat{\sigma_b}\phi_1 + 1\cdot\hat{\sigma_c}\phi_1 + 1\cdot\hat{C}_1\phi_1 + 1\cdot\hat{C}_2\phi_1 \\
&= \phi_1 + \phi_8 + \phi_1 + \phi_{15} + \phi_8 + \phi_{15} = 2(\phi_1 + \phi_8 + \phi_{15}),
\end{aligned} \tag{2.8}$$

where in Eq. (2.7) $D_{A_1}(\hat{R}_i) = 1$ for all symmetry operators according to the character table shown in Fig. 2.9(b). With a help of Fig. 2.1, it is easy to see that $\Psi_2^{A_1}$ can be also obtained by starting from ϕ_8 or ϕ_{15} orbitals. From this we can conclude that all A_1 basis vectors can be obtained using Eq. (2.7), starting from ϕ_j for $j = 0, 2, ..., 5$, see Fig. 2.1. All these orbitals lie in one part of a triangle and can not be transformed one into another by any symmetry operations. We can write A_1 basis vectors after normalization as

$$\begin{aligned}
\Psi_1^{A_1} &= \phi_0 \\
\Psi_2^{A_1} &= \frac{1}{\sqrt{3}}(\phi_1 + \phi_8 + \phi_{15}) \\
\Psi_3^{A_1} &= \frac{1}{\sqrt{3}}(\phi_2 + \phi_9 + \phi_{16}) \\
\Psi_4^{A_1} &= \frac{1}{\sqrt{6}}(\phi_3 + \phi_{21} + \phi_{14} + \phi_7 + \phi_{10} + \phi_{17}) \\
\Psi_5^{A_1} &= \frac{1}{\sqrt{6}}(\phi_4 + \phi_{20} + \phi_{13} + \phi_6 + \phi_{11} + \phi_{18}) \\
\Psi_6^{A_1} &= \frac{1}{\sqrt{3}}(\phi_5 + \phi_{19} + \phi_{12}).
\end{aligned}$$

These states are fully symmetric which was schematically shown in Fig. 2.10(a) In a similar way, one can construct basis vectors transforming according to irreducible representation A_2. We apply Eq. 2.7 first, e.g. to ϕ_2 and ϕ_4, getting

$$\begin{aligned}
\Psi_1^{A_2} &= 1\cdot\hat{E}\phi_2 - 1\cdot\hat{\sigma_a}\phi_2 - 1\cdot\hat{\sigma_b}\phi_2 - 1\cdot\hat{\sigma_c}\phi_2 + 1\cdot\hat{C_1}\phi_2 + 1\cdot\hat{C_2}\phi_2 \\
&= \phi_2 - \phi_9 - \phi_2 - \phi_{16} + \phi_9 + \phi_{16} = 0 \\
\Psi_2^{A_2} &= 1\cdot\hat{E}\phi_4 - 1\cdot\hat{\sigma_a}\phi_4 - 1\cdot\hat{\sigma_b}\phi_4 - 1\cdot\hat{\sigma_c}\phi_4 + 1\cdot\hat{C_1}\phi_4 + 1\cdot\hat{C_2}\phi_4 \\
&= \phi_4 - \phi_{20} - \phi_{13} - \phi_6 + \phi_{11} + \phi_{18}, \qquad (2.9)
\end{aligned}$$

where $D_{A_2}(\sigma_\nu) = -1$ and $D_{A_2}(C_i) = 1$ according to the character table shown in Fig. 2.9(b). First vector vanishes identically. This gives a clue that starting orbital can not lie on a line associated with one of reflection planes. We have only $a_{A_2} = 2$ basis vectors, and second one can be obtained starting from ϕ_3. We can write A_2 basis vectors after normalization as

$$\begin{aligned}
\Psi_1^{A_2} &= \frac{1}{\sqrt{6}}\left(\phi_3 - \phi_{21} - \phi_{14} - \phi_7 + \phi_{10} + \phi_{17}\right) \\
\Psi_2^{A_2} &= \frac{1}{\sqrt{6}}\left(\phi_4 - \phi_{20} - \phi_{13} - \phi_6 + \phi_{11} + \phi_{18}\right).
\end{aligned}$$

These states are fully antisymmetric which was schematically shown in Fig. 2.10(b).

We construct basis vectors transforming according to irreducible representation E. In order to do this, we define irreducible representations for symmetry operators because only characters of these matrices are known, see Fig. 2.9(b). We choose following unitary matrices

$$\begin{aligned}
D_E(\hat{E}) &= \begin{pmatrix} 1 & 0 \\ 0 & 1 \end{pmatrix}, D_E(\hat{\sigma_a}) = \begin{pmatrix} 0 & 1 \\ 1 & 0 \end{pmatrix}, \\
D_E(\hat{\sigma_b}) &= \begin{pmatrix} 0 & e^{-2i\pi/3} \\ e^{2i\pi/3} & 0 \end{pmatrix}, D_E(\hat{\sigma_c}) = \begin{pmatrix} 0 & e^{2i\pi/3} \\ e^{-2i\pi/3} & 0 \end{pmatrix}, \\
D_E(\hat{C_1}) &= \begin{pmatrix} e^{2i\pi/3} & 0 \\ 0 & e^{-2i\pi/3} \end{pmatrix}, D_E(\hat{C_2}) = \begin{pmatrix} e^{-2i\pi/3} & 0 \\ 0 & e^{2i\pi/3} \end{pmatrix}. \qquad (2.10)
\end{aligned}$$

We apply Eq. 2.7 first to ϕ_1. We have four matrix elements in each matrix

2.10, so we obtain four functions

$$\begin{aligned}
{}^{11}\Psi_1^E &= {}^{11}D_E(\hat{E})\hat{E}\phi_1 + {}^{11}D_E(\hat{\sigma}_a)\hat{\sigma}_a\phi_1 + {}^{11}D_E(\hat{\sigma}_b)\hat{\sigma}_b\phi_1 \\
&+ {}^{11}D_E(\hat{\sigma}_c)\hat{\sigma}_c\phi_1 + {}^{11}D_E(\hat{C}_1)\hat{C}_1\phi_1 + {}^{11}D_E(\hat{C}_2)\hat{C}_2\phi_1 \\
&= 1\cdot\phi_1 + 0\cdot\phi_1 + 0\cdot\phi_{15} + 0\cdot\phi_8 + e^{-2i\pi/3}\cdot\phi_8 + e^{2i\pi/3}\cdot\phi_{15} \\
&= \phi_1 + e^{-2i\pi/3}\phi_8 + e^{2i\pi/3}\phi_{15} \\
{}^{12}\Psi_1^E &= {}^{12}D_E(\hat{E})\hat{E}\phi_1 + {}^{12}D_E(\hat{\sigma}_a)\hat{\sigma}_a\phi_1 + {}^{12}D_E(\hat{\sigma}_b)\hat{\sigma}_b\phi_1 \\
&+ {}^{12}D_E(\hat{\sigma}_c)\hat{\sigma}_c\phi_1 + {}^{12}D_E(\hat{C}_1)\hat{C}_1\phi_1 + {}^{12}D_E(\hat{C}_2)\hat{C}_2\phi_1 \\
&= 0\cdot\phi_1 + e^{-2i\pi/3}\cdot\phi_1 + 1\cdot\phi_{15} + e^{2i\pi/3}\cdot\phi_8 + 0\cdot\phi_8 + 0\cdot\phi_{15} \\
&= e^{-2i\pi/3}\phi_1 + e^{2i\pi/3}\phi_8 + \phi_{15} = e^{-2i\pi/3}\left(\phi_1 + e^{-2i\pi/3}\phi_8 + e^{2i\pi/3}\phi_{15}\right)
\end{aligned}$$

$$\begin{aligned}
{}^{21}\Psi_1^E &= {}^{21}D_E(\hat{E})\hat{E}\phi_1 + {}^{21}D_E(\hat{\sigma}_a)\hat{\sigma}_a\phi_1 + {}^{21}D_E(\hat{\sigma}_b)\hat{\sigma}_b\phi_1 \\
&+ {}^{21}D_E(\hat{\sigma}_c)\hat{\sigma}_c\phi_1 + {}^{21}D_E(\hat{C}_1)\hat{C}_1\phi_1 + {}^{21}D_E(\hat{C}_2)\hat{C}_2\phi_1 \\
&= 0\cdot\phi_1 + e^{2i\pi/3}\cdot\phi_1 + 1\cdot\phi_{15} + e^{-2i\pi/3}\cdot\phi_8 + 0\cdot\phi_8 + 0\cdot\phi_{15} \\
&= e^{2i\pi/3}\phi_1 + e^{-2i\pi/3}\phi_8 + \phi_{15} = e^{2i\pi/3}\left(\phi_1 + e^{2i\pi/3}\phi_8 + e^{-2i\pi/3}\phi_{15}\right) \\
{}^{22}\Psi_1^E &= {}^{22}D_E(\hat{E})\hat{E}\phi_1 + {}^{22}D_E(\hat{\sigma}_a)\hat{\sigma}_a\phi_1 + {}^{22}D_E(\hat{\sigma}_b)\hat{\sigma}_b\phi_1 \\
&+ {}^{22}D_E(\hat{\sigma}_c)\hat{\sigma}_c\phi_1 + {}^{22}D_E(\hat{C}_1)\hat{C}_1\phi_1 + {}^{22}D_E(\hat{C}_2)\hat{C}_2\phi_1 \\
&= 1\cdot\phi_1 + 0\cdot\phi_1 + 0\cdot\phi_{15} + 0\cdot\phi_8 + e^{2i\pi/3}\cdot\phi_8 + e^{-2i\pi/3}\cdot\phi_{15} \\
&= \phi_1 + e^{2i\pi/3}\phi_8 + e^{-2i\pi/3}\phi_{15}.
\end{aligned}$$

It is clearly seen that ${}^{11}\Psi_1^E$ and ${}^{12}\Psi_1^E$ are linearly dependent. Similarly ${}^{21}\Psi_1^E$ and ${}^{22}\Psi_1^E$ are linearly dependent. Thus, two linear independent basis vectors can be chosen as

$$\begin{aligned}
\Psi_{11}^E = {}^{11}\Psi_1^E &= \phi_1 + e^{-2i\pi/3}\phi_8 + e^{2i\pi/3}\phi_{15} \\
\Psi_{12}^E = {}^{22}\Psi_1^E &= \phi_1 + e^{2i\pi/3}\phi_8 + e^{-2i\pi/3}\phi_{15}.
\end{aligned}$$

We see that orbitals in these vectors are obtained by starting from one and rotating it over $\pm 2\pi/3$. Thus, all E basis vectors can be found starting from orbitals ϕ_j for $j = 1, 2, ..., 7$, which lie in 1/3 of the triangle and can not be transformed one into another by any of two rotations, see Fig. 2.1. These vectors with appropriate normalization, with a help of Fig. 2.1, can be shortly written as

$$\begin{aligned}
\Psi_{j1}^E &= \frac{1}{\sqrt{3}}\left(\phi_j + e^{-2i\pi/3}\phi_{j+7} + e^{2i\pi/3}\phi_{j+14}\right) \\
\Psi_{j2}^E &= \frac{1}{\sqrt{3}}\left(\phi_j + e^{2i\pi/3}\phi_{j+7} + e^{-2i\pi/3}\phi_{j+14}\right),
\end{aligned}$$

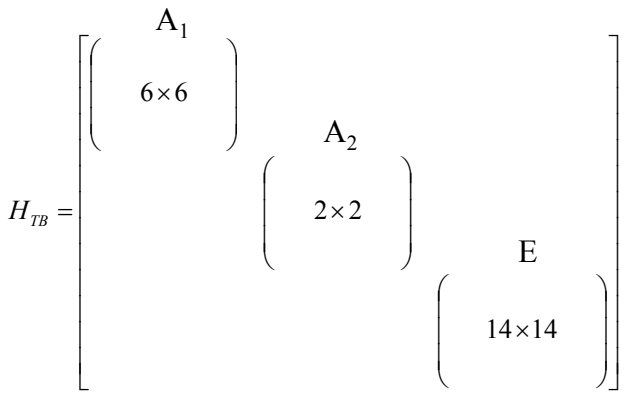

Figure 2.11: The scheme of a TB Hamiltonian matrix written in a basis of vectors transforming according to irreducible representation of an equilateral triangle. The matrix takes a block diagonal form.

for $j = 1, 2, ..., 7$. Having all basis vectors, a TB Hamiltonian matrix has a block diagonal form, shown in Fig. 2.11. Three blocks corresponding to each irreducible representation are visible. Matrix elements between basis vectors transforming according to different irreducible representations vanish identically. For example, for $\langle \Psi_3^{A_1} | H_{TB} | \Psi_{11}^{E} \rangle$ one gets

$$\begin{aligned}\langle \Psi_3^{A_1} | H_{TB} | \Psi_{11}^{E} \rangle &= \frac{1}{3}(\langle \phi_2 | H_{TB} | \phi_1 \rangle + e^{-2i\pi/3} \langle \phi_2 | H_{TB} | \phi_8 \rangle + e^{2i\pi/3} \langle \phi_2 | H_{TB} | \phi_{15} \rangle \\ &+ \langle \phi_9 | H_{TB} | \phi_1 \rangle + e^{-2i\pi/3} \langle \phi_9 | H_{TB} | \phi_8 \rangle + e^{2i\pi/3} \langle \phi_9 | H_{TB} | \phi_{15} \rangle \\ &+ \langle \phi_{16} | H_{TB} | \phi_1 \rangle + e^{-2i\pi/3} \langle \phi_{16} | H_{TB} | \phi_8 \rangle + e^{2i\pi/3} \langle \phi_{16} | H_{TB} | \phi_{15} \rangle),\end{aligned}$$

where due to the symmetry of the system

$$\begin{aligned}\langle \phi_2 | H_{TB} | \phi_1 \rangle &= \langle \phi_9 | H_{TB} | \phi_8 \rangle = \langle \phi_{16} | H_{TB} | \phi_{15} \rangle, \\ \langle \phi_2 | H_{TB} | \phi_8 \rangle &= \langle \phi_9 | H_{TB} | \phi_{15} \rangle = \langle \phi_{16} | H_{TB} | \phi_8 \rangle, \\ \langle \phi_2 | H_{TB} | \phi_{15} \rangle &= \langle \phi_9 | H_{TB} | \phi_1 \rangle = \langle \phi_{16} | H_{TB} | \phi_1 \rangle, \end{aligned} \tag{2.11}$$

which was obtained with a help of Fig. 2.1. Finally, one gets

$$\begin{aligned}\langle \Psi_3^{A_1} | H_{TB} | \Psi_{11}^{E} \rangle &= \frac{1}{3}(\langle \phi_2 | H_{TB} | \phi_1 \rangle \left(1 + e^{-2i\pi/3} + e^{2i\pi/3}\right) \\ &+ \langle \phi_2 | H_{TB} | \phi_8 \rangle \left(1 + e^{-2i\pi/3} + e^{2i\pi/3}\right) \\ &+ \langle \phi_2 | H_{TB} | \phi_1 5 \rangle \left(1 + e^{-2i\pi/3} + e^{2i\pi/3}\right) = 0,\end{aligned}$$

for arbitrary matrix elements because $1 + e^{-2i\pi/3} + e^{2i\pi/3} = 0$.

In Fig. 2.12(a) we show energy spectrum for the structure from Fig. 2.9(a) with classified symmetries of eigenstates. There are $N_{deg} = 2$ degenerate zero-energy states. They transform according to E irreducible representation. The

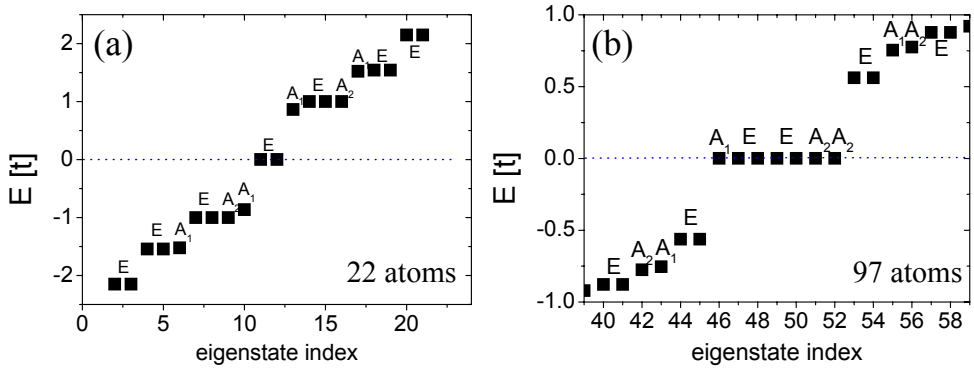

Figure 2.12: Energy spectra of TB Hamiltonian for TGQDs with (a) $N = 22$ and (b) $N = 97$ atoms. Each energy level transforms according to the irreducible representation of C_{3v} symmetry group.

highest (lowest) state of valence (conduction) band transforms according to A_1 irreducible representation. In Fig. 2.12(b), we show energy spectrum for the structure consisting of $N = 97$ atoms with $N_{deg} = 7$ degenerate zero-energy states. Here, zero-energy states characterize by different symmetries. There are two states transforming according to A_2 and E, and one transforming according to A_1 irreducible representation. Thus, it is clearly seen that the zero-energy degeneracy is not related to the symmetry of the system. Such degeneracy is called accidental. We note that for all studied structures a number of states with a given symmetry in the degenerate shell, N^{Γ}_{deg}, can be evaluate using following expressions, for $n-$ integer,

$N^{A_1}_{deg}$	$\text{int}\left(\frac{\text{N}_{\text{deg}}+2}{6}\right)$	$N_{deg} \neq 6n-1$
	$\text{int}\left(\frac{\text{N}_{\text{deg}}-4}{6}\right)$	$N_{deg} = 6n-1$
$N^{A_2}_{deg}$	$\text{int}\left(\frac{\text{N}_{\text{deg}}+5}{6}\right)$	$N_{deg} \neq 6n-4$
	$\text{int}\left(\frac{\text{N}_{\text{deg}}}{6}\right)$	$N_{deg} = 6n-4$
N^{E}_{deg}	$\text{int}\left(\frac{\text{N}_{\text{deg}}+1}{3}\right)$	$N_{deg} = 1, 2, ...$

Additionally, in energy spectra shown in Fig. 2.12(a) and (b), the highest (lowest) state of valence (conduction) band transforms according to A_1 and E irreducible representation, respectively. We note that for all studied structures the symmetry of these states confirms a following rule

$$\begin{array}{ccc} A_1 & \text{for} & N_{edge} = 3n-1 \\ E & \text{for} & \begin{array}{c} N_{edge} = 3n \\ N_{edge} = 3n-2 \end{array} \end{array}.$$

for $n-$ integer.

2.3 Triangular mesoscopic quantum rings with zigzag edges

The results, presented in this section, were published in a paper "Electronic and magnetic properties of triangular graphene quantum rings", by P. Potasz, A. D. Güçlü, O. Voznyy, J. A. Folk, and P. Hawrylak, Ref. [172].

We describe single particle properties of triangular graphene quantum rings (TGQR) with zigzag edges. TGQR can be fabricated using carbon nanotubes (CNT) as a mask in the etching process. One can place CNT over the graphene sheet along a given crystallographic direction and cover atoms lying below, e.g., along a zigzag direction. Three carbon nanotubes can be arranged in a triangular shape, along three zigzag edges, shown on the left in Fig. 2.13. As a result one expects to obtain a triangular structure with well defined zigzag edges and a hole in the center, as shown on the right in Fig. 2.13. The full TGQD consists of $N_{out}^2 + 4N_{out} + 1$ atoms, where $N_{out} = N_{edge}$. The small removed triangle consists of $N_{inn}^2 + 4N_{inn} + 1$ atoms, where N_{inn} is the number of edge atoms on one inner edge. The resulting TGQR has $N = N_{out}^2 - N_{inn}^2 + 4(N_{out} - N_{inn})$ atoms. Its width satisfies $N_{out} - N_{inn} = 3(N_{width} + 1)$, where N_{width} is the width counted in the number of benzene rings. The structure shown on the right of Fig. 2.13 has $N_{width} = 2$. We note that while outer edges are built of A-type of atoms, inner edges are built of B-type of atoms.

2.3.1 Energy spectrum

In the full triangle, the imbalance between the number of A type (N_A) and B type (N_B) of atoms in bipartite honeycomb graphene lattice, proportional to N_{edge}, leads to appearance of zero-energy states in the TB model in the nearest neighbors approximation. The number of zero-energy states is $N_{deg} = |N_A - N_B|$, according to subsection 2.2.2. Removing a small triangle from the center lowers the imbalance between two types of atoms in the structure, leading to a decreased number of zero-energy states. The degeneracy of the zero-energy shell in TGQRs can be defined as $N_{deg} = 3(N_{width} + 1)$. Thus, the number of zero-energy states in TGQR's only depends on the width of the ring, and not the size.

In Fig. 2.14, we show the single particle spectra for TGQRs obtained by diagonalizing TB Hamiltonian, Eq. (2.1). Figure 2.4.2(a) shows the energy

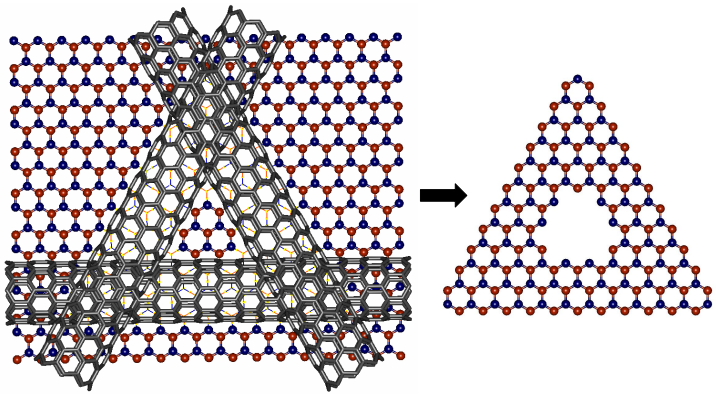

Figure 2.13: Proposed experimental method for designing TGQR. Three CNTs arranged in equilateral triangle along zigzag edges play the role of a mask. By using etching methods one can obtain TGQR with well defined edges. The circumference of CNT determines the width of TGQR. Red and blue colors distinguish between two sublattices in the honeycomb graphene lattice.

spectrum for TGQR with $N_{width} = 2$ consisting of $N = 171$ atoms and shown in Fig. 2.13. It has $N_{out} = 11$ and $N_{inn} = 2$ and the number of zero-energy states is $N_{deg} = 9$. Similarly, in Fig. 2.14(b) we show TB spectrum for TGQR with $N_{width} = 5$, and consisting of 504 atoms. It has $N_{out} = 21$ and $N_{inn} = 3$, giving $N_{deg} = 18$, consistent with our formula $N_{deg} = 3(N_{width} + 1)$. We note that the states of the zero-energy shell consist of orbitals belonging to one type of atoms indicated by red color in Fig. 2.13, which was proved in subsection 2.2.2, and lie mostly on the outer edge. On the other hand, the other states close to the Fermi level consist of orbitals belonging to both sublattices but lie mostly on inner edge (not shown here). This fact has implications for the magnetic properties of the system, described in the Section 4.2.

2.4 Hexagonal mesoscopic quantum rings

The results, presented in this section, were published in a paper "Spin and electronic correlations in gated graphene quantum rings", by P. Potasz, A. D. Güçlü, and P. Hawrylak, Ref. [173].

We consider hexagonal mesoscopic quantum rings. Below, a method of construction of hexagonal mesoscopic quantum rings is presented. The reason of using this method becomes clear in next subsection. We first consider six independent nanoribbons, then bring them together by turning on the hopping between the connecting atoms. In Fig. 2.15 we show two sets of six graphene

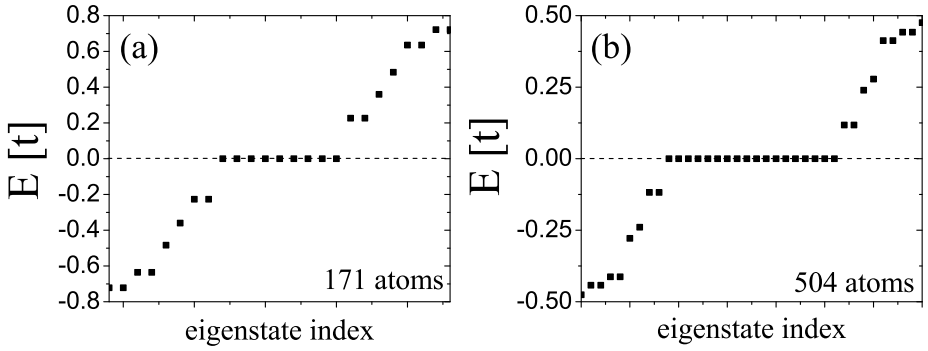

Figure 2.14: Single particle TB levels for TGQR with (a) $N_{width} = 2$, consisting of 171 atoms and (b) $N_{width} = 5$, consisting of 504 atoms. The degeneracy at the Fermi level (dashed line) is a function of the width $N_{deg} = 3(N_{width} + 1)$, for (a) $N_{deg} = 9$ and for (b) $N_{deg} = 18$.

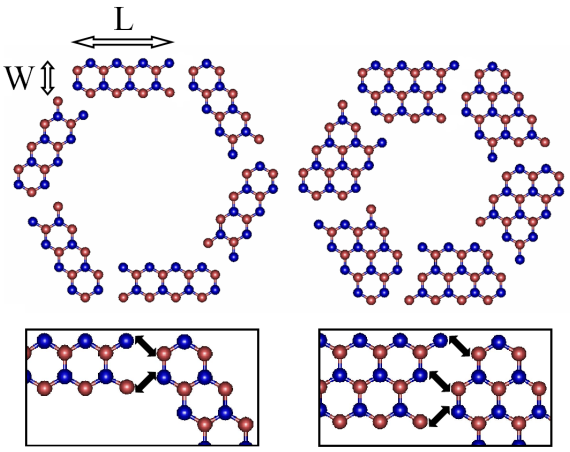

Figure 2.15: Construction of ring structures from six ribbon-like units. On the left, there are six thinnest possible ribbons (one benzene ring thick denoted as $W = 1$) arranged in a hexagonal ring structure. The length of each ribbon is given by $L = 4$, the number of one type of atoms in one row. Each ribbon consists of 16 atoms which gives a total of $N = 96$ atoms in a ring. On the right, there are six ribbons with width $W = 2$ (two benzene ring thick). Each of them consists of 21 atoms giving a total of $N = 126$ atoms in a ring. We create a thicker ring with a similar length $L = 4$ but a smaller antidot inside. Small black arrows in the bottom enlargement indicate bonds and hopping integrals between nearest neighbors in the TB model between neighboring ribbons.

ribbons arranged in a hexagonal ring. On the left side, thinnest possible ribbons with one benzene ring width are shown, denoted as $W = 1$. Each of them consists of 16 atoms. The length $L = 4$, is measured by the number of one type of atoms in the upper row, so the final ring is built of $N = 96$ atoms. Small black arrows in the bottom enlargement indicate bonds and hopping integrals between nearest neighbors in TB model between neighboring ribbons, two arrows in the case of thinnest structures. The number of such connecting atoms increases with increasing width as seen on the right hand side of Fig. 2.15. The thicker ribbon $W = 2$ has identical length to the one from the left side $L = 4$. In this case there are three connecting atoms. Three small black arrows in the bottom enlargement indicate three bonds. The final ring is built of $N = 126$ atoms. By connecting neighboring ribbons with different lengths and widths, we create rings with different single particle spectra.

2.4.1 Energy spectrum

In Fig. 2.16 we show the single particle energy levels near Fermi level obtained by diagonalizing TB Hamiltonian, Eq. (2.1), for rings with length $L = 8$ and different widths W. The thinnest ring $W = 1$ consists of $N = 192$ atoms. For this structure we observe nearly degenerate shells of energy levels separated by gaps. Each shell consists of six levels: two single and two doubly degenerate states. The first shell over the Fermi level is almost completely degenerate, while in the second one the degeneracy is slightly removed. We note that for rings with different lengths, the gap between the first and second shell is always larger then the gap at the Fermi level. With increasing width of the ring, the spectrum changes completely. For the rings with width $W = 2$ and $N = 270$ atoms, $W = 3$ and $N = 336$ atoms, and $W = 5$ and $N = 432$ atoms, shells are not visible. For $W = 4$ $N = 390$ atoms we observe appearance of shells separated by gaps further from Fermi level but the splitting between levels in these shells is much stronger in comparison to the thinnest ring. We note that for $W \geq 2$, although we do not observe a clear pattern of shells around the Fermi level, single shells of six levels separated by gaps from the rest of the spectrum appear far away from the Fermi energy in some cases.

In order to have a better understanding of the structure of the TB spectra, in Fig. 2.17, we show the evolution of single particle energies from six independent ribbons to a ring as the hopping t' between the ribbons is increased. To achieve this, we first diagonalize the TB Hamiltonian matrix for a single ribbon. We then take six such ribbons and create Hamiltonian matrix in the

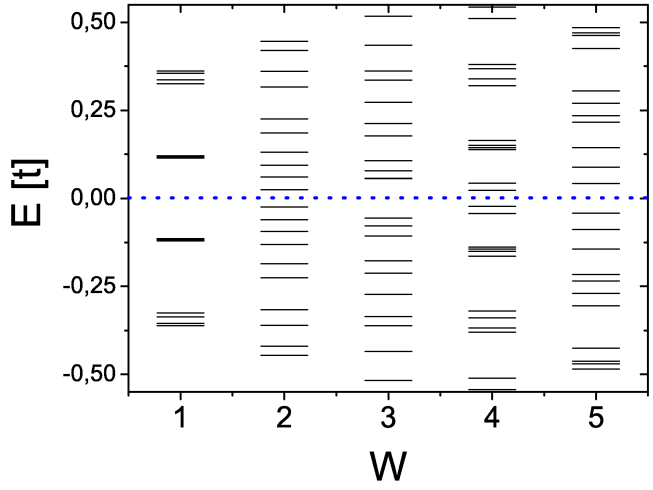

Figure 2.16: Single particle spectrum near Fermi level for ring structures with $L = 8$, different widths W and $t' = t$ (see Fig. 2.17). The shell structure is clearly observed only for the thinnest ring $W = 1$. Dotted blue line indicates the location of Fermi energy.

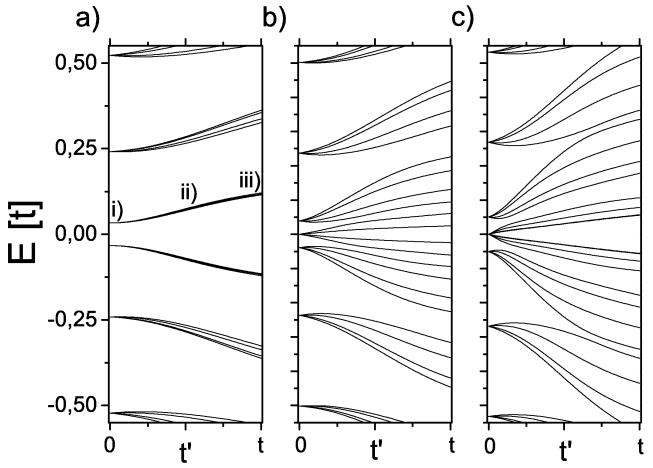

Figure 2.17: The evolution of the single particle spectrum from six independent ribbons with $L = 8$ to a hexagonal ring structure spectrum. t' indicate hopping integrals between neighboring ribbons. a) For the thinnest ring $W = 1$ six fold degeneracy is slightly removed, preserving a shell structure. For thicker structures ((b) and (c), $W = 2$ and $W = 3$ respectively) the six fold degeneracy is strongly lifted and shell structure is not observed.

basis of the eigenvectors of six ribbons. Here, the matrix has diagonal form. All energy levels are at least six fold degenerate. Next, using the six ribbons basis, we write hopping integrals corresponding to connecting atoms between neighboring ribbons indicated by small black arrows in Fig. 2.15. By slowly turning on the hopping integrals and diagonalizing the Hamiltonian at every step, we can observe the evolution of the spectrum from single particle states of six independent ribbons to a ring.

The hopping integrals between connecting atoms of neighboring ribbons are indicated by t' in Fig. 2.17. For the thinnest ring, Fig. 2.17(a), each ribbon consists of 32 atoms. There are only two connecting atoms between neighboring ribbons, giving only two hopping integrals t' between each two ribbons in the nearest neighbors approximation. We see that their influence is very small and six fold degenerate states evolve into shells with a very small splitting between levels. We note that this splitting is a bit stronger for higher energy levels but due to large gaps between consecutive levels of single ribbon the shell structure is still clearly observed. For the thicker structures, Fig. 2.17(b) and (c), the evolution of the spectrum has a more complicated behavior. For a given ring each ribbon consists of different number of two types of atoms giving rise to zero-energy edge-states [186]. With increasing width, the number of zero-energy states increases as well as the number of connecting atoms and equally the number of t' hopping integrals (see enlargement in Fig. 2.15). This causes a stronger splitting of levels for thicker rings in comparison to the thinnest one. Thus, the thicker ring's spectrum close to the Fermi level is due to the splitting of zero-energy states of independent ribbons. For $W = 2$ (one zero-energy state) and $W = 3$ (two zero-energy states), each ribbon consists of 45 and 56 atoms respectively, and the evolution of their spectrum is similar. The degeneracy is strongly lifted and no shell structure is observed.

In order to illuminate the influence of t' hopping integrals on the thinnest ring spectrum, in Fig. 2.18, we also show the electronic densities for the first shell over the Fermi level for three different values of t' (indicated in Fig. 2.18(a)). For $t' = 0$, there are six independent ribbons and first shell is perfectly six fold degenerate. The electronic charge density in each ribbon is larger on the two atoms with only one bond (see Fig.2.15) and gradually decreases along the length. For $t' = 0.5t$ the total energy of the shell increases and the degeneracy is slightly removed. Here, the highest peak of the electronic charge density is moved towards the center of each ribbon in comparison to $t' = 0$ case. Increasing t' to t causes increase of the total energy of the shell

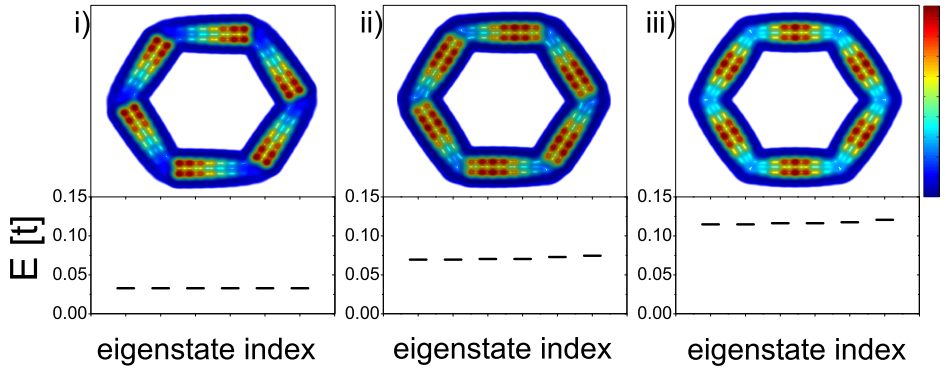

Figure 2.18: Energy levels and corresponding total electronic densities for the first six states over the Fermi level for the thinnest structure $W = 1$ with $L = 8$ and $N = 192$ atoms, for i) $t' = 0$, ii) $t' = 0.5t$, iii) $t' = t$. The three values of t' hopping integrals are indicated in Fig. 2.17(a).

and the highest peak of the electronic charge density is now perfectly in the middle of each arm of the ring. Thus, both the electronic charge density and the energy of levels change slightly during the gradual transition of ribbons into a hexagonal ring structure.

We find degenerate shells near the Fermi energy only for the thinnest rings $W = 1$. In Fig. 2.19 we show the low energy spectrum for two thinnest rings with different lengths. We clearly see shells with six levels. The splitting of levels of the first shell over the Fermi level is smaller for larger ring. For ring structure with $L = 4$ the difference between the highest and the lowest energy of levels forming the first shell is around $0.069t \simeq 0.17$ eV. In comparison, for ring with $L = 8$ this value is around $0.006t \simeq 0.015$ eV. Thus, we conclude that for smaller rings single particle energies can play important role in the properties of many particle states while for the larger rings interactions are expected to be more important.

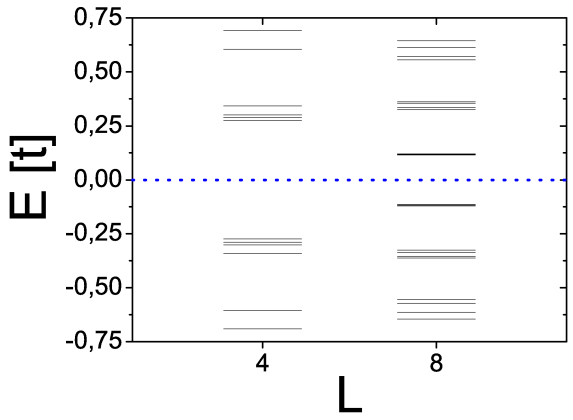

Figure 2.19: Single particle spectrum near Fermi level for the thinnest ring structures $W = 1$ with length $L = 8$ and $L = 4$. The shell structure is clearly observed. The splitting between levels in the first shell is smaller for larger structure. Dotted blue line indicate the location of the Fermi energy.

Chapter 3

Electron-electron interaction in gated graphene nanostructures

3.1 Introduction

A problem of interacting particles moving in graphene nanostructures is equivalent to interacting electrons moving in an external electrostatic potential. The confinement induces a discretization of the single particle energy levels. A common way of solving this task is, first, to find allowed single particle energies, fill obtained energy levels by electrons, and turn on interactions. An appropriate many-body Hamiltonian will be introduced in Sec. 3.2 with the two-body Coulomb part described in Sec. 3.3. The ground state of such system is determined by the competition between minimization of a kinetic energy or interactions between electrons. In the case of the large energy level spacing between single particle states, electrons occupy lowest single particle energy levels. An excitation of an electron to the unoccupied state, despite a possibility of decreasing of a Coulomb interaction, is still energetically expensive due to large cost of the kinetic energy. In such situation, the ground state of the system of N_{el} interacting electrons can be described approximately by using a many-body wave function constructed from single particle orbitals corresponding to N_{el} filled lowest energy levels. The wave function has to be antisymmetric with respect to exchange of two particle as a result of a fermionic nature of electrons. This antisymmetry requirements is satisfied by constructing a Slater determinant. The description of the system of interacting particles by using a single Slater determinant of effective Hartree-Fock orbitals corresponds to a mean-field approximation. It is described in Sec. 3.4.

When an energy spacing between single particle levels is comparable to the

characteristic Coulomb interaction energy, electron-electron interactions play an important role. In atoms, e.g. d-shell manganese (Mn, $4s^2$ $3d^5$), valence electrons occupy closely lying levels of the highest d-shell. Configurations of electrons with different spins can be formed. In this case a number of electrons, 5, is equal to the number of single particle levels and the total spin of the ground state is governed by Hunds rules-the configuration corresponding to electrons with parallel spins maximizes negative exchange interaction. More interesting situation occurs, when a number of electrons is different than a number of single particle levels. Electrons can fill energy levels in many different ways creating configurations with a similar total kinetic energy. As a consequence, electron-electron interactions can mix all these configurations forming a strongly correlated ground state, with incompressible liquids of the fractional quantum Hall effect as a good example [177, 178]. Solving a many-body Hamiltonian in a basis built of many possible configurations occupying single particle energy levels is called configuration interaction method. This method is characterized by large computational cost. The number of possible configurations exponentially increases with a number of electrons and energy levels. Even small systems containing e.g., 10 electrons occupying 20 energy levels corresponds to the dimension of Hilbert space around 10^5. Thus, one has to restrict its applicability to the small size systems. A more detail analysis of configuration interaction method will be presented in Section 3.5.

GQDs are systems consisting of few to few millions of atoms. In the case of single orbital TB model it corresponds to systems with a number of electrons well beyond the applicability of configuration interaction method. Alternative way of studying these systems is to combine mean-field and configuration interaction methods. Here, electrons from the filled band separated by the energy gap are described by a single Slater determinant of HF orbitals and the rest of electrons, in a degenerate shell, are treated in the exact diagonalization procedure. We describe this method in Section 3.6.

3.2 Many-body Hamiltonian

The Hamiltonian of interacting electrons in an effective potential V_{eff} can be written as

$$H_{MB} = \sum_i \left(\frac{-\nabla_i^2}{2} + \sum_j V_{eff}^j(\mathbf{r}_i - \mathbf{R}_j) \right) + \frac{1}{2} \sum_{i,j} \frac{1}{\kappa |\mathbf{r}_i - \mathbf{r}_j|}, \tag{3.1}$$

where $V_{eff}^{j}(\mathbf{r}-\mathbf{R}) = V^{A}(\mathbf{r}-\mathbf{R}) + V^{B}(\mathbf{r}-\mathbf{b}-\mathbf{R})$ are potentials from single particle Hamiltonian given by Eq. (1.1), and a second part is Coulomb interaction term written in atomic units (a.u.), 1 $a.u.$ = 27.211 eV, and κ is a dielectric constant. We can introduce field operators,

$$\begin{aligned}\Phi(\mathbf{r}) &= \sum_{j} c_j \phi_j(\mathbf{r}) \\ \Phi^{\dagger}(\mathbf{r}) &= \sum_{j} c_j^{\dagger} \phi_j^{*}(\mathbf{r}),\end{aligned} \tag{3.2}$$

where the fermionic operator $c_{i\sigma}$ ($c_{i\sigma}^{\dagger}$) annihilates (creates) an electron on i-th p_z orbital with spin σ. These operators satisfy anticommutation rules

$$\{c_{i\sigma}, c_{j\sigma}\} = \left\{c_{i\sigma}^{\dagger}, c_{j\sigma}^{\dagger}\right\} = 0; \quad \left\{c_{i\sigma'}, c_{j\sigma}^{\dagger}\right\} = \delta_{ij}\delta_{\sigma\sigma'}, \tag{3.3}$$

which guarantees the antisymmetry of a many-body state. Hamiltonian given by Eq. (3.1) in terms of field operators can be written as

$$\begin{aligned}H_{MB} &= \int d\mathbf{r}\Phi^{\dagger}(\mathbf{r})\left(\frac{-\nabla^2}{2} + \sum_{j} V_{eff}^{j}(\mathbf{r}-\mathbf{R}_j)\right)\Phi(\mathbf{r}) \\ &+ \frac{1}{2}\int\int d\mathbf{r}d\mathbf{r}'\Phi^{\dagger}(\mathbf{r})\Phi^{\dagger}(\mathbf{r}')\frac{1}{\kappa|\mathbf{r}-\mathbf{r}'|}\Phi(\mathbf{r}')\Phi(\mathbf{r}),\end{aligned} \tag{3.4}$$

Combining Eq. (3.4) and Eq. (3.2), Eq. (3.1) can be written in the second quantization form as

$$H = \sum_{i,\sigma}\epsilon_{i\sigma}c_{i\sigma}^{\dagger}c_{i\sigma} + \sum_{i,l,\sigma}\tau_{il\sigma}c_{i\sigma}^{\dagger}c_{l\sigma} + \frac{1}{2}\sum_{\substack{i,j,k,l,\\ \sigma\sigma'}}\langle ij|V|kl\rangle c_{i\sigma}^{\dagger}c_{j\sigma'}^{\dagger}c_{k\sigma'}c_{l\sigma}, \tag{3.5}$$

with $\tau_{il\sigma}$ defined by Eq. (1.5). $\langle ij|V|kl\rangle$ are Coulomb matrix elements described in detail in next subsection. The first term from Eq. (3.5) corresponds to a site energy of p_z orbitals which is a constant, $\epsilon_{i\sigma} = \epsilon$.

3.3 Two body scattering - Coulomb matrix elements

Two-body Coulomb term from Eq. 3.5 is written as

$$\frac{1}{2}\sum_{\substack{i,j,k,l,\\ \sigma\sigma'}}\langle ij|V|kl\rangle c_{i\sigma}^{\dagger}c_{j\sigma'}^{\dagger}c_{k\sigma'}c_{l\sigma}, \tag{3.6}$$

with Coulomb matrix elements defined as

$$\langle ij \mid V \mid kl\rangle = \int\int d\mathbf{r_1}d\mathbf{r_2}\phi_{i\sigma}^{*}(\mathbf{r_1})\phi_{j\sigma'}^{*}(\mathbf{r_2})\frac{1}{\epsilon \mid \mathbf{r_2}-\mathbf{r_1} \mid}\phi_{k\sigma'}(\mathbf{r_2})\phi_{l\sigma}(\mathbf{r_1}), \tag{3.7}$$

where $\mathbf{r_1}$ and $\mathbf{r_2}$ are coordinates of the first and the second electron, respectively, and σ_i is a spin of spin-orbital with spatial part ϕ_i. Above integral contains four p_z orbitals. Two electrons occupying orbitals on sites with indices k and l interact with each other and can scatter to two orbitals on sites with indices j and i. One can note here that for $i = l$ and $j = k$, one gets $\langle ij|V|ji\rangle$, and this term corresponds to the classical Coulomb interaction between two electronic densities localized on sites i and j, $|\phi_i(\mathbf{r_1})|^2$ and $|\phi_j(\mathbf{r_2})|^2$, respectively. On the other hand, for $i = k$ and $j = l$, $\langle ij|V|ij\rangle$ corresponds to the exchange term and does not vanish only when electrons on i and j orbitals have the same spin, $\sigma = \sigma'$. It is related to an orthogonality of spin part of wavefunctions in Eq. 3.7.

π_z orbitals of carbon atoms in matrix elements given by Eq. 3.7 can be approximated by Slater orbitals defined in Ref. [179]. They are given by a function

$$\phi_i(\mathbf{r_1}) = \left(\frac{\xi^5}{32\pi}\right)^{\frac{1}{2}} z \exp\left(\frac{-\xi r_1}{2}\right), \tag{3.8}$$

with $\xi = 3.14$ [179]. Coulomb matrix elements given by Eq. 3.7 were numerically calculated for orbitals localized on lattice sites of the honeycomb graphene lattice [144, 173]. In numerical calculations, on-site, scattering, and exchange terms up to the next-nearest neighbors, as well as all long-range direct terms were obtained. In Table 3.1 we show selected Coulomb matrix elements for dielectric constant $\kappa = 1$. Numbers 1, 2 and 3 indicate electron on-site, on nearest-neighbor site and on next-nearest-neighbor site of a hexagonal lattice, respectively.

3.4 Mean-Field HF approximation

We apply a mean-field approximation to Coulomb interaction term from Eq. (3.5). A following ansatz is used

$$\begin{aligned} & c^\dagger_{i\sigma} c^\dagger_{j\sigma'} c_{k\sigma'} c_{l\sigma} \simeq \\ = \; & c^\dagger_{i\sigma}\langle c_{j\sigma'} c^\dagger_{k\sigma'}\rangle c_{l\sigma} + \langle c^\dagger_{i\sigma} c_{l\sigma}\rangle c^\dagger_{j\sigma'} c_{k\sigma'} - c^\dagger_{i\sigma} c_{k\sigma'}\langle c^\dagger_{j\sigma'} c_{l\sigma}\rangle \delta_{\sigma\sigma'} - \langle c^\dagger_{i\sigma} c_{k\sigma'}\rangle c^\dagger_{j\sigma'} c_{l\sigma}\delta_{\sigma\sigma'}, \end{aligned}$$

where $\langle c^\dagger_{i\sigma} c_{l\sigma}\rangle$ is an average of two operators with respect to the ground state and will be defined later. First two terms correspond to the direct terms and last two terms to the exchange terms. The exchange terms vanish for distinguishable particles, e.g. particles with different spins. We can write a

$\langle ij \mid V \mid kl\rangle$	$E\ [eV]$
$\langle 11 \mid V \mid 11\rangle$	16.522
$\langle 12 \mid V \mid 21\rangle$	8.640
$\langle 13 \mid V \mid 31\rangle$	5.333
$\langle 11 \mid V \mid 12\rangle$	3.157
$\langle 12 \mid V \mid 31\rangle$	1.735
$\langle 12 \mid V \mid 12\rangle$	0.873
$\langle 11 \mid V \mid 22\rangle$	0.873
$\langle 22 \mid V \mid 13\rangle$	0.606

Table 3.1: Selected coulomb matrix elements between electrons on sites in graphene honeycomb lattice for $\kappa = 1$. Numbers 1, 2 and 3 indicate electron on-site, on nearest-neighbor site and on next-nearest-neighbor site of hexagonal lattice, respectively.

Coulomb operator from Eq. (3.5) in a mean-field approximation as

$$\begin{aligned} V_{MF} &= \frac{1}{2}\sum_{\substack{i,j,k,l,\\ \sigma\sigma'}} \langle ij|V|kl\rangle \left(\langle c_{j\sigma'}c^\dagger_{k\sigma'}\rangle c^\dagger_{i\sigma}c_{l\sigma} + \langle c^\dagger_{i\sigma}c_{l\sigma}\rangle c^\dagger_{j\sigma'}c_{k\sigma'}\right) \\ &- \frac{1}{2}\sum_{\substack{i,j,k,l,\\ \sigma\sigma'}} \langle ij|V|kl\rangle \left(\langle c^\dagger_{j\sigma'}c_{l\sigma}\rangle c^\dagger_{i\sigma}c_{k\sigma'}\delta_{\sigma\sigma'} + \langle c^\dagger_{i\sigma}c_{k\sigma'}\rangle c^\dagger_{j\sigma'}c_{l\sigma}\delta_{\sigma\sigma'}\right), \end{aligned} \tag{3.9}$$

where the first part corresponds to direct terms and the second part to exchange terms. Direct terms from Eq. (3.9) can be written as

$$\begin{aligned} &\frac{1}{2}\sum_{\substack{i,j,k,l,\\ \sigma\sigma'}} \langle ij|V|kl\rangle \left(\langle c_{j\sigma'}c^\dagger_{k\sigma'}\rangle c^\dagger_{i\sigma}c_{l\sigma} + \langle c^\dagger_{i\sigma}c_{l\sigma}\rangle c^\dagger_{j\sigma'}c_{k\sigma'}\right) \\ = \frac{1}{2}\sum_{\substack{i,j,k,l,\\ \sigma\sigma'}} &\langle ij|V|kl\rangle\langle c_{j\sigma'}c^\dagger_{k\sigma'}\rangle c^\dagger_{i\sigma}c_{l\sigma} + \frac{1}{2}\sum_{\substack{i,j,k,l,\\ \sigma\sigma'}} \langle ji|V|lk\rangle\langle c^\dagger_{j\sigma'}c_{k\sigma'}\rangle c^\dagger_{i\sigma}c_{l\sigma} \\ &= \sum_{\substack{i,j,k,l,\\ \sigma\sigma'}} \langle ij|V|kl\rangle\langle c_{j\sigma'}c^\dagger_{k\sigma'}\rangle c^\dagger_{i\sigma}c_{l\sigma}, \end{aligned}$$

where in the second term from the second line we have changed indices $i\sigma \leftrightarrow j\sigma'$, $l\sigma \leftrightarrow k\sigma'$ and used a fact $\langle ji|V|lk\rangle = \langle ij|V|kl\rangle$. In a similar way, one can transform exchange terms from Eq. (3.9) getting

$$\begin{aligned} &-\frac{1}{2}\sum_{\substack{i,j,k,l,\\ \sigma\sigma'}} \langle ij|V|kl\rangle \left(\langle c^\dagger_{j\sigma'}c_{l\sigma}\rangle c^\dagger_{i\sigma}c_{k\sigma'}\delta_{\sigma\sigma'} + \langle c^\dagger_{i\sigma}c_{k\sigma'}\rangle c^\dagger_{j\sigma'}c_{l\sigma}\delta_{\sigma\sigma'}\right) \\ &= -\sum_{\substack{i,j,k,l,\\ \sigma\sigma'}} \langle ij|V|lk\rangle\langle c^\dagger_{j\sigma'}c_{k\sigma'}\rangle c^\dagger_{i\sigma}c_{l\sigma}\delta_{\sigma\sigma'}, \end{aligned}$$

where in the first term a change $l\sigma \leftrightarrow k\sigma'$ and in the second term a change $i\sigma \leftrightarrow j\sigma'$ were performed. We used also fact $\langle ji|V|kl\rangle = \langle ij|V|lk\rangle$. Eq. (3.9) can be written as

$$V_{MF} = \sum_{\substack{i,j,k,l,\\ \sigma\sigma'}} \left(\langle ij|V|lk\rangle - \langle ij|V|lk\rangle\delta_{\sigma\sigma'}\right) \langle c^\dagger_{j\sigma'} c_{k\sigma'}\rangle c^\dagger_{i\sigma} c_{l\sigma}$$

Finally, Hamiltonian given by Eq. (3.5) can be written in a mean-field HF approximation as

$$\begin{aligned} H_{MF} &= \sum_{i,\sigma} \epsilon_{i\sigma} c^\dagger_{i\sigma} c_{i\sigma} + \sum_{i,l,\sigma} \tau_{il\sigma} c^\dagger_{i\sigma} c_{l\sigma} \\ &+ \sum_{\substack{i,j,k,l,\\ \sigma\sigma'}} \left(\langle ij|V|lk\rangle - \langle ij|V|lk\rangle\delta_{\sigma\sigma'}\right) \langle c^\dagger_{j\sigma'} c_{k\sigma'}\rangle c^\dagger_{i\sigma} c_{l\sigma} \end{aligned} \tag{3.10}$$

3.4.1 Hartree-Fock method - application to graphene nanostructures

In a previous section, a general form of a many-body Hamiltonian in a mean-field HF approximation, Eq. (3.10), without defining an average $\langle ...\rangle$ was written. We use this expression for particular systems - graphene and graphene nanostructures. Eq. (3.10) for graphene layer can be written as

$$\begin{aligned} H^o_{MF} &= \sum_{i,\sigma} \epsilon_{i\sigma} c^\dagger_{i\sigma} c_{i\sigma} + \sum_{i,l,\sigma} \tau_{il\sigma} c^\dagger_{i\sigma} c_{l\sigma} + \sum_{\substack{i,j,k,l,\\ \sigma\sigma'}} \left(\langle ij|V|lk\rangle - \langle ij|V|lk\rangle\delta_{\sigma\sigma'}\right) \rho^o_{jk\sigma'} \\ &= \sum_{i,l,\sigma} t_{il\sigma} c^\dagger_{i\sigma} c_{l\sigma}, \end{aligned} \tag{3.11}$$

with density matrix elements $\rho^o_{jk\sigma'} = \langle ...\rangle_{GS}$ calculated with respect to the ground state (GS)-the fully occupied valence band. This is effectively a one-body TB Hamiltonian given by Eq. 2.1 with experimentally measured hopping integral t_{il} for graphene [1]. The density matrix can be defined as

$$\rho^o_{jk\sigma'} = \sum_{\mathbf{k}} b^*_{\mathbf{R}_j}(\mathbf{k}) b_{\mathbf{R}_k}(\mathbf{k}), \tag{3.12}$$

where j and k are graphene lattice sites and a summation is over a full valence band. $b_{\mathbf{R}}$'s are the coefficients of the p_z orbitals and according to Eq. (1.11) can be written as

$$b_{\mathbf{R}_j} = \frac{1}{\sqrt{2N_c}} e^{i\mathbf{k}\mathbf{R}_j}, \tag{3.13}$$

for A-type atoms and

$$b_{\mathbf{R}_j} = \frac{1}{\sqrt{2N_c}} e^{i\mathbf{k}\mathbf{R_j}} e^{-i\theta_{\mathbf{k}}}, \tag{3.14}$$

for B-type atoms. Due to a translation invariance of the system, the density matrix depends only on a relative positions $|\mathbf{R_j} - \mathbf{R_k}|$. On-site density matrix elements for an arbitrary lattice site j are site and sublattice index independent,

$$\rho^o_{jj\sigma'} = \frac{1}{2N_c}\sum_{\mathbf{k}} e^{-i\mathbf{kR}} e^{i\mathbf{kR}} = \frac{1}{2N_c}\sum_{\mathbf{k}} 1 = \frac{1}{2}, \tag{3.15}$$

where we took into account the fact that the number of occupied states, is equal to the number of unit cells in the system [1]. The nearest neighbors density matrix elements for atoms from the same unit cell corresponds to $\mathbf{R_k} = \mathbf{R_j}$ and are calculated using

$$\begin{aligned} \rho^o_{jk\sigma'} &= \frac{1}{2N_c}\sum_{\mathbf{k}} e^{-i\mathbf{kR_j}} e^{i\mathbf{kR_k}} e^{-i\theta_\mathbf{k}} \\ &= \frac{1}{2N_c}\sum_{\mathbf{k}} e^{-i\theta_\mathbf{k}} \simeq 0.262, \end{aligned}$$

where the summation over occupied valence states is carried out numerically. We note that we obtain the same value for two other nearest neighbors. Same results can also be obtained by diagonalizing a sufficiently large graphene quantum dot, and by computing the density matrix elements for two nearest neighbors in the vicinity of the center of the structure. We have also calculated next-nearest neighbors density matrix elements, getting negligibly small value.

We would like to use Hamiltonian in a mean-field approximation for graphene nanostructures, but starting from single particle energy levels obtained within TB model. In order to do this, we combine Eq. (3.10) and Eq. (3.11) getting

$$\begin{aligned} H^{GQD}_{MF} &= H^{GQD}_{MF} - H^o_{MF} + H^o_{MF} \\ &= \sum_{i,\sigma} \epsilon_{i\sigma} c^\dagger_{i\sigma} c_{i\sigma} + \sum_{i,l,\sigma} t_{il\sigma} c^\dagger_{i\sigma} c_{l\sigma} \\ &+ \sum_{i,l,\sigma}\sum_{j,k,\sigma'} (\rho_{jk\sigma'} - \rho^o_{jk\sigma'})(\langle ij|V|kl\rangle - \langle ij|V|lk\rangle \delta_{\sigma,\sigma'}) c^\dagger_{i\sigma} c_{l\sigma}, \end{aligned} \tag{3.16}$$

where the subtracted component in a second term corresponds to mean-field interactions included in effective $t_{il\sigma}$ hopping integrals, described by graphene density matrix $\rho^o_{jk\sigma'}$. The density matrix elements $\rho_{jk\sigma'}$ are calculated with respect to the many-body ground state of graphene nanostructures. It can be written as

$$\rho_{jk} = \sum_{\mathbf{s}} A^{*s}_j A^s_k, \tag{3.17}$$

[1] The number of all energy levels is $2N_c$ (because of two atoms in a units cell), and only half of them is occupied, which gives N_c.

where indices s run over all occupied states and A_j^s are expansion coefficients of eigenstates written in a basis of localized p_z orbitals

$$c_s^\dagger = \sum_{i,\sigma} A_i^{*s} a_i^\dagger.$$

The Hamiltonian given by Eq. (3.16) has to be solved self-consistently to obtain Hartree-Fock quasi-particle orbitals.

3.4.2 Hubbard model - mean-field approximation

In order to derive a Hubbard model in a mean-field approximation, from all scattering matrix elements $\langle ij|V|kl\rangle$, only onsite terms $\langle ii|V|ii\rangle$, are kept. We note that Hubbard model is used to study quantum phase transitions in solid state physics [174–176]. Eq. (3.16) for a Hubbard model can be written as

$$\begin{aligned} H_{Hubb} &= \sum_{i,\sigma} \epsilon_{i\sigma} c_{i\sigma}^\dagger c_{i\sigma} + \sum_{i,l,\sigma} t_{il\sigma} c_{i\sigma}^\dagger c_{l\sigma} + U \sum_{i\sigma} \left(\langle \hat{n}_{i\sigma} \rangle - \frac{1}{2} \right) \hat{n}_{i\sigma'} \\ &= \sum_{i,\sigma} \epsilon_{i\sigma} c_{i\sigma}^\dagger c_{i\sigma} + \sum_{i,l,\sigma} t_{il\sigma} c_{i\sigma}^\dagger c_{l\sigma} \\ &+ U \sum_i \left(\langle \hat{n}_{i\uparrow} \rangle \hat{n}_{i\downarrow} + \langle \hat{n}_{i\downarrow} \rangle \hat{n}_{i\uparrow} - \frac{1}{2} \hat{n}_{i\downarrow} - \frac{1}{2} \hat{n}_{i\uparrow} \right), \end{aligned} \tag{3.18}$$

with a particle operator $\hat{n}_{i\sigma} = c_{i\sigma}^\dagger c_{i\sigma}$, $U = \langle ii|V|ii\rangle$, and we took into account fact that $\rho_{ii\sigma}^o = \frac{1}{2}$ according to Eq. (3.15). We choose the on-site interaction $U \sim 2.75$ eV according to Table 3.1 for the effective dielectric constant $\kappa = 6$ [180]. For a hopping integral between the nearest neighbors, $t = -2.5$ eV, the ratio $|U/t| = 1.1$ resides in commonly used range (1.1-1.3) [181] and is close to DFT results [101]. We note that the first term $\epsilon_{i\sigma}$ and last two terms from Eq. 3.18, $-\frac{1}{2}\hat{n}_{i\downarrow}$ and $-\frac{1}{2}\hat{n}_{i\uparrow}$ correspond to diagonal matrix elements and are equal for all sites i. Thus, they just shift an entire spectrum by a constant value and can be neglected. We can finally write the Hubbard model in the mean-field approximation as

$$H = t \sum_{\langle i,j\rangle,\sigma} c_{i\sigma}^\dagger c_{j\sigma} + U \sum_i \left(n_{i\uparrow} \langle n_{i\downarrow} \rangle + n_{i\downarrow} \langle n_{i\uparrow} \rangle \right), \tag{3.19}$$

where the first term is TB Hamiltonian in the nearest neighbor approximation, Eq. 2.1. A mean-field value of a particle operator can be explicitly written, e.g., for spin down, as

$$\langle \hat{n}_{i\downarrow} \rangle = \sum_s |A_{s\downarrow}^i|^2, \tag{3.20}$$

where index s run over all occupied states. Eq. (3.20) corresponds to the average spin down density on site i. Hubbard Hamiltonian given by Eq. (3.19) has to be solved in a self-consistent procedure. A solution is characterized by a single-particle spectrum and the spin density $M_i = (n_{i\uparrow} - n_{i\downarrow})/2$ on each atomic site i. A self-consistent procedure can be described in a following way. Hamiltonian given by Eq. (3.19) consists of two blocks, for spin up and spin down states. Additionally, spin up Hamiltonian depends on spin down densities and vice versa. As a starting point, one can choose a simple TB Hamiltonian given by Eq. (2.1). After diagonalizing it, eigenvalues and eigenvectors are given. Obtained energy levels are filled by N_{dn} and N_{up} electrons, occupying N_{dn} and N_{up} lowest eigenstates, respectively. Next, by using Eq. (3.20), for each site, spin up and spin down densities can be calculated. According to Eq. (3.19), calculated spin down densities correspond to diagonal matrix elements of spin up Hamiltonian and calculated spin up densities correspond to diagonal matrix elements of spin down Hamiltonian. After diagonalizing separately spin down and spin up Hamiltonians, new energy levels for spin down and spin up electrons are obtained. These new states are again filled by N_{dn} and N_{up} electrons which occupy N_{dn} and N_{up} lowest energy levels, respectively. New spin densities can be calculated and used in new spin up and spin down Hamiltonians. A procedure is repeated till a convergence with an appropriate accuracy is obtained.

3.5 Configuration interaction method

We start from writing a many-body Hamiltonian of interacting electrons occupying energy levels as

$$\begin{aligned} H_{MB} &= \sum_{s,\sigma} E_{s\sigma} a^{\dagger}_{s\sigma} a_{s\sigma} \\ &+ \frac{1}{2} \sum_{\substack{s,p,d,f,\\ \sigma,\sigma'}} \langle sp \mid V \mid df \rangle a^{\dagger}_{s\sigma} a^{\dagger}_{p\sigma'} a_{d\sigma'} a_{f\sigma}. \end{aligned} \tag{3.21}$$

The first term, energies $E_{s\sigma}$ correspond to eigenvalues of TB Hamiltonian given by Eq. (3.11). The second term from Hamiltonian given by Eq. (3.21) describes an interaction between quasi-particles occupying energy levels denoted by s, p, d, f indices. The two-body quasi-particle scattering matrix elements $\langle sp \mid V \mid df \rangle$ are calculated from the two-body localized on-site Coulomb matrix elements $\langle ij \mid V \mid kl \rangle$. Because Hamiltonian given by Eq. (3.21) does not contain any spin interaction terms, total spin S and its projection onto

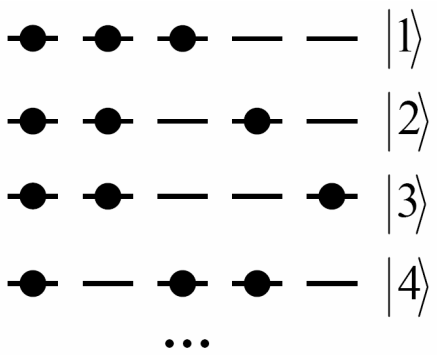

Figure 3.1: A scheme of possible distributions of spinless $N_{el} = 3$ particles within $N_{st} = 5$ energy states. Black bars corresponds to energy levels and black circuits to electrons. One can construct the total of $N_{conf} = 10$ distinct configurations. They form a many-body basis in the configuration interaction method.

z axis, S_z, are good quantum numbers. Hamiltonian matrix can be divided into blocks corresponding to different S or S_z. Each block can be diagonalized independently. In next subsection, we show a method of a construction of a many-body basis for a given S_z for electrons occupying single particle orbitals.

3.5.1 Creation of many-body basis

For a given number of electrons we write a many-body vector consisting of electrons distributed within single particle orbitals. It can be written as

$$|\Psi_1\rangle = \prod_{s\sigma} a^\dagger_{s\sigma}|0\rangle,$$

where $|0\rangle$ is a vacuum state in the case of TB energy levels. The number of operators in this product is equal to the number of electrons N_{el}. We show a method of construction a complete set of basis vectors on an example of $N_{el} = 3$ particles distributed within $N_{st} = 5$ states, for simplicity neglecting spin degrees of freedom. It is schematically presented in Fig. 3.1. Black bars corresponds to energy levels and black circuits to electrons. The first configuration from Fig. 3.1 can be written as

$$|1\rangle = a^\dagger_1 a^\dagger_2 a^\dagger_3|0\rangle,$$

where numbers $1, 2..$ label energy levels counted from the left to the right. We note that in order to avoid double counting of the same configuration one has to choose some convention of ordering creation operators in the many-body

vectors. Our choice is that we always write $...a_i^\dagger a_j^\dagger...|0>$ for $i < j$. We can calculate a total number of possible configurations N_{conf} by using binomial coefficient

$$N_{conf} = \left(\begin{array}{c} N_{st} \\ N_{el} \end{array} \right).$$

Thus, one can construct N_{conf} linear independent vectors which span our Hilbert space. For the case from Fig. 3.1, $N_{st} = 5$ and $N_{el} = 3$, we get $N_{conf} = 10$.

We include spin degrees of freedom. A many-body vector is a product of vectors for spin down and spin up configurations

$$|\Psi_1\rangle = \prod_s a_{s\downarrow}^\dagger |0\rangle \otimes \prod_p a_{p\uparrow}^\dagger |0\rangle = ...a_{s\downarrow}^\dagger ...a_{p\uparrow}^\dagger ...|0\rangle, \tag{3.22}$$

with the number of creation operators in this product equal to the number of electrons $N_{el} = N_{dn} + N_{up}$, and N_{dn} (N_{up}) defined as a number of electrons with spin down (spin up). The total number of configurations is

$$N_{conf} = N_{conf}^{dn} \cdot N_{conf}^{up},$$

where N_{conf}^{dn} (N_{conf}^{up}) is the number of configurations of electrons with spin down (spin up). We introduce an operator corresponding to a projection of total spin S onto z-axis. It is defined as

$$\hat{S}_z = \sum_s \sigma a_{s\sigma}^\dagger a_{s\sigma}.$$

This operator commutes with Hamiltonian given by Eq. (3.21), $[\hat{H}, \hat{S}_z] = 0$. Additionally, many-body vectors given by Eq. (3.22) are eigenvectors of this operator: each of them has a well defined projection of spin onto z-axis, $S_z = 1/2(N_{up} - N_{dn})$. For a given number of particles, N_{el}, sets of vectors for each S_z are constructed. These vectors span independent subspaces and a Hamiltonian matrix can be written in a block diagonal form, e.g. for even number of particles

$$\hat{H} = \left(\begin{array}{ccc} \left(\begin{array}{c} \\ S_z = 0 \\ \\ \end{array} \right) & & \\ & \left(\begin{array}{c} \\ S_z = 1 \\ \\ \end{array} \right) & \\ & & ... \end{array} \right).$$

One can also construct a Hamiltonian matrix in a block diagonal form for $\hat{S}^2$ operator, due to the fact that $[\hat{H}, \hat{S}^2] = 0$. This operator is defined as

$$\hat{S}^2 = \frac{N_{el}}{2} + \hat{S}_z^2 - \sum_{sp} a_{s\uparrow}^\dagger a_{p\downarrow}^\dagger a_{p\downarrow} a_{s\uparrow}.$$

The problem is that eigenvectors of $\hat{S}^2$ operator are linear combinations of eigenvectors of $\hat{S}_z$ operator. A finding of these eigenvectors requires some additional transformations, thus it is not so simple as in the case of $\hat{S}_z$ operator [182].

3.5.2 Construction of Hamiltonian matrix

In a many-body Hamiltonian given by Eq. (3.21) there are two operators. We can write this Hamiltonian as

$$H_{MB} = \hat{T} + \hat{V} \tag{3.23}$$

with a single particle operator

$$\hat{T} = \sum_{s,\sigma} E_{s\sigma} a_{s\sigma}^\dagger a_{s\sigma} \tag{3.24}$$

and a two body operator

$$\hat{V} = \frac{1}{2} \sum_{\substack{s,p,d,f,\\ \sigma,\sigma'}} \langle sp \mid V \mid df \rangle a_{s\sigma}^\dagger a_{p\sigma'}^\dagger a_{d\sigma'} a_{f\sigma}. \tag{3.25}$$

We show a method of finding matrix elements of these operators in a given many-body basis. We choose a system with 4 particles, e.g. two spin down and two spin up electrons distributed within 3 single particle states for each spin. It corresponds to the subspace with $S_z = 0$. One can create a total of $N_{conf} = 3 * 3 = 9$ configurations. They have a following form

$$\begin{array}{ll} |\Psi_1\rangle = a_{1\downarrow}^\dagger a_{2\downarrow}^\dagger a_{1\uparrow}^\dagger a_{2\uparrow}^\dagger |0\rangle, & |\Psi_6\rangle = a_{1\downarrow}^\dagger a_{3\downarrow}^\dagger a_{2\uparrow}^\dagger a_{3\uparrow}^\dagger |0\rangle, \\ |\Psi_2\rangle = a_{1\downarrow}^\dagger a_{2\downarrow}^\dagger a_{1\uparrow}^\dagger a_{3\uparrow}^\dagger |0\rangle, & |\Psi_7\rangle = a_{2\downarrow}^\dagger a_{3\downarrow}^\dagger a_{1\uparrow}^\dagger a_{2\uparrow}^\dagger |0\rangle, \\ |\Psi_3\rangle = a_{1\downarrow}^\dagger a_{2\downarrow}^\dagger a_{2\uparrow}^\dagger a_{3\uparrow}^\dagger |0\rangle, & |\Psi_8\rangle = a_{2\downarrow}^\dagger a_{3\downarrow}^\dagger a_{1\uparrow}^\dagger a_{3\uparrow}^\dagger |0\rangle, \\ |\Psi_4\rangle = a_{1\downarrow}^\dagger a_{3\downarrow}^\dagger a_{1\uparrow}^\dagger a_{2\uparrow}^\dagger |0\rangle, & |\Psi_9\rangle = a_{2\downarrow}^\dagger a_{3\downarrow}^\dagger a_{2\uparrow}^\dagger a_{3\uparrow}^\dagger |0\rangle. \\ |\Psi_5\rangle = a_{1\downarrow}^\dagger a_{3\downarrow}^\dagger a_{1\uparrow}^\dagger a_{3\uparrow}^\dagger |0\rangle, & \end{array} \tag{3.26}$$

We keep a convention that from the left to right we have creation operators with increasing indices, first for spin down, and next for spin up operators.

Single particle operator

From configurations given by Eq. 3.26, we take one vector for our example, e.g., $|\Psi_8\rangle$. We act on this vector by a single particle operator given by Eq. (3.24),

$$\hat{T}|\Psi_8\rangle = \sum_{s,\sigma} E_{s\sigma} a^\dagger_{s\sigma} a_{s\sigma} a^\dagger_{2\downarrow} a^\dagger_{3\downarrow} a^\dagger_{1\uparrow} a^\dagger_{3\uparrow} |0\rangle. \tag{3.27}$$

The summation run over all possible energy levels, $s = 1, 2, 3$, $\sigma = \downarrow, \uparrow$. Lets choose first $s\sigma = 1\downarrow$. We get

$$\begin{aligned} E_{1\downarrow} a^\dagger_{1\downarrow} a_{1\downarrow} a^\dagger_{2\downarrow} a^\dagger_{3\downarrow} a^\dagger_{1\uparrow} a^\dagger_{3\uparrow} |0\rangle &= -E_{1\downarrow} a^\dagger_{1\downarrow} a^\dagger_{2\downarrow} a_{1\downarrow} a^\dagger_{3\downarrow} a^\dagger_{1\uparrow} a^\dagger_{3\uparrow} |0\rangle = E_{1\downarrow} a^\dagger_{1\downarrow} a^\dagger_{2\downarrow} a^\dagger_{3\downarrow} a_{1\downarrow} a^\dagger_{1\uparrow} a^\dagger_{3\uparrow} |0\rangle \\ &= -E_{1\downarrow} a^\dagger_{1\downarrow} a^\dagger_{2\downarrow} a^\dagger_{3\downarrow} a^\dagger_{1\uparrow} a_{1\downarrow} a^\dagger_{3\uparrow} |0\rangle = E_{1\downarrow} a^\dagger_{1\downarrow} a^\dagger_{2\downarrow} a^\dagger_{3\downarrow} a^\dagger_{1\uparrow} a^\dagger_{3\uparrow} a_{1\downarrow} |0\rangle = 0, \end{aligned}$$

where in order to change the order of operators anticommutation relations given by Eq. (3.3) were used. From this example one can see that the nonzero terms appear only when annihilation operator from an operator matches to one of creation operators in a vector. This can be seen by looking at e.g. $s\sigma = 3\downarrow$ element,

$$\begin{aligned} E_{3\downarrow} a^\dagger_{3\downarrow} a_{3\downarrow} a^\dagger_{2\downarrow} a^\dagger_{3\downarrow} a^\dagger_{1\uparrow} a^\dagger_{3\uparrow} |0\rangle &= -E_{3\downarrow} a^\dagger_{3\downarrow} a^\dagger_{2\downarrow} a_{3\downarrow} a^\dagger_{3\downarrow} a^\dagger_{1\uparrow} a^\dagger_{3\uparrow} |0\rangle \\ &= -E_{3\downarrow} a^\dagger_{3\downarrow} a^\dagger_{2\downarrow} \left(1 - a^\dagger_{3\downarrow} a_{3\downarrow}\right) a^\dagger_{1\uparrow} a^\dagger_{3\uparrow} |0\rangle \\ = -E_{3\downarrow} a^\dagger_{3\downarrow} a^\dagger_{2\downarrow} a^\dagger_{1\uparrow} a^\dagger_{3\uparrow} |0\rangle &- E_{3\downarrow} a^\dagger_{3\downarrow} a^\dagger_{2\downarrow} a^\dagger_{3\downarrow} a_{3\downarrow} a^\dagger_{1\uparrow} a^\dagger_{3\uparrow} |0\rangle \\ &= -E_{3\downarrow} a^\dagger_{3\downarrow} a^\dagger_{2\downarrow} a^\dagger_{1\uparrow} a^\dagger_{3\uparrow} |0\rangle = E_{3\downarrow} a^\dagger_{2\downarrow} a^\dagger_{3\downarrow} a^\dagger_{1\uparrow} a^\dagger_{3\uparrow} |0\rangle, \end{aligned}$$

where in the last line we have changed the order of operators to obtain a vector written in agreement with our convention. It is clearly seen that we get the same vector $|\Psi_8\rangle$ as we started. We can write all nonzero terms for single particle operator acting on this vector as

$$\hat{T}|\Psi_8\rangle = \left(E_{2\downarrow} + E_{3\downarrow} + E_{1\uparrow} + E_{3\uparrow}\right)|\Psi_8\rangle.$$

One can see that these energies correspond to occupied states by electrons in this configuration. Basis vectors are orthonormalized, $\langle\Psi_i|\Psi_j\rangle = \delta_{ij}$, thus nonzero matrix elements after projecting only on bra vector $\langle\Psi_8|$ are obtained. Finally, it can be written as

$$\langle\Psi_8|\hat{T}|\Psi_8\rangle = E_{2\downarrow} + E_{3\downarrow} + E_{1\uparrow} + E_{3\uparrow},$$

which corresponds to diagonal terms. In this way, one can find nonzero matrix elements for all configurations given by Eq. 3.26 for single particle operator.

Two body operator

We present a method of finding nonzero matrix elements for Coulomb operator given by Eq. (3.25). Before we do this, we write this operator in a more suitable form. It can be written as

$$\hat{V} = \frac{1}{2} \sum_{s,p,d,f} \langle sp \mid V \mid df \rangle a_s^\dagger a_p^\dagger a_d a_f, \tag{3.28}$$

where we did not write a spin dependence apparently remembering that $s \equiv s\sigma$, $p \equiv p\sigma'$, $d \equiv d\sigma'$, $f \equiv f\sigma$. We divide a summation into two parts, for $d < f$ and $d > f$. A term $d = f$ can be neglected because it gives $d\sigma' = f\sigma$, a term in Eq. (3.28) with two identical annihilation operators. If one acted with it on an arbitrary state, one would get always zero, which is a consequence of Pauli principle: no more than one electron can occupy a state with given quantum numbers. Eq. (3.28) is written as

$$\begin{aligned}
\hat{V} &= \frac{1}{2} \sum_{s,p,d<f} \langle sp \mid V \mid df \rangle a_s^\dagger a_p^\dagger a_d a_f + \frac{1}{2} \sum_{s,p,d>f} \langle sp \mid V \mid df \rangle a_s^\dagger a_p^\dagger a_d a_f \\
&= \frac{1}{2} \sum_{s,p,d<f} \langle sp \mid V \mid df \rangle a_s^\dagger a_p^\dagger a_d a_f - \frac{1}{2} \sum_{s,p,d>f} \langle sp \mid V \mid df \rangle a_s^\dagger a_p^\dagger a_f a_d \\
&= \frac{1}{2} \sum_{s,p,d<f} \langle sp \mid V \mid df \rangle a_s^\dagger a_p^\dagger a_d a_f - \frac{1}{2} \sum_{s,p,d<f} \langle sp \mid V \mid fd \rangle a_s^\dagger a_p^\dagger a_d a_f \\
&= \frac{1}{2} \sum_{s,p,d<f} \left(\langle sp \mid V \mid df \rangle - \langle sp \mid V \mid fd \rangle \right) a_s^\dagger a_p^\dagger a_d a_f,
\end{aligned}$$

where going from the first to the second line we used anticommutation rules given by Eq. (3.3), and in the second term in the third line we have changed indices $d \leftrightarrow f$. In a similar way, one can divide a summation over s and p into $s < p$ and $s > p$, and finally write two body Coulomb operator as

$$\hat{V} = \sum_{s>p,d<f} \left(\langle sp \mid V \mid df \rangle - \langle sp \mid V \mid fd \rangle \right) a_s^\dagger a_p^\dagger a_d a_f. \tag{3.29}$$

Writing explicitly a spin dependence, we can distinguish six possibilities of terms in a summation in Eq. (3.29)

$$\begin{array}{lll}
1^o & s\downarrow p\downarrow d\downarrow f\downarrow & \langle sp \mid V \mid df \rangle - \langle sp \mid V \mid fd \rangle \\
2^o & s\uparrow p\uparrow d\uparrow f\uparrow & \langle sp \mid V \mid df \rangle - \langle sp \mid V \mid fd \rangle \\
3^o & s\uparrow p\downarrow d\downarrow f\uparrow & \langle sp \mid V \mid df \rangle \\
4^o & s\uparrow p\downarrow d\uparrow f\downarrow & -\langle sp \mid V \mid fd \rangle \\
5^o & s\downarrow p\uparrow d\uparrow f\downarrow & \langle sp \mid V \mid df \rangle \\
6^o & s\downarrow p\uparrow d\downarrow f\uparrow & -\langle sp \mid V \mid fd \rangle.
\end{array} \tag{3.30}$$

These six possibilities can be related to the arrangement of creation operators in a many-body vector $...a^{\dagger}_{s\downarrow}...a^{\dagger}_{p\uparrow}...|0\rangle$. Here, $s\sigma < p\sigma'$ for arbitrary s and p. We show that in order to satisfy a condition $s\sigma > p\sigma'$ and $d\sigma' < f\sigma$ only first three terms survive. For example, the fourth term contains $d\uparrow$ and $f\downarrow$. In this particular case $d\uparrow< f\downarrow$ but it is forbidden because in our convention spin up operators are always for larger indices than spin down operators, $d\uparrow> f\downarrow$. Thus, we can write Eq. (3.29) as

$$\hat{V} = \sum_{s>p,d<f} \left(\langle sp \mid V \mid df\rangle - \langle sp \mid V \mid fd\rangle\right) a^{\dagger}_s a^{\dagger}_p a_d a_f = \hat{H}_{\downarrow\downarrow} + \hat{H}_{\uparrow\uparrow} + \hat{H}_{\downarrow\uparrow},$$

where

$$\hat{H}_{\downarrow\downarrow} = \sum_{s>p,d<f} \left(\langle sp \mid V \mid df\rangle - \langle sp \mid V \mid fd\rangle\right) a^{\dagger}_{s\downarrow} a^{\dagger}_{p\downarrow} a_{d\downarrow} a_{f\downarrow} \tag{3.31}$$

$$\hat{H}_{\uparrow\uparrow} = \sum_{s>p,d<f} \left(\langle sp \mid V \mid df\rangle - \langle sp \mid V \mid fd\rangle\right) a^{\dagger}_{s\uparrow} a^{\dagger}_{p\uparrow} a_{d\uparrow} a_{f\uparrow} \tag{3.32}$$

$$\hat{H}_{\downarrow\uparrow} = \sum_{s,p,d,f} \langle sp \mid V \mid df\rangle a^{\dagger}_{s\uparrow} a^{\dagger}_{p\downarrow} a_{d\downarrow} a_{f\uparrow}. \tag{3.33}$$

We note that in a last term conditions $s\uparrow> p\downarrow$ and $d\downarrow> f\uparrow$ are automatically satisfied for arbitrary s and p or d and f. Thus, we have separated a Coulomb term given by Eq. (3.25) into components describing scattering of two particles within a given spin subspace, Eq. (3.31) and (3.32), and a component describing scattering of one particle within spin up and one within spin up subspace, Eq. (3.33).

We show an effect of acting by these operators on our example vector. In order to simplify a description we will not write matrix elements, which can be easily added from Eq. (3.31-3.33). An operator $\hat{H}_{\downarrow\downarrow}$ act on a vector $|\Psi_8\rangle$ which is written as

$$\hat{H}_{\downarrow\downarrow}|\Psi_8\rangle \rightarrow \sum_{s>p,d<f} a^{\dagger}_{s\downarrow} a^{\dagger}_{p\downarrow} a_{d\downarrow} a_{f\downarrow} a^{\dagger}_{2\downarrow} a^{\dagger}_{3\downarrow} a^{\dagger}_{1\uparrow} a^{\dagger}_{3\uparrow} |0\rangle. \tag{3.34}$$

There are two spin down annihilation operators and two spin down creation operators. Creation operators with spin up don't play a role here. The only choice to obtain nonvanishing terms is to take annihilation operators from Hamiltonian identical to creation operators from a vector. In other case, we can move annihilation operator to the right by using anticommutation relations and act it on a vacuum, getting zero. Thus, we can have only $d = 2\downarrow$ and $f = 3\downarrow$, due to a condition $d < f$. We can write (3.34) as

$$\hat{H}_{\downarrow\downarrow}|\Psi_8\rangle \rightarrow \sum_{s>p} a^{\dagger}_{s\downarrow} a^{\dagger}_{p\downarrow} a_{2\downarrow} a_{3\downarrow} a^{\dagger}_{2\downarrow} a^{\dagger}_{3\downarrow} a^{\dagger}_{1\uparrow} a^{\dagger}_{3\uparrow} |0\rangle. \tag{3.35}$$

By using anticommutation relations given by Eq. (3.3), Eq. (3.35) is reduced to

$$\hat{H}_{\downarrow\downarrow}|\Psi_8\rangle \rightarrow -\sum_{s>p} a^\dagger_{s\downarrow}a^\dagger_{p\downarrow}a^\dagger_{1\uparrow}a^\dagger_{3\uparrow}|0\rangle. \tag{3.36}$$

We can write above term for all s in a summation as

$$\begin{aligned}\hat{H}_{\downarrow\downarrow}|\Psi_8\rangle \rightarrow & -a^\dagger_{2\downarrow}a^\dagger_{1\downarrow}a^\dagger_{1\uparrow}a^\dagger_{3\uparrow}|0\rangle - a^\dagger_{3\downarrow}a^\dagger_{1\downarrow}a^\dagger_{1\uparrow}a^\dagger_{3\uparrow}|0\rangle - a^\dagger_{3\downarrow}a^\dagger_{2\downarrow}a^\dagger_{1\uparrow}a^\dagger_{3\uparrow}|0\rangle \\ & = a^\dagger_{1\downarrow}a^\dagger_{2\downarrow}a^\dagger_{1\uparrow}a^\dagger_{3\uparrow}|0\rangle + a^\dagger_{1\downarrow}a^\dagger_{3\downarrow}a^\dagger_{1\uparrow}a^\dagger_{3\uparrow}|0\rangle + a^\dagger_{2\downarrow}a^\dagger_{3\downarrow}a^\dagger_{1\uparrow}a^\dagger_{3\uparrow}|0\rangle, \end{aligned} \tag{3.37}$$

where in the second line the order of operators was changed to obtain vectors in agreement with our convention. These new three vectors corresponds to some configuration vectors from our basis, given by (3.26). They can be found by comparing all creation operators in these vectors, one by one with all creation operators in vectors from our basis. This is a very inefficient method and in Section 3.5.3 a more effective way will be shown. We write all nonzero matrix elements corresponding to these vectors

$$\begin{aligned}\langle\Psi_2|\hat{H}_{\downarrow\downarrow}|\Psi_8\rangle &= \langle 21 \mid V \mid 23\rangle - \langle 21 \mid V \mid 32\rangle \\ \langle\Psi_5|\hat{H}_{\downarrow\downarrow}|\Psi_8\rangle &= \langle 31 \mid V \mid 23\rangle - \langle 31 \mid V \mid 32\rangle \\ \langle\Psi_8|\hat{H}_{\downarrow\downarrow}|\Psi_8\rangle &= \langle 32 \mid V \mid 23\rangle - \langle 32 \mid V \mid 32\rangle, \end{aligned}$$

with a help of Eq. 3.31.

In a similar way, we can find nonzero matrix elements of an operator $\hat{H}_{\uparrow\uparrow}$ given by Eq. (3.32). We focus on an operator $\hat{H}_{\downarrow\uparrow}$, Eq. (3.33). We write

$$\hat{H}_{\downarrow\uparrow}|\Psi_8\rangle = \sum_{s,p,d,f} \langle sp \mid V \mid df\rangle a^\dagger_{s\uparrow}a^\dagger_{p\downarrow}a_{d\downarrow}a_{f\uparrow}a^\dagger_{2\downarrow}a^\dagger_{3\downarrow}a^\dagger_{1\uparrow}a^\dagger_{3\uparrow}|0\rangle. \tag{3.38}$$

There are two annihilation operators, one for spin down state and one for spin up. Based on previous results, we know that these operators must match with creation operators in a configuration vector. These operators can correspond to states $d = 2, 3$ for spin down and $f = 1, 3$ for spin up. From them, four combinations can be created

$$\begin{aligned} d\uparrow{=}\,2\uparrow \quad f\uparrow{=}\,1\uparrow \\ d\uparrow{=}\,2\uparrow \quad f\uparrow{=}\,3\uparrow \\ d\uparrow{=}\,3\uparrow \quad f\uparrow{=}\,1\uparrow \\ d\uparrow{=}\,3\uparrow \quad f\uparrow{=}\,3\uparrow \end{aligned} \tag{3.39}$$

We take the first combination, $d\uparrow{=}\,2\uparrow, f\uparrow{=}\,1\uparrow$. From Eq. (3.38) one gets

$$\begin{aligned} & \sum_{s,p} a^\dagger_{s\uparrow}a^\dagger_{p\downarrow}a_{2\downarrow}a_{1\uparrow}a^\dagger_{2\downarrow}a^\dagger_{3\downarrow}a^\dagger_{1\uparrow}a^\dagger_{3\uparrow}|0\rangle \\ = & \sum_{s,p} a^\dagger_{s\uparrow}a^\dagger_{p\downarrow}a_{2\downarrow}a^\dagger_{2\downarrow}a^\dagger_{3\downarrow}a_{1\uparrow}a^\dagger_{1\uparrow}a^\dagger_{3\uparrow}|0\rangle = \sum_{s,p} a^\dagger_{s\uparrow}a^\dagger_{p\downarrow}a^\dagger_{3\downarrow}a^\dagger_{3\uparrow}|0\rangle. \end{aligned}$$

The summation over s and p run over all possible states but s and p indices have to be different than indices in present creation operators. In the case, when one has two creation operators corresponding to the same state, due to a Hermicity of Coulomb operator, one can act with them as annihilation operators on bra vector, getting zero. This is also a consequence of Pauli principle: it is not possible to create two particles on a state with given quantum numbers. We write all elements in a summation

$$\begin{aligned}\sum_{s,p} a^\dagger_{s\uparrow}a^\dagger_{p\downarrow}a^\dagger_{3\downarrow}a^\dagger_{3\uparrow}|0\rangle &= a^\dagger_{1\uparrow}a^\dagger_{1\downarrow}a^\dagger_{3\downarrow}a^\dagger_{3\uparrow}|0\rangle + a^\dagger_{1\uparrow}a^\dagger_{2\downarrow}a^\dagger_{3\downarrow}a^\dagger_{3\uparrow}|0\rangle \\ &+ a^\dagger_{2\uparrow}a^\dagger_{1\downarrow}a^\dagger_{3\downarrow}a^\dagger_{3\uparrow}|0\rangle + a^\dagger_{2\uparrow}a^\dagger_{2\downarrow}a^\dagger_{3\downarrow}a^\dagger_{3\uparrow}|0\rangle\end{aligned}$$

Again, to write vectors in our convention a change of order of operator is required. We get

$$\begin{aligned}\sum_{s,p} a^\dagger_{s\uparrow}a^\dagger_{p\downarrow}a^\dagger_{3\downarrow}a^\dagger_{3\uparrow}|0\rangle &= a^\dagger_{1\downarrow}a^\dagger_{3\downarrow}a^\dagger_{1\uparrow}a^\dagger_{3\uparrow}|0\rangle + a^\dagger_{2\downarrow}a^\dagger_{3\downarrow}a^\dagger_{1\uparrow}a^\dagger_{3\uparrow}|0\rangle \\ &+ a^\dagger_{1\downarrow}a^\dagger_{3\downarrow}a^\dagger_{2\uparrow}a^\dagger_{3\uparrow}|0\rangle + a^\dagger_{2\downarrow}a^\dagger_{3\downarrow}a^\dagger_{2\uparrow}a^\dagger_{3\uparrow}|0\rangle\end{aligned}$$

In analogy to the case of operator $\hat{H}_{\downarrow\downarrow}$, these four new vectors give nonvanishing terms only when projected onto identical configuration vectors, given by (3.26). We write matrix elements for an operation (3.38) for $d\uparrow = 2\uparrow, f\uparrow = 1\uparrow$

$$\begin{aligned}\langle\Psi_5|\hat{H}_{\downarrow\uparrow}|\Psi_8\rangle &= \langle 11 \mid V \mid 33\rangle \\ \langle\Psi_8|\hat{H}_{\downarrow\uparrow}|\Psi_8\rangle &= \langle 12 \mid V \mid 33\rangle \\ \langle\Psi_6|\hat{H}_{\downarrow\uparrow}|\Psi_8\rangle &= \langle 21 \mid V \mid 33\rangle \\ \langle\Psi_9|\hat{H}_{\downarrow\uparrow}|\Psi_8\rangle &= \langle 22 \mid V \mid 33\rangle.\end{aligned}$$

From each of four combinations given by (3.39), one gets four nonzero matrix elements, getting a total of 16 nonzero matrix elements. We will not write them here.

3.5.3 Diagonalization methods for large matrices

In configuration interaction method, a size of the Hilbert space exponentially increases with a number of particles and a number of states. For example, for a system with $N_{st} = 10$ and $N_{el} = 5$ one gets

$$N_{conf} = \left(\begin{array}{c} 10 \\ 5 \end{array}\right) = \frac{10!}{(10-5)!5!} = 126 \simeq 10^2$$

but if one doubles the number of states and particles

$$N_{conf} = \left(\begin{array}{c} 20 \\ 10 \end{array}\right) = \frac{20!}{(20-10)!10!} = 184756 \simeq 10^5,$$

which is three orders of magnitude larger. Thus, this method has to be restricted to calculations of small systems or an efficient way of calculation methods is required.

For large matrices, $N_{conf} > 10^5$, problems of storing matrix elements due to a large memory space requirement appear. Additionally, a procedure of diagonalization of matrix by regular methods using linear algebra packages, e.g. Lapack subroutines, is not possible. The important fact is that only few lowest eigenvalues are important from physical point of view. These ones correspond to the ground state and low energy excited states. In order to find these eigenvalues, iterative methods are required. In this Section, we present an iterative method to find extremal eigenvalues of large matrices, Lanczos method [183]. There is an important advantage of using this method. It is based on a matrix-vector multiplication and in each consecutive iteration only a product of this operation is required. The efficient way to overcome problems with storing matrix elements is to calculate them "on the fly", separately for each iteration. Calculated matrix elements are multiplied by a appropriate coefficients of a given vector and only a product of this operation, a vector, is stored. Thus, instead of storing N_{conf}^2 matrix elements, one can only store N_{conf} coefficients of a new vector. There are several ways of implementing Lanczos method. We now present one of it.

Lanczos method [183]

Solving a Schrodinger equation is equivalent to a rotation of a matrix to its diagonal form. It can be written as

$$U^{-1}\begin{pmatrix} H_{11} & H_{12} & H_{13} & ... \\ H_{21} & H_{22} & H_{23} & ... \\ H_{31} & H_{32} & H_{33} & ... \\ ... & ... & ... & \ddots \end{pmatrix} U = \begin{pmatrix} E_1 & 0 & 0 & ... \\ 0 & E_2 & 0 & ... \\ 0 & 0 & E_3 & ... \\ ... & ... & ... & \ddots \end{pmatrix},$$

where U is a unitary matrix consisting of column eigenvectors $\mathbf{v}_i$ of matrix H, $U = (\mathbf{v}_1, \mathbf{v}_2, ..., \mathbf{v}_n)$, and E_i are eigenvalues of matrix H. Instead of rotating matrix H to a diagonal form, one can rotate it to tridiagonal form

$$W^{-1}\begin{pmatrix} H_{11} & H_{12} & H_{13} & ... \\ H_{21} & H_{22} & H_{23} & ... \\ H_{31} & H_{32} & H_{33} & ... \\ ... & ... & ... & \ddots \end{pmatrix} W = \begin{pmatrix} \alpha_1 & \beta_1 & 0 & ... \\ \beta_1 & \alpha_2 & \beta_2 & ... \\ 0 & \beta_2 & \alpha_3 & ... \\ ... & ... & ... & \ddots \end{pmatrix}, \qquad (3.40)$$

where W is a unitary matrix consisting of column vectors $\mathbf{w}_i$, $W = (\mathbf{w}_1, \mathbf{w}_2, ..., \mathbf{w}_n)$. By multiplying Eq. (3.40) by matrix W on the left one

gets

$$\begin{pmatrix} H_{11} & H_{12} & H_{13} & ... \\ H_{21} & H_{22} & H_{23} & ... \\ H_{31} & H_{32} & H_{33} & ... \\ ... & ... & ... & \ddots \end{pmatrix} W = W \begin{pmatrix} \alpha_1 & \beta_1 & 0 & ... \\ \beta_1 & \alpha_2 & \beta_2 & ... \\ 0 & \beta_2 & \alpha_3 & ... \\ ... & ... & ... & \ddots \end{pmatrix}, \tag{3.41}$$

which can be written as

$$\begin{pmatrix} H_{11} & H_{12} & H_{13} & ... \\ H_{21} & H_{22} & H_{23} & ... \\ H_{31} & H_{32} & H_{33} & ... \\ ... & ... & ... & \ddots \end{pmatrix} (\mathbf{w}_1, \mathbf{w}_2, ...) = (\mathbf{w}_1, \mathbf{w}_2, ...) \begin{pmatrix} \alpha_1 & \beta_1 & 0 & ... \\ \beta_1 & \alpha_2 & \beta_2 & ... \\ 0 & \beta_2 & \alpha_3 & ... \\ ... & ... & ... & \ddots \end{pmatrix} \tag{3.42}$$

By comparing two sides of Eq. (3.42), we can obtain a set of equations

$$\begin{aligned} H\mathbf{w}_1 &= \mathbf{w}_1\alpha_1 + \mathbf{w}_2\beta_1 \\ H\mathbf{w}_2 &= \mathbf{w}_1\beta_1 + \mathbf{w}_2\alpha_2 + \mathbf{w}_3\beta_2 \\ H\mathbf{w}_3 &= \mathbf{w}_2\beta_2 + \mathbf{w}_3\alpha_3 + \mathbf{w}_4\beta_3 \\ &... \\ H\mathbf{w}_k &= \mathbf{w}_{k-1}\beta_{k-1} + \mathbf{w}_k\alpha_k + \mathbf{w}_{k+1}\beta_k. \end{aligned} \tag{3.43}$$

We solve these equations iteratively, starting from randomly generated vector $\mathbf{w}_1$. In the first equation from a set of Eq. (3.43) unknown quantities are α_1, β_1, $\mathbf{w}_2$. Projecting this equation on $\mathbf{w}_1$ direction one gets

$$\mathbf{w}_1^T H \mathbf{w}_1 = \alpha_1, \tag{3.44}$$

due to an orthogonality requirement, $\mathbf{w}_i^T \mathbf{w}_j = \delta_{ij}$. Thus α_1 is just an expectation value of a matrix H in a direction $\mathbf{w}_1$. Knowing α_1, we can write

$$H\mathbf{w}_1 - \alpha_1\mathbf{w}_1 = \beta_1\mathbf{w}_2. \tag{3.45}$$

An above equation corresponds to an orthogonalization procedure. Labeling $\mathbf{z}_2 = H\mathbf{w}_1$ and using a definition of α_1, Eq. (3.44), Eq. (3.45) can be written as

$$\mathbf{z}_2 - (\mathbf{w}_1^T \mathbf{z}_2)\mathbf{w}_1 = \beta_1\mathbf{w}_2, \tag{3.46}$$

where we can see that from vector $\mathbf{z}_2$ a component in a $\mathbf{w}_1$ direction is subtracted. This is a simple Gramm-Schmidt orthogonalization procedure. We write Eq. (3.45) as

$$\mathbf{r} = \beta_1\mathbf{w}_2 \tag{3.47}$$

with

$$\mathbf{r} = H\mathbf{w}_1 - \alpha_1\mathbf{w}_1. \tag{3.48}$$

A new vector $\mathbf{w}_2$ is just an unnormalized vector $\mathbf{r}$

$$\mathbf{w}_2 = \frac{\mathbf{r}}{||\mathbf{r}||},$$

with a norm

$$\beta_1 = ||\mathbf{r}|| = ||H\mathbf{w}_1 - \alpha_1\mathbf{w}_1||.$$

We can go to the second equation of a set of Eq. (3.43). Here, unknown are α_2, β_2, $\mathbf{w}_3$. Projecting this equation on $\mathbf{w}_2$ direction one gets

$$\mathbf{w}_2^T H\mathbf{w}_2 = \alpha_2, \tag{3.49}$$

so α_2 is an expectation value of matrix H in a direction $\mathbf{w}_2$. We can write the second equation of a set of Eq. (3.43) as

$$\mathbf{r} = \mathbf{w}_3\beta_2$$

with

$$\mathbf{r} = H\mathbf{w}_2 - \mathbf{w}_1\beta_1 - \mathbf{w}_2\alpha_2. \tag{3.50}$$

This equation also is an orthogonalization procedure. Labeling $\mathbf{z}_3 = H\mathbf{w}_2$ and using a definition of α_2, Eq. (3.49), and β_1 from Eq. (3.47) after projecting on $\mathbf{w}_2$, Eq. (3.50) can be written as

$$\mathbf{z}_3 - (\mathbf{w}_1^T\mathbf{z}_3)\mathbf{w}_1 - (\mathbf{w}_2^T\mathbf{z}_3)\mathbf{w}_2 = \beta_2\mathbf{w}_3. \tag{3.51}$$

Similarly to previous step,

$$\beta_2 = ||\mathbf{r}|| = ||H\mathbf{w}_2 - \mathbf{w}_1\beta_1 - \mathbf{w}_2\alpha_2||$$

and

$$\mathbf{w}_3 = \frac{\mathbf{r}}{||\mathbf{r}||}.$$

In the third and next equations from a set of Eq. (3.43), the same steps as for the second equation is adopted. We shortly write entire procedure in few

steps

0.	$k = 1,$ random $\mathbf{w}_\mathrm{k}$	generation of a vector
1.	$\mathbf{w}_k = \mathbf{w}_k / \|\|\mathbf{w}_k\|\|$	normalization
2.	$H\mathbf{w}_k = \mathbf{w}_{k+1}$	
3.	$\alpha_k = \mathbf{w}_k^T H \mathbf{w}_k$	finding α_1
4.	$\mathbf{w}_{k+1} = \mathbf{w}_{k+1} - (\mathbf{w}_k^T \mathbf{w}_{k+1})\mathbf{w}_k$	orthogonalization
5.	$\beta_k = \|\|\mathbf{w}_{k+1}\|\|$	finding β_1
6.	$\mathbf{w}_{k+1} = \mathbf{w}_{k+1} / \|\|\mathbf{w}_{k+1}\|\|$	normalization
7.	$H\mathbf{w}_{k+1} = \mathbf{w}_{k+2}$	
8.	$\alpha_{k+1} = \mathbf{w}_{k+1}^T H \mathbf{w}_{k+1}$	finding $\alpha_{\mathrm{k+1}}$
9.	$\mathbf{w}_{k+2} = \mathbf{w}_{k+2} - (\mathbf{w}_k^T \mathbf{w}_{k+2})\mathbf{w}_k - (\mathbf{w}_{k+1}^T \mathbf{w}_{k+2})\mathbf{w}_{k+1}$	orthogonalization
10.	$\beta_{k+1} = \|\|\mathbf{w}_{k+2}\|\|$	finding $\beta_{\mathrm{k+1}}$
11.	$\mathbf{w}_{k+2} = \mathbf{w}_{k+2} / \|\|\mathbf{w}_{k+2}\|\|$	normalization
12.	$k = k + 1$	
13.	go to 7	

In practice, in a step nr 9 an orthogonalization to all previous vectors is performed, which eliminates numerical errors. These lead to so called "Ghost states", which artificially increases a degeneracy of eigenvalues.

Methods of optimization of calculations

Finding matrix elements of a matrix with N_{conf} size require N_{conf}^2 operations. There are several ways to speed up this process. The important note is only nonzero matrix elements are needed. In the Hamiltonian given by Eq. (3.21), there are two terms, a single particle operator (3.24) and a two particle operator (3.25). By acting them on an arbitrary basis vector, only one particle changes its state for an operator (3.24), or two particles change their states for an operator (3.25). From this, we conclude that all matrix elements between vectors which differ by more than two operators are zeros. These findings are called Slater rules. Including them significantly improves the time of calculations because of neglecting many zero matrix elements. However, in our method it is not possible to implement this idea. In our case, we first find values of nonzero matrix elements and next find a position of them in a matrix. The procedure is as following.

With each configuration, two binary numbers can be associated, one for spin down and one for spin up operators. When a configuration vector contains a creation operator corresponding to a given state we put "1", in other case "0". Lets take our example vector, $|\Psi_8\rangle$ from vectors (3.26). It can be written

as a binary number as

$$|\Psi_8\rangle = a^\dagger_{2\downarrow}a^\dagger_{3\downarrow}a^\dagger_{1\uparrow}a^\dagger_{3\uparrow}|0\rangle = |011|101\rangle, \tag{3.52}$$

where 1's correspond to occupied states and 0's to empty states. We don't have a particle in the first spin down states and in the second spin up state, which are written as 0's in binary numbers. The length of binary number is equal to the number of states in a system. These binary numbers can be written in a decimal system

$$|011\rangle = 2^1 + 2^0 = 3 \tag{3.53}$$

for spin down and

$$|101\rangle = 2^2 + 2^0 = 5 \tag{3.54}$$

for spin up, where powers of '2' are counted from right to left starting from power '0'. In this way, one can associate binary numbers with all configuration vectors (3.26)

Ψ_i	spin down	spin up
$\|\Psi_1\rangle = a^\dagger_{1\downarrow}a^\dagger_{2\downarrow}a^\dagger_{1\uparrow}a^\dagger_{2\uparrow}\|0\rangle = \|110\|110\rangle$	6	6
$\|\Psi_2\rangle = a^\dagger_{1\downarrow}a^\dagger_{2\downarrow}a^\dagger_{1\uparrow}a^\dagger_{3\uparrow}\|0\rangle = \|110\|101\rangle$	6	5
$\|\Psi_3\rangle = a^\dagger_{1\downarrow}a^\dagger_{2\downarrow}a^\dagger_{2\uparrow}a^\dagger_{3\uparrow}\|0\rangle = \|110\|011\rangle$	6	3
$\|\Psi_4\rangle = a^\dagger_{1\downarrow}a^\dagger_{3\downarrow}a^\dagger_{1\uparrow}a^\dagger_{2\uparrow}\|0\rangle = \|101\|110\rangle$	5	6
$\|\Psi_5\rangle = a^\dagger_{1\downarrow}a^\dagger_{3\downarrow}a^\dagger_{1\uparrow}a^\dagger_{3\uparrow}\|0\rangle = \|101\|101\rangle$	5	5
$\|\Psi_6\rangle = a^\dagger_{1\downarrow}a^\dagger_{3\downarrow}a^\dagger_{2\uparrow}a^\dagger_{3\uparrow}\|0\rangle = \|101\|011\rangle$	5	3
$\|\Psi_7\rangle = a^\dagger_{2\downarrow}a^\dagger_{3\downarrow}a^\dagger_{1\uparrow}a^\dagger_{2\uparrow}\|0\rangle = \|011\|110\rangle$	3	6
$\|\Psi_8\rangle = a^\dagger_{2\downarrow}a^\dagger_{3\downarrow}a^\dagger_{1\uparrow}a^\dagger_{3\uparrow}\|0\rangle = \|011\|101\rangle$	3	5
$\|\Psi_9\rangle = a^\dagger_{2\downarrow}a^\dagger_{3\downarrow}a^\dagger_{2\uparrow}a^\dagger_{3\uparrow}\|0\rangle = \|011\|011\rangle$	3	3.

(3.55)

It is seen that these vectors are arranged in a suitable way. First, all vectors with the same spin down part are written, with spin up part arranged according to binary numbers in descending order. Next, for lower spin down binary number, the same order of spin up binary numbers is kept.

We show an effect of acting on these vectors by Hamiltonian operator given by Eq. (3.21). After acting by single particle operator, Eq. (3.24), the same vector is returned, thus we will not consider this case here. Lets take first two body operator given by Eq. (3.31). According to Eq. (3.37), we get new three vectors

Ψ_i	spin down	spin up
$a^\dagger_{1\downarrow}a^\dagger_{2\downarrow}a^\dagger_{1\uparrow}a^\dagger_{3\uparrow}\|0\rangle = \|110\|101\rangle$	6	5
$a^\dagger_{1\downarrow}a^\dagger_{3\downarrow}a^\dagger_{1\uparrow}a^\dagger_{3\uparrow}\|0\rangle = \|101\|101\rangle$	5	5
$a^\dagger_{2\downarrow}a^\dagger_{3\downarrow}a^\dagger_{1\uparrow}a^\dagger_{3\uparrow}\|0\rangle = \|011\|101\rangle$	3	5,

(3.56)

where corresponding binary numbers were also written. We acted only on spin down part, so spin up part remains unchanged. The idea is to find efficiently ordering numbers i corresponding to these vectors. In Subsection 3.4.2 we compared all creation operators of these vectors with basis vectors (3.26) one by one. Now, we just have to compare corresponding binary numbers of vectors (3.56) to basis vectors (3.55). Additionally, we don't have to do this one by one. All binary numbers are ordered and we can use bisection method. The efficiency of bisection method is $\sim \ln N_{conf}$, instead of $\sim N_{conf}$ in a regular comparison.

The idea of the bisection method is following. The set of binary numbers in descending order is given. Each binary number bin in a set corresponds to some integer index i, which can be labeled as $bin(i)$. The largest i is noted as i_{max}, the smallest i_{min}. We try to find an index j of a binary number $bin(j)$ corresponding to our new vector. A set $bin(i)$ is divided into two equal subsets, $\langle bin(i_{min}), bin(k)\rangle$ and $(bin(k), bin(i_{max})\rangle$, for $k = (i_{max} + i_{min})/2$. Next step is to check whether one of equalities $bin(j) = bin(i_{min})$, $bin(j) = bin(i_{max})$ or $bin(j) = bin(k)$ is satisfied. If yes, we can stop because index j is found. If not, we choose a subset which contains $bin(j)$ and divide it into new two subsets. For example, if $bin(j)$ is in the second subset, new subsets are defined as $\langle bin(k), bin((k + i_{max})/2)\rangle$ and $(bin((k + i_{max})/2), bin(i_{max})\rangle$. If an equality $bin(j) = bin((k + i_{max})/2)$ is satisfied, we can stop because index j is found. If not, a check which subset contains $bin(j)$ is required. A procedure of a division of sets into two subsets is repeated till an equality is satisfied. We can write this procedure in few steps

0. read bin(i), define $\mathrm{i_{min}}$, $\mathrm{i_{max}}$
1. if bin(j) = bin($\mathrm{i_{min}}$) stop
   if bin(j) = bin($\mathrm{i_{max}}$) stop
2. $k = (i_{max} + i_{min})/2$
3. if bin(j) = bin(k) stop
4. if bin(j) $\leq$ bin(k) then $\mathrm{i_{max}} = \mathrm{k}$
   if bin(j) $>$ bin(k) then $\mathrm{i_{min}} = \mathrm{k}$
5. go to 1

In the case of operator given by Eq. (3.33), we act on both, spin down and spin up parts changing a position of one particle for each of it. A procedure of calculations is equivalent, independently for spin down and spin up subspaces. A final vector is a product of new spin down and spin up vectors.

We would like to emphasize an importance of a division of a Coulomb

part of the many-body Hamiltonian, Eq. (3.25), into three terms, Eq. (3.31), Eq. (3.32) and Eq. (3.33). A bisection method for Eq. (3.25) requires $\sim N_{conf} \ln N_{conf}$ operations for all s, p, d, f indices which run over all $\sim N_{st}$ states for $\downarrow$ and $\uparrow$ states giving the number of operations

$$N_{op} \sim 2^2 (N_{st})^4 N_{conf} \ln N_{conf},$$

when '2^2' comes from a summation over spins (σ and σ'). In our case, a bisection method for terms (3.31) and (3.32) run only over $N^{\downarrow}_{conf}$ ($N^{\uparrow}_{conf}$) configurations where $N^{\downarrow}_{conf} \sim \sqrt{N_{conf}}$ which gives $\sim 2\sqrt{N_{conf}} \ln \sqrt{N_{conf}} = \sqrt{N_{conf}} \ln N_{conf}$ operations. The total number of operations is reduced to

$$N_{op} \sim (N_{st})^4 N_{conf} \ln N_{conf} + (N_{st})^4 \sqrt{N_{conf}} \ln N_{conf},$$

where the first part corresponds to term (3.33) and the second part to terms (3.31) and (3.32). The second part is negligibly small comparing to the first one. Thus, a division of a Coulomb part of a many-body Hamiltonian, Eq. (3.25), into three terms, Eq. (3.31), Eq. (3.32) and Eq. (3.33) approximately four times reduces the time of calculations.

In our numerical programs, all spin down and spin up configurations with corresponding binary numbers are stored. It is possible even for, e.g. $N^{\downarrow}_{el} = 15$ distributed within $N^{\downarrow}_{st} = 30$, giving $N^{\downarrow}_{conf} \simeq 10^8$ configurations. Each of our spin configurations consists of 15 integer numbers. In order to store them, it requires $\sim$ 1Gb of memory, which is not too much even for personal computers. In this case, approximately a total of $N_{conf} \simeq N^{\downarrow}_{conf} * N^{\uparrow}_{conf} \simeq 10^{16}$ configurations is obtained. It is not presently possible to diagonalize so large matrix, so we are within an available calculation range.

3.6 TB+HF+CI method

We would like to study the role of interaction effects in graphene nanostructures. Solving the full many-body problem even for structures with tens of atoms is not possible at present. Thus, we combine the mean-field HF approach with exact CI diagonalization method. We are interested in systems with the degenerate shell, where electron-electron interactions play an important role. Thus, we explain our methodology based on TGQD consisting of $N = 97$ atoms with $N_{deg} = 7$ degenerate states. The procedure is schematically shown in Fig. 3.2. In Fig. 3.2(a) it is clearly seen that the valence band and the degenerate shell are separated by the energy gap. Thus, the closed

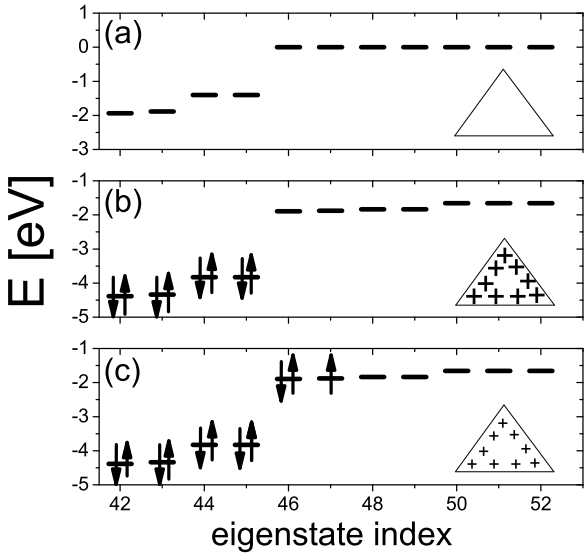

Figure 3.2: (a) Single-particle nearest-neighbor TB energy levels. The zero-energy shell on the Fermi level is perfectly degenerate. (b) Positively charged system with an empty degenerate band after self-consistent Hartee-Fock (HF) mean-field calculations described by a single Slater determinant (TB+HF model). (c) Occupation of empty degenerate HF quasi-orbitals by electrons. The inset pictures schematically show the excess charge corresponding to each of the three model systems. The ground state and the total spin of the system of interacting electrons can be calculated by using the configuration interaction (CI) method. The charge neutrality corresponds to a half-filled degenerate band (not shown).

shell system of $N_{ref} = N - N_{deg}$ interacting electrons is expected to be well described in a mean-field approximation, using a single Slater determinant. This corresponds to a charged system with N_{deg} positive charges, as schematically shown in Fig. 3.2(b). The Hamiltonian given by Eq. (3.16) is self-consistently solved for N_{ref} electrons. Obtained new orbitals for quasi-particles correspond to a fully occupied valence band and completely empty degenerate states. One can note that because of the mean-field interaction with the valence electrons, a group of three states is now separated from the rest by a small gap of $\sim$0.2 eV, Fig. 3.2(b). The three states correspond to HF quasiparticles localized in the three corners of the triangle [144]. As will be shown in Sec. 4.1.3, this is related to the long-range interaction. We start filling degenerate energy levels by adding extra electrons one by one, schematically shown in Fig. 3.2(c). Next, we solve the many-body Hamiltonian corresponding to the added electrons, given by Eq. (3.21). In our calculations, we neglect scattering from/to the states from a fully occupied valence band. Moreover, because of the large energy gap between the degenerate states and the conduction band, we can neglect scatterings to the higher energy states. Our assumptions can be confirmed by comparing the energy gaps and Coulomb interaction matrix elements. For example, the system with degenerate states separated by energy gaps $\Delta E \sim 0.5$ eV has the intra degenerate states interaction terms $V \sim 0.23$ eV. The Coulomb matrix elements V scattering electrons from an arbitrary degenerate state to the valence band and/or to the conduction band are $V \sim 0.2$ eV. Hence, the effect of these scatterings is proportional to $V^2/\Delta E \ll 1$, and is weak. Thus, many body properties of electrons occupying the degenerate states are primarily governed by interactions between electrons within these states. These approximations allow us to treat the degenerate shell as an independent system which significantly reduces the dimension of the Hilbert space. The basis is constructed from vectors corresponding to all possible many-body configurations of electrons distributed within the degenerate states. For a given number of electrons, N_{el}, Hamiltonian given by Eq. (3.21) is diagonalized in each subspaces with a given S_z.

Chapter 4

Magnetic properties of gated graphene nanostructures

4.1 Triangular graphene quantum dots with zigzag edges

The results, presented in Sections 4.1.1-4.1.3, were published in a paper "Electronic properties of gated triangular graphene quantum dots: Magnetism, correlations, and geometrical effects", by P. Potasz, A. D. Güçlü, A. Wójs, and P. Hawrylak, Ref. [165].

4.1.1 Analysis as a function of filling factor

In Fig. 4.1, we analyze the dependence of the low energy spectra on the total spin S for [Fig. 4.1(a)] the charge neutral system, $N_{el} = 7$ electrons, and [Fig. 4.1(b)] one added electron, i.e., $N_{el} = 8$ electrons. We see that for the charge neutral TGQD with $N_{el} = 7$ electrons the ground state of the system is maximally spin polarized, with $S = 3.5$, indicated by a circle. There is only one possible configuration of all electrons with parallel spins that corresponds to exactly one electron per one degenerate state. The energy of this configuration is well separated from other states with lower total spin S, which require at least one flipped spin among seven initially spin-polarized electrons. An addition of one extra electron to the system with $N_{el} = 7$ spin polarized electrons induces correlations as seen in Fig. 4.1(b), where the cost of flipping one spin is very small. Moreover, for $N_{el} = 8$, the ground state is completely depolarized with $S = 0$, indicated by a circle, but this ground state is almost degenerate with states corresponding to the different total spin.

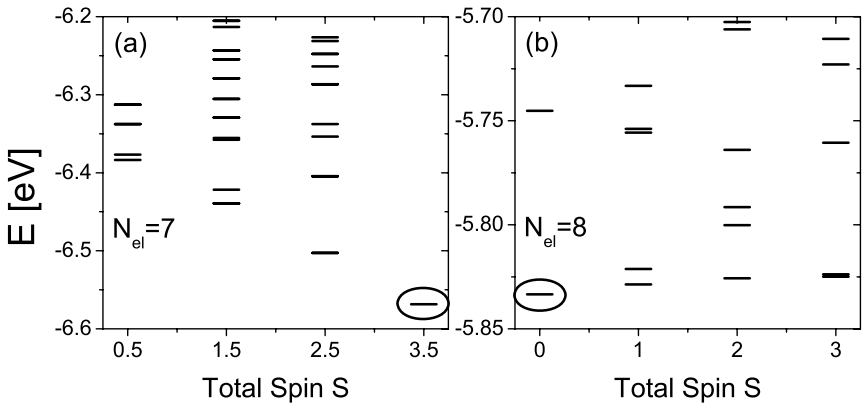

Figure 4.1: The low-energy spectra for the different total spin S for (a) $N_{el} = 7$ electrons and (b) $N_{el} = 8$ electrons. For $N_{el} = 7$ electrons the ground state corresponding to $S = 3.5$, indicated by a circle, is well separated from excited states with different total spin S. For $N_{el} = 8$ electrons the ground state corresponding to $S = 0$, indicated by a circle, is almost degenerate with excited states with different total spin S.

The calculated many-body energy levels, including all spin states for different numbers of electrons (shell filling), are shown in Fig. 4.2. For each electron number, N_{el}, energies are measured from the ground-state energy and scaled by the energy gap of the half-filled shell, corresponding to $N_{el} = 7$ electrons in this case. The solid line shows the evolution of the energy gap as a function of shell filling. The energy gaps for a neutral system , $N_{el} = 7$, as well as for $N_{el} = 7 - 3 = 4$ and $N_{el} = 7 + 3 = 10$ are found to be significantly larger in comparison to the energy gaps for other electron numbers. In addition, close to the half-filled degenerate shell, the reduction of the energy gap is accompanied by an increase of low energy density of states. This is a signature of correlation effects, showing that they can play an important role at different filling factors.

We now extract the total spin and energy gap for each electron number. Figures 4.3(a) and (b) show the phase diagram, the total spin S and an excitation gap as a function of the number of electrons occupying the degenerate shell. The system reveals maximal spin polarization for almost all fillings, with exceptions for $N_{el} = 8, 9$ electrons. However, the energy gaps are found to strongly oscillate as a function of shell filling as a result of a combined effect of correlations and system's geometry. We observe a competition between fully spin polarized system that maximizes exchange energy and fully unpolarized system that maximizes the correlation energy. Only close to the charge

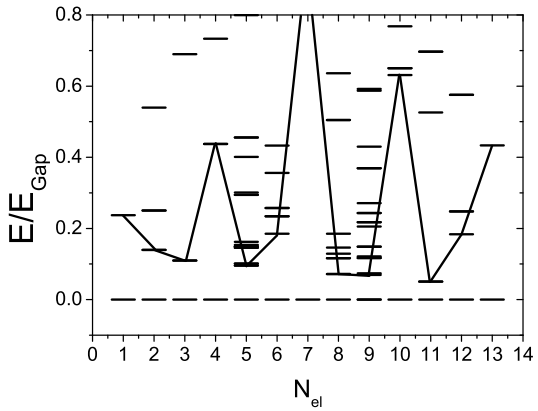

Figure 4.2: The low-energy spectra of the many-body states as a function of the number of electrons occupying the degenerate shell for the system with $N_{deg} = 7$ degenerate states. The energies are renormalized by the energy gap corresponding to the half-filled shell, $N_{el} = 7$ electrons. The solid line shows the evolution of the energy gap as a function of shell filling.

neutrality, for $N_{el} = 8$ and $N_{el} = 9$ electrons, are the correlations sufficiently strong to overcome the large cost of the exchange energy related to flipping spin. The excitation gap is significantly reduced and exhibits large density of states at low energies, as shown in Fig. 4.1. Away from half-filling, we observe larger excitation gaps for $N_{el} = 4$ and $N_{el} = 10$ electrons. These fillings correspond to subtracting/adding three electrons from/to the charge-neutral system with $N_{el} = 7$ electrons. In Fig. 4.4 we show the corresponding spin densities. Here, long range interactions dominate the physics and three spin polarized [Fig. 4.4(a)] holes ($N_{el} = 7 - 3$ electrons) and [Fig. 4.4(b)] electrons ($N_{el} = 7 + 3$ electrons) maximize their relative distance by occupying three consecutive corners. Electron spin density is localized in each corner while holes correspond to missing spin density localized in each corner. We also note that this is not observed for $N_{el} = 3$ electrons filling the degenerate shell (not shown here). The energies of HF orbitals of corner states correspond to three higher energy levels [see Fig. 4.7(c)], with electronic densities shown in Ref. [144]. Thus, $N_{el} = 3$ electrons occupy lower-energy degenerate levels corresponding to sides instead of corners. On the other hand, when $N_{el} = 7$ electrons are added to the shell, self-energies of extra electrons renormalize the energies of HF orbitals. The degenerate shell is again almost perfectly flat similarly to levels obtained within the TB model. A kinetic energy does

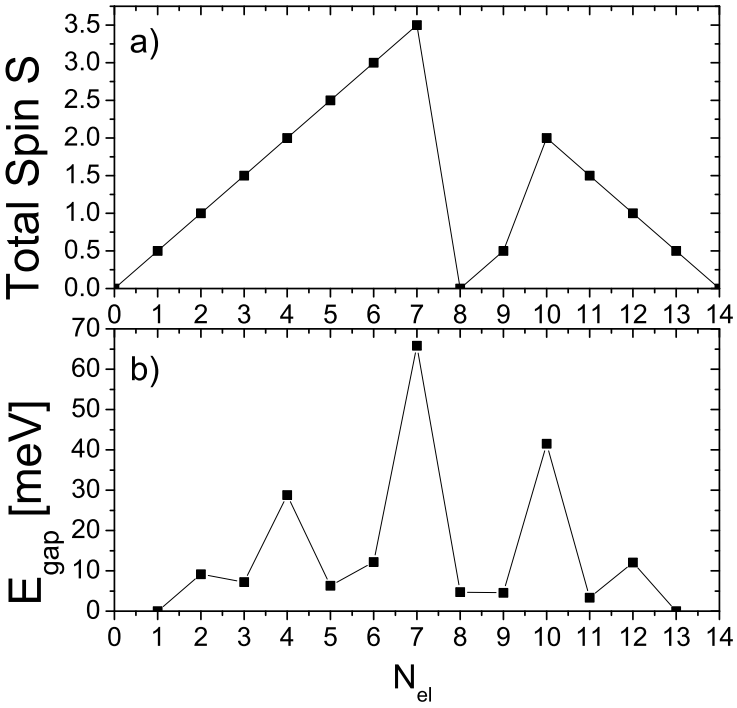

Figure 4.3: (color online) (a) The total spin as a function of the number of electrons occupying the degenerate shell and (b) corresponding the energy excitation gaps. Due to a presence of correlation effects for some fillings, the magnitude of the energy gap is significantly reduced.

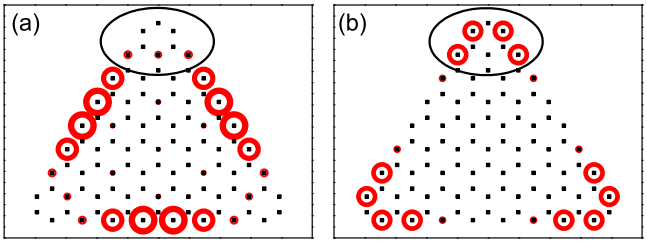

Figure 4.4: (color online) The spin densities of the ground state for (a) $N_{el} = 4$ electrons and (b) $N_{el} = 10$ electrons that correspond to subtracting/adding three electrons from/to the charge neutral system. The radius of circles is proportional to a value of spin density on a given atom. A long range Coulomb interaction repels (a) holes and (b) electrons to three corners, forming a spin-polarized Wigner-like molecule.

not play a role allowing a formation of a spin-polarized Wigner-like molecule, resulting from a long-range interactions and a triangular geometry. We note that Wigner molecules were previously discussed in circular graphene quantum dots with zigzag edges described in the effective mass approximation [184,185]. The rotational symmetry of quantum dot allowed for the construction of an approximate correlated ground state corresponding to either a Wigner-crystal or Laughlin-like state [184]. Later, a variational rotating-electron-molecule (VREM) wave function was used [185]. Unfortunately, due to a lack of an analytical form of a correlated wave function with a triangular symmetry, it is not possible to do it here.

4.1.2 Analysis as a function of size

In a previous section, we have analyzed in detail the electronic properties of a particular TGQD with $N = 97$ atoms as a function of the filling factor $\nu = N_{el}/N_{deg}$, i.e., the number of electrons per number of degenerate levels. In this section we address the important question of whether one can predict the electronic properties of a TGQD as a function of size.

Figure 4.5 shows spin phase diagrams for triangles with odd number of degenerate edge states N_{deg} and increasing size. Clearly, the total spin depends on the filling factor and size of the triangle. However, all charge-neutral systems at $\nu = 1$ are always maximally spin polarized and a complete depolarization occurs for $N_{deg} \leq 9$ for structures with one extra electron added (such

depolarization also occurs for even N_{deg}, not shown). Similar results for small size triangles were obtained in our previous work. [144] However, at $N_{deg} = 11$ we do not observe depolarization for $N_{deg} + 1$ electrons but for $N_{deg} + 3$, where a formation of Wigner-like molecule for a triangle with $N_{deg} = 7$ was observed. We will come back to this problem later. We now focus on the properties close to the charge neutrality.

For the charge-neutral case, the ground state corresponds to only one configuration $|GS\rangle = \prod_i a^\dagger_{i,\downarrow}|0\rangle$ with maximum total S_z and occupation of all degenerate shell levels i by electrons with parallel spin. Here $|0\rangle$ is the HF ground state of all valence electrons. Let us consider the stability of the spin polarized state to single spin flips. We construct spin-flip excitations $|kl\rangle = a^\dagger_{k,\uparrow} a_{l,\downarrow}|GS\rangle$ from the spin-polarized degenerate shell. The spin-up electron interacts with a spin-down "hole" in a spin-polarized state and forms a collective excitation, an exciton. An exciton spectrum is obtained by building an exciton Hamiltonian in the space of electron-hole pair excitations and diagonalizing it numerically, as was done, e.g., for quantum dots. [177] If the energy of the spin flip excitation turns out to be negative in comparison with the spin-polarized ground state, the exciton is bound and the spin-polarized state is unstable. The binding energy of a spin-flip exciton is a difference between the energy of the lowest state with $S = S_z^{max} - 1$ and the energy of the spin-polarized ground state with $S = S_z^{max}$. An advantage of this approach is the ability to test the stability of the spin polarized ground state for much larger TGQD sizes. Figure 4.6 shows the exciton binding energy as a function of the size of TGQD, labeled by a number of the degenerate states N_{deg}. The largest system, with $N_{deg} = 20$, corresponds to a structure consisting of $N = 526$ atoms. The exciton binding energies are always positive, i.e., the exciton does not form a bound state, confirming a stable magnetization of the charge neutral system. The observed ferromagnetic order was also found by other groups based on calculations for small systems with different levels of approximations. [138, 139, 141, 144] The above results confirm predictions based on Lieb's theorem for a Hubbard model on bipartite lattice relating total spin to the broken sublattice symmetry [186]. Unlike in Lieb's theorem, in our calculations many-body interacting Hamiltonian contains direct long-range, exchange, and scattering terms. Moreover, we include next-nearest-neighbor hopping integral in HF self-consistent calculations that slightly violates bipartite lattice property of the system, one of cornerstones of Lieb's arguments [186]. Nevertheless, the main result of the spin-polarized ground state for the charge neutral TGQD seems to be consistent with predictions of Lieb's theorem and, hence, applicable to much larger

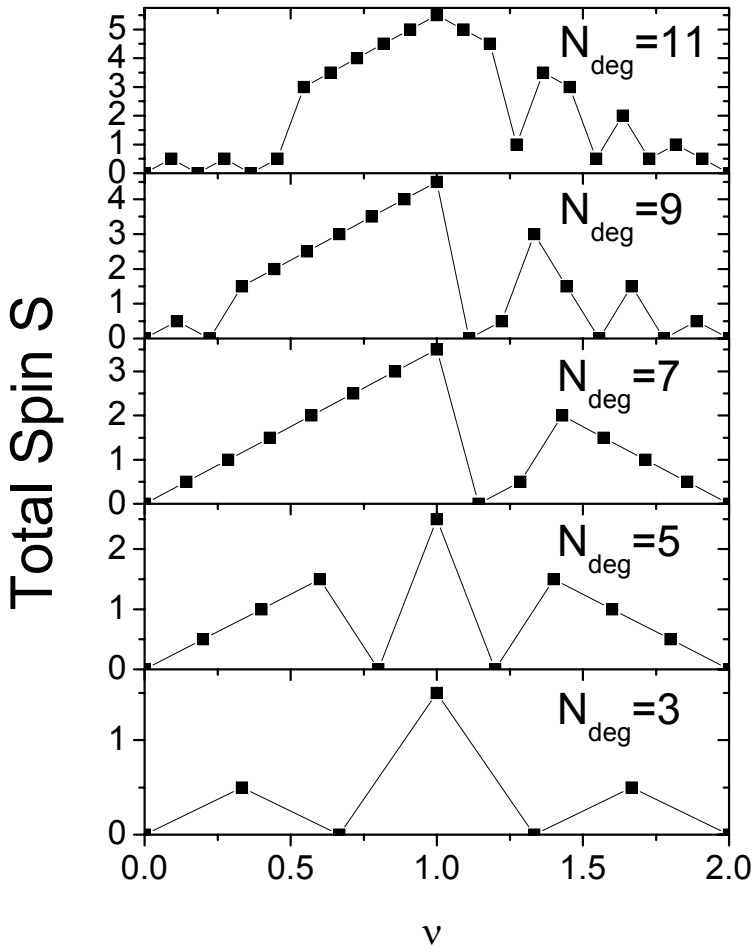

Figure 4.5: Spin phase diagrams as a function of filling factor $\nu = N_{el}/N_{deg}$ for different size triangles characterized by the number of the degenerate edge states N_{deg}. Half-filled shell $\nu = 1$ is always maximally spin polarized. The complete spin depolarization occurs for one added electron to the charge-neutral system for $N_{deg} \leq 9$. For $N_{deg} = 11$ the depolarization effect moves to a different filling.

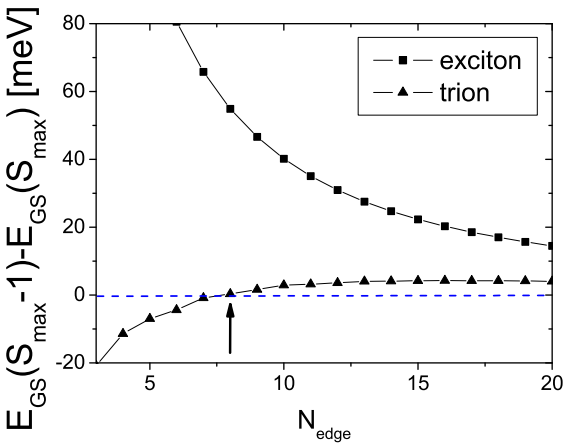

Figure 4.6: Size-dependent analysis based on exciton and trion binding energies. For the charge-neutral system, it is energetically unfavorable to form an exciton, which is characterized by a positive binding energy. The formation of a trion is desirable for small size systems. The phase transition occurs close to $N_{deg} = 8$, indicated by an arrow.

systems.

Having established the spin polarization of the charge-neutral TGQD we now discuss the spin of charged TGQD. We start with a spin-polarized ground state $|GS\rangle$ of a charge-neutral TGQD with all electron spins down and add to it a minority spin electron in any of the degenerate shell states i as $|i\rangle = a^\dagger_{i,\uparrow}|GS\rangle$. The total spin of these states is $S_z^{max} - 1/2$. We next study stability of such states with one minority spin-up electron to spin-flip excitations by forming three particle states $|lki\rangle = a^\dagger_{l,\uparrow}a_{k,\downarrow}a^\dagger_{i,\uparrow}|GS\rangle$ with total spin $S_z^{max} - 1/2 - 1$. Here there are two spin-up electrons and one hole with spin-down in the spin-polarized ground state. The interaction between the two electrons and a hole leads to the formation of trion states. We form a Hamiltonian matrix in the space of three particle configurations and diagonalize it to obtain trion states. If the energy of the lowest trion state with $S_z^{max} - 1/2 - 1$ is lower than the energy of any of the charged TGQD states $|i\rangle$ with $S_z^{max} - 1/2$, the minority spin electron forms a bound state with the spin-flip exciton, a trion, and the spin-polarized state of a charged TGQD is unstable. The trion binding energy, shown in Fig. 4.6, is found to be negative for small systems with $N_{deg} \leq 8$ and positive for all larger systems studied here. The binding of the trion, i.e., the negative binding energy, is consistent with the complete spin depolarization obtained using TB+HF+CI method for TGQD with $N_{deg} \leq 9$ but not observed

for $N_{deg} = 11$ (and not observed for $N_{deg} = 10$, not shown here), as shown in Fig. 4.5. For small systems, a minority spin-up electron triggers spin-flip excitations, which leads to the spin depolarization. With increasing size, the effect of the correlations close to the charge neutrality vanishes. At a critical size, around $N_{deg} = 8$, indicated by an arrow in Fig. 4.6, a quantum phase transition occurs [187], from minimum to maximum total spin.

However, the spin depolarization does not vanish but moves to different filling factors. In Fig. 4.5 we observe that the minimum spin state for the largest structure computed by the TB+HF+CI method with $N_{deg} = 11$ occurs for TGQD charged with additional three electrons. We recall that for TGQD with $N_{deg} = 7$ charged with three additional electrons a formation of a Wigner-like spin polarized molecule was observed, shown in Fig. 4.4. In the following, the differences in the behavior of these two systems, $N_{deg} = 7$ and 11, will be explained based on the analysis of the many-body spectrum of the $N_{deg} = 11$ system.

Figure 4.7 shows the many-body energy spectra for different numbers of electrons for $N_{deg} = 11$ TGQD to be compared with Fig. 4.2 for the $N_{deg} = 7$ structure. Energies are renormalized by the energy gap of a half-filled shell, $N_{el} = 11$ electrons in this case. In contrast to the $N_{deg} = 7$ structure, energy levels corresponding to $N_{el} = N_{deg} + 1$ electrons are sparse, whereas increased low-energy densities of states appear for $N_{el} = N_{deg} + 2$ and $N_{el} = N_{deg} + 3$ electrons. In this structure, electrons are not as strongly confined as for smaller systems. Therefore, for $N_{el} = N_{deg} + 3$ electrons, geometrical effects that lead to the formation of a Wigner-like molecule become less important. Here, correlations dominate, which results in a large low-energy density of states.

4.1.3 Comparison of Hubbard, extended Hubbard and full CI results

In this section, we study the role of different interaction terms included in our calculations. The computational procedure is identical to that described in Sec. 3.6. We start from the TB model but in self-consistent HF and CI calculations we include only specific Coulomb matrix elements. We compare results obtained with Hubbard model with only the on-site term, the extended Hubbard model with on-site plus long range Coulomb interactions, and a model with all direct and exchange terms calculated for up to next-nearest neighbors using Slater orbitals, and all longer range direct Coulomb interaction terms approximated as $\langle ij|V|ji\rangle = 1/(\kappa|r_i - r_j|)$, written in atomic units, 1 a.u.=

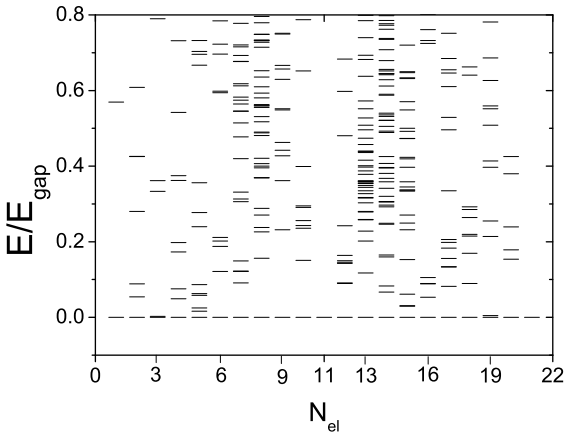

Figure 4.7: The low-energy spectra of the many-body states as a function of the number of electrons occupying the degenerate shell for the triangle with $N_{deg} = 11$ degenerate states. The energies are renormalized by the energy gap corresponding to the half-filled shell, $N_{el} = 11$ electrons. The large density of states related to the correlation effects observed in Fig. 4.2 around $N_{deg} + 1$ electrons shifts to a different filling around $N_{edge} + 3$ electrons.

27.211 eV, where r_i and r_j are positions of i-th and j-th sites, respectively.

The comparison of HF energy levels for the structure with $N_{deg} = 7$ is shown in Fig. 4.8. The on-site U-term slightly removes degeneracy of the perfectly flat shell [Fig. 4.8(a)] and unveils the double valley degeneracy. On the other hand, the direct long-range Coulomb interaction separates three corner states from the rest with a higher energy [Fig. 4.8(b)], forcing the lifting of one of the doubly degenerate subshells. Finally, the inclusion of exchange and scattering terms causes stronger removal of the degeneracy and changes the order of the four lower-lying states. However, the form of the HF orbitals is not affected significantly (not shown here).

In Fig. 4.9 we study the influence of different interacting terms on CI results. The phase diagrams obtained within (a) the Hubbard model and (b) the extended Hubbard model show that all electronic phases are almost always fully spin polarized. The ferromagnetic order for the charge-neutral system is properly predicted. For TGQD charged with electrons, only inclusion of all Coulomb matrix elements correctly predicts the effect of the correlations leading to the complete depolarization for $N_{el} = 8$ and 9. We note that the depolarizations at other filling factors are also observed in Hubbard (at $N_{el} = 2$)) and extended Hubbard calculation (at $N_{el} = 11$)) results.

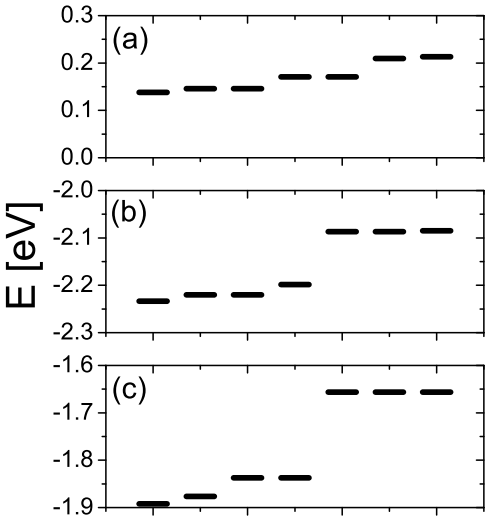

Figure 4.8: Hartree-Fock energy levels corresponding to the degenerate shell for calculations with (a) only the on-site term U (Hubbard model), (b) the on-site term U + direct long-range interaction (extended Hubbard model), and (c) all interactions. A separation of three corner states with higher energies is related to direct long range Coulomb interaction terms.

A more detailed analysis can be done by looking at the energy excitation gaps, which are shown in Fig. 4.10. For the charge-neutral system, all three methods give comparable excitation gaps, in agreement with previous results. [138, 139, 141, 144] In the Hubbard model, the energy gap of the doped system is reduced compared to the charge neutrality but without affecting magnetic properties. The inclusion of a direct long-range interaction in Fig. 4.10(b) induces oscillations of the energy gap. For $N_{el} = N_{deg} + 1$ electrons the energy gap is significantly reduced but the effect is not sufficiently strong to depolarize the system. Further away from half-filling, a large energy gap for models with long-range interactions for $N_{el} = N_{deg} + 3$ appears, corresponding to the formation of a Wigner-like molecule of three spin-polarized electrons in three different corners. The inclusion of exchange and scattering terms slightly reduces the gap but without changing a main effect of Wigner-like molecule formation.

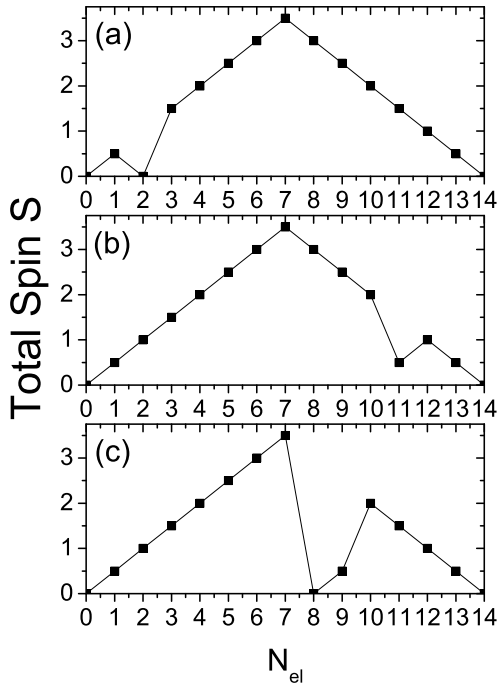

Figure 4.9: Spin phase diagrams obtained by use of the CI method with (a) only the on-site term U (Hubbard model), (b) the on-site term U + direct long range interaction (extended Hubbard model), and (c) all interactions. The ferromagnetic order for the charge-neutral system is properly predicted by all three methods. Correlations leading to the complete depolarization for $N_{el} = N_{deg} + 1$ electrons and $N_{el} = N_{deg} + 2$ electrons are observed only within a full interacting Hamiltonian.

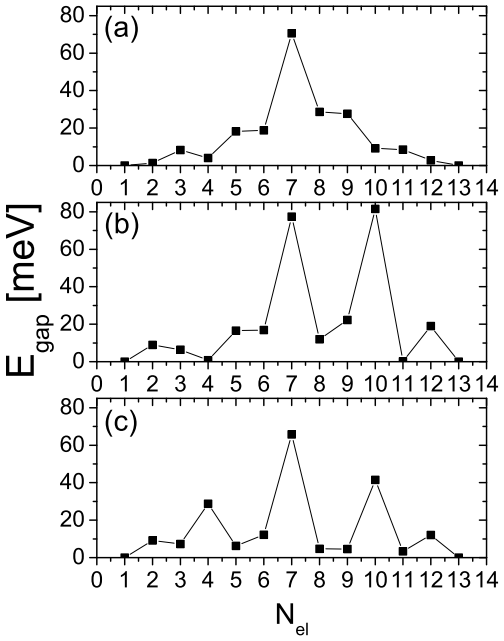

Figure 4.10: The excitation gaps corresponding to phase diagrams from Fig. 4.9 for many-body Hamiltonians with (a) only the on-site term U (Hubbard model), (b) the on-site term U + direct long-range interaction (extended Hubbard model), and (c) all interactions. All three methods give qualitatively similar excitation gaps for the charge neutral system. A large energy gap for $N_{el} = N_{deg} + 3$ electrons, which is related to geometrical properties of the structure, can be obtained by inclusion of direct long-range interactions. This gap is slightly reduced by inclusion of exchange and scattering terms.

4.1.4 Edge reconstruction effects using DFT

The results, presented in this section, were published in a paper "Effect of edge reconstruction and passivation on zero-energy states and magnetism in triangular graphene quantum dots with zigzag edges", by O. Voznyy, A. D. Güçlü, P. Potasz, and P. Hawrylak, Ref. [188]

We would like to analyze the robustness of TGQD the magnetic properties versus edge reconstructions and passivation as a function of size. Calculations have been performed within DFT approach as implemented in the SIESTA code. [189] We have used the generalized gradient approximation (GGA) with the Perdew-Burke-Ernzerhof (PBE) exchange-correlation functional, [190] double-ζ plus polarization (DZP) orbital bases for all atoms (i.e., 2s, 2p, and 2d orbitals for carbon, thus, both σ and π bonds are included on equal footing), Troullier- Martins norm-conserving pseudopotentials to represent the cores, 300-Ry real-space mesh cutoff for charge density (with symmetrization sampling to further improve the convergence), and a supercell with at least 20 Å of vacuum between the periodic images of the TGQDs. Geometries were optimized until the forces on atoms below 40 meV/Å were reached, and exactly the same geometries were used for the comparison of total energies of the ferromagnetic (FM) and antiferromagnetic (AFM) configurations. Our optimized C-C bond length for bulk graphene of 1.424 Å overestimates the experimental value by ∼3%, typical for GGA.

We use the most feasible with current manufacturing technique reconstructions (ZZ and ZZ_{57}) while our conclusions are expected to be general for any configuration of pentagon-heptagon defects. We consider several possible TGQD structures. The requirement of the ZZ_{57} reconstruction of the edge leads to structures with the three rings at the corner, 5-7-5, 7-6-5, or 6-6-5 arrangements presented in Figs. 4.11(b)–(d) (for the sake of comparison of total energies, we investigate only those reconstructions conserving the amount of atoms). Among reconstructed corners, only the structure in Fig. 4.11(b) conserves the mirror symmetry of the TGQD; however, according to our calculations, it is the least stable due to strong distortion of the corner cells. Thus, in the remainder of this paper, we will be presenting results utilizing the configuration shown in Fig. 4.11(c) for an even, and that in Fig. 4.11(d) for an odd N_{edge}.

Passivation by hydrogen is an important requirement for the observation of the band of nonbonding states. Our calculations show that, without hydrogen passivation, the π bonds hybridize with the σ bonds on the edge, destroying

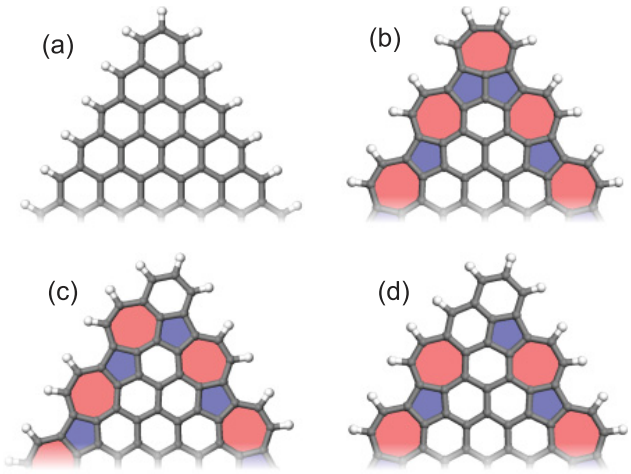

Figure 4.11: Triangular graphene quantum-dot edge configurations considered in this Section: (a) Ideal zigzag edges ZZ, (b) ZZ_{57} reconstruction with pentagon-heptagon-pentagon corner configuration, (c) ZZ_{57} reconstruction with heptagon-hexagon-pentagon corner, and (d) ZZ_{57} reconstruction with hexagon-hexagon-pentagon corner.

the condition of the well-defined equivalent bonds on a bipartite lattice and thus the zero-energy band itself. In Fig. 4.12(a), we address the stability of hydrogen passivation for ZZ and ZZ_{57} edges on the example of a triangle with $N = 97$ carbon atoms, with $N_{edge} = 8$. The number of passivating hydrogens is $N_H = 3N_{edge} + 3 = 27$. For hydrogen-passivated structures, ZZH is 0.3 eV per hydrogen atom more stable than $ZZ_{57}H$ since, in the latter structure, the angles between the σ bonds significantly deviate from the ideal 120^o and the total energy is affected by strain. In the absence of hydrogen, however, the structure has to passivate the dangling σ bonds by itself, e.g. by reconstructing the edge. Indeed, the ZZ_{57} reconstruction becomes 0.4 eV more stable. It is important to note that hydrogen passivation is a favorable process for both structures, even relative to the formation of H_2 molecules, and not only atomic hydrogen, i.e. formation of the $H - H$ bond can not compensate the energy loss due to breaking the $C - H$ bond, Fig. 4.12(a)). The same conclusions hold for larger TGQDs as well. Thus, the H-passivated edge, required for magnetism, is easily achievable and we will present further only the results for hydrogen-passivated structures omitting the index H (i.e., use ZZ instead of ZZH). These results are also consistent with the ones for infinite edges in graphene nanoribbons. In Fig. 4.12(b), we investigate the relative stability of hydrogen-passivated ZZ and ZZ_{57} structures as a function of the linear size

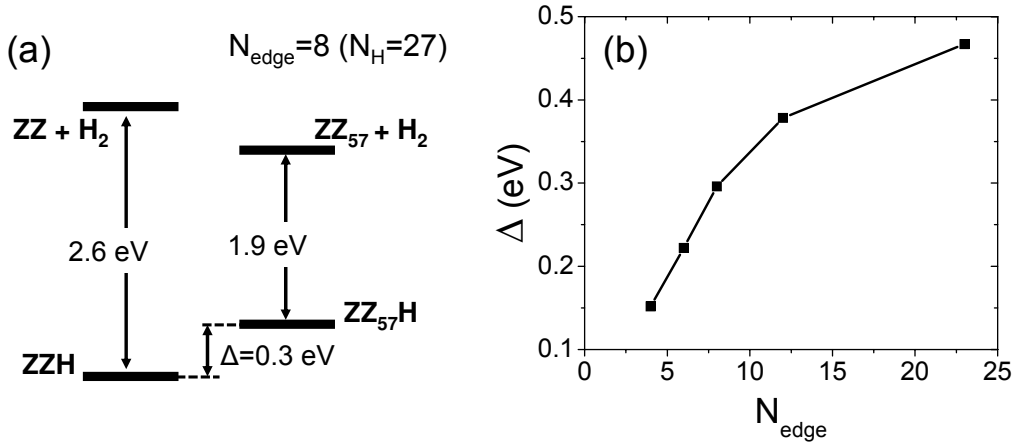

Figure 4.12: Relative total energies of hydrogen-passivated and nonpassivated TGQDs with reconstructed and nonreconstructed edges for the case of $N_{edge} = 8$ ($N_H = 27$). (b) Total energy difference between hydrogen-passivated ZZ_{57} and ZZ configurations as a function of the number of atoms on a side of the triangle. Presented values are energy per hydrogen atom.

of the triangles. The largest TGQD that we have studied has $N = 622$ carbon atoms with $N_{edge} = 23$. The fact that the energy per edge atom increases with size signifies that the infinite limit has not yet been reached. Clearly, the ZZ structure remains the ground state for the range of sizes studied here. Nevertheless, since most of the current experimental techniques involve the unpassivated edge, for which ZZ_{57} is more stable, its consequent hydrogenation may propagate the reconstruction into the final structure, where it may be locked due to high interconversion barrier.

In Sec. 2.2.2 we have proved that the number of zero-energy states equals the difference between the number of A and B type of atoms in the structure, $N_{deg} = |N_A - N_B|$. Additionally, these states are localized exclusively on the sublattice to which the ZZ edges belong, see Fig. 2.6. Figure 4.13 compares the DFT electronic spectra near the Fermi level for the ground states of hydrogen-passivated unreconstructed ZZ) and reconstructed (ZZ_{57}) TGQDs with $N_{edge} = 12$. The degenerate band survives in a reconstructed (ZZ_{57}) TGQD. However, the dispersion of this band increases almost threefold due to a reduction of the structure symmetry. Lifting of the band degeneracy becomes observed even in the nearest-neighbor TB model with equal hoppings (not shown), and is more pronounced for the structures in Figs. 4.11(c) and 4.11(d), which additionally lift the reflection symmetry present in Fig. 4.11(b).

For ZZ triangle the up- and down-spin edge states are split around the Fermi level such that only up-spin states are filled. This is in agreement with our previous TB+HF+CI results presented in Sec. 4.1. The calculated dispersion of the up-spin states is 0.03 eV/state, see Fig. 4.13(a). On the other hand, the ground state of the ZZ_{57} configuration is antiferromagnetic, i.e. there is no splitting between the up- and down-spin states, see Fig. 4.13(b). We can understand it in a following way. An introduction of the ZZ_{57} edge reconstruction smears the distinction between sublattices. One can see from the charge-density plot in Fig. 4.13(b) that degenerate states can now populate both A and B sublattices even close to the center of the dot (see outlined regions), contrary to ZZ triangle, see charge-density plot in Fig 4.13(a)). We speculate that the resulting reduction in the peak charge density on each site is responsible for the reduced on-site repulsion between spin-up and spin-down electrons. Stronger dispersion and reduced up-down spin splitting favor kinetic energy minimization versus exchange energy and destroy the ferromagnetism in ZZ_{57}. It should be noted that partial polarization can still be possible in ZZ_{57}. Particularly, we observed it for structures with symmetric corners [Fig. 4.11(b)], which exhibit smaller dispersion.

Our conclusions based on the analysis of the energy spectra are supported by the total energy calculations depicted in Fig. 4.14. For the ZZ structure, the gap Δ_{min} shown in Fig. 4.13 is always positive and the total energy of the FM configuration is lower than that of AFM (blue squares). For the ZZ_{57} configuration, on the contrary, the ground state clearly remains AFM for all sizes with the exception of the case with $N_{edge} = 4$. Here, the band consists of only $N_{deg} = 3$ degenerate states and their dispersion can not overcome the splitting between spin-up and spin-down states, resulting in FM configuration being more stable. The total energy difference between the FM and AFM configurations for ZZ remains almost constant (in the range 0.3–0.5 eV) for the triangle sizes studied here, and reduces with size if divided by the number of edge atoms. Such a small value, comparable to the numerical accuracy of the method, makes it difficult to make reliable predictions regarding magnetization of larger dots.

To investigate whether the magnetization of the edges would be preserved on a mesoscale, we plot in Fig. 4.15 the evolution of the energy spectra with the TGQD size. For this plot, we performed an additional calculation for the case of $N = 1761$ carbon atoms with $N_{edge} = 40$. We did not perform the geometry optimization for this case due to the high computational cost, however, based on the results for smaller structures, we expect that this would have a minor

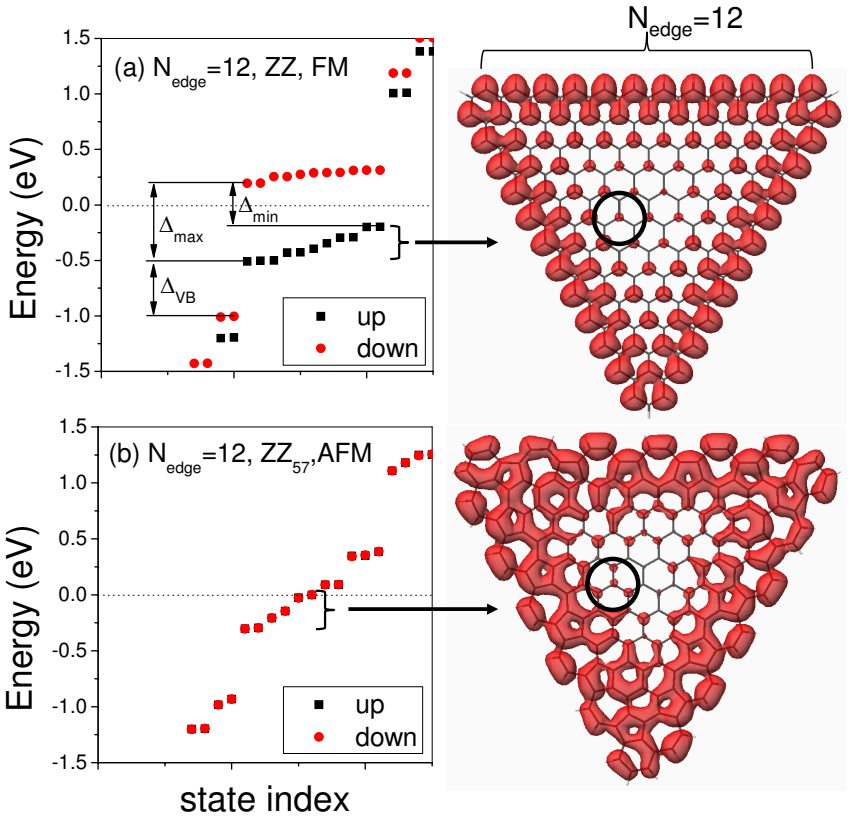

Figure 4.13: Energy spectra of the ground states for (a) ZZ and (b) ZZ_{57} configurations for a hydrogen-passivated triangular dot with $N_{edge} = 12$. Spin-up states are shown in black squares and spindown states are shown in red circles. On the right-hand side, charge densities of the filled part of degenerate bands are shown. Circular outlines show the population of only one sublattice in the ZZ structure and both sublattices in ZZ_{57}.

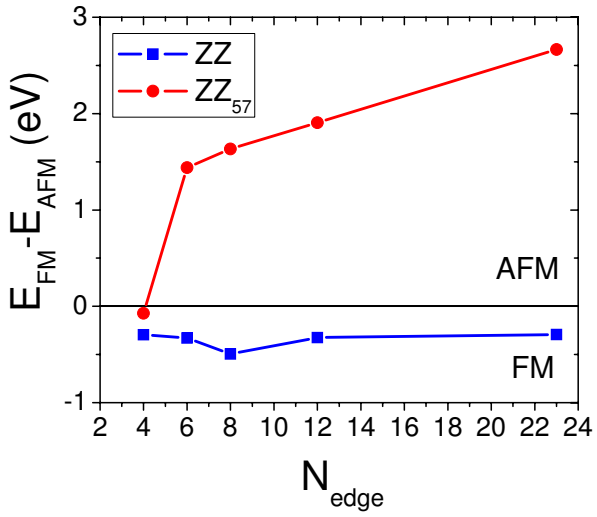

Figure 4.14: Total energy difference between ferromagnetic and antiferromagnetic states as a function of the size of the triangle for hydrogen-passivated ZZ (blue squares) and ZZ_{57} (red circles). For ZZ, the ground state is ferromagnetic for all sizes studied, while for ZZ_{57} it is antiferromagnetic for $N_{edge} > 4$.

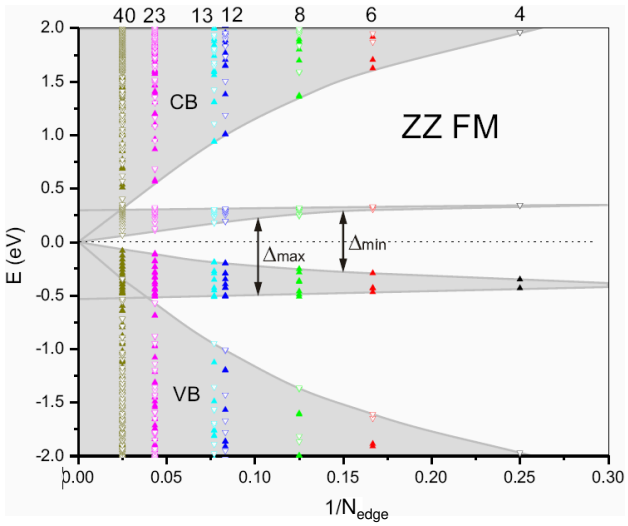

Figure 4.15: Scaling of the energy gaps with the inverse linear size of ZZ TGQDs. Full energy spectra of the structures calculated in this work are shown. Open symbols correspond to spin-down and filled symbols to spin-up states.

effect on the spectrum. This allows us to notice the reduction of the splitting Δ_{max} shown in Fig. 4.13 between the spin-up and spin-down states with the growing size, which was not appreciated previously. Our GGA gap between degenerate bands (Δ_{min}) and that between the valence and conduction bands are larger than LDA gaps reported previously, as also observed for graphene nanoribbons. Both gaps show sublinear behavior, complicating the extrapolation to triangles of infinite size. This behavior, however, should change to linear for larger structures where the effect of edges reduces, converging both gaps to zero, as expected for Dirac fermions. An important difference from the nearest-neighbor TB calculation is the growing dispersion of the zero-energy bands. Combined with the reduction of the valence-conduction gap, this leads to the overlap of the degenerate band with the valence band, even for finite sizes, as indeed observed for the $N_{edge} = 40$ case (see Fig. 4.15), while in ZZ_{57} structures, it becomes visible already at $N_{edge} = 23$ (not shown). Nevertheless, it does not affect the magnetization of the edges, as indeed confirmed by our calculation for $N_{edge} = 40$, and can be compared to a magnetization of the infinitely long hydrogen-passivated nanoribbons, where the edge state overlaps in energy with the valence band but, in k space, those bands do not actually cross. Our results thus suggest that magnetization of the edges for infinitely large triangles survives in the limit of the zero temperature.

4.2 Triangular mesoscopic quantum rings with zigzag edges

The results, presented in this section, were published in a paper "Electronic and magnetic properties of triangular graphene quantum rings", by P. Potasz, A. D. Güçlü, O. Voznyy, J. A. Folk, and P. Hawrylak, Ref. [172].

4.2.1 Properties of the charge neutral system

In order to study magnetic properties of TGQRs, we use Hubbard model with a Hamiltonian given by Eq. 3.19. We would like to check a validity of this model, comparing with results obtained within DFT calculation. In Fig. 4.16 we show spectra obtained (a) from Hubbard model in the mean-field approximation and (b) using DFT implemented in SIESTA package [189] for TGQR with $N_{width} = 2$, consisting of $N = 171$ atoms, $N_{out} = 11$ and $N_{inn} = 2$. This corresponds to $N_{deg} = 9$ degenerate zero-energy TB levels, shown in Fig. 2.14(a). Interactions open a spin dependent gap in the single-particle zero-energy shell, resulting in maximum spin polarization of those states. The total spin of the system is $S_{tot} = 9/2$, in accordance with Lieb's theorem [186]. In Fig. 4.16(c) and 4.16(d) we show corresponding spin density. The net total spin is mostly localized on the outer edge and vanishes as one moves to the center, similar to the electronic densities of TGQD shown in Fig. 2.6(f). Good agreement between results obtained from the mean-field Hubbard and DFT calculations (Fig. 4.16) validates the applicability of the mean-field Hubbard model and allows us to study efficiently structures consisting of larger number of atoms.

In Fig. 4.17 we show the results of the Hubbard model for a larger structure with $N = 315$ atoms, $N_{out} = 20$ and $N_{inn} = 11$, with the same width $N_{width} = 2$. The energy spectrum, Fig. 4.17(a) looks similar to that from Fig. 4.16(a) and the total spin is again $S_{tot} = 9/2$. On the other hand, spin density in Fig. 4.17(b) is different than in Fig. 4.16(c). Here, the outer edge is still spin polarized, but the inner edge reveals opposite polarization. This fact can be understood in the following way. Electrons with majority spin (spin up) occupy degenerate levels of the zero-energy shell which are built exclusively of orbitals localized on atoms belonging to the sublattice labeled as A. These states are localized on the outer edge. Due to repulsive on-site interaction, spin-up electrons repel minority spin electrons (spin down) to sublattice labeled as B. After self-consistent calculations, spin up and spin down densities

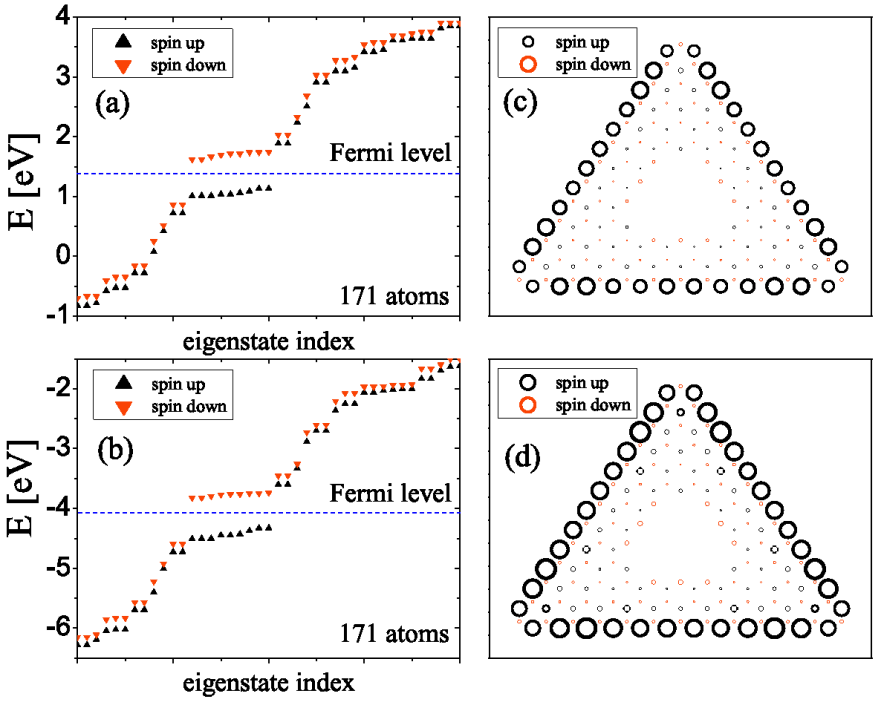

Figure 4.16: (a) Energy spectra from (a) self-consistent mean-field Hubbard model and (b) DFT calculations for TGQR with the width $N_{width} = 2$ and $N = 171$ atoms. States up to the Fermi level (dashed line) are occupied. (c) and (d) are corresponding spin densities. The radius of circles is proportional to the value of spin density on a given atom. Proportions between size of circles in (c) and (d) are not retained.

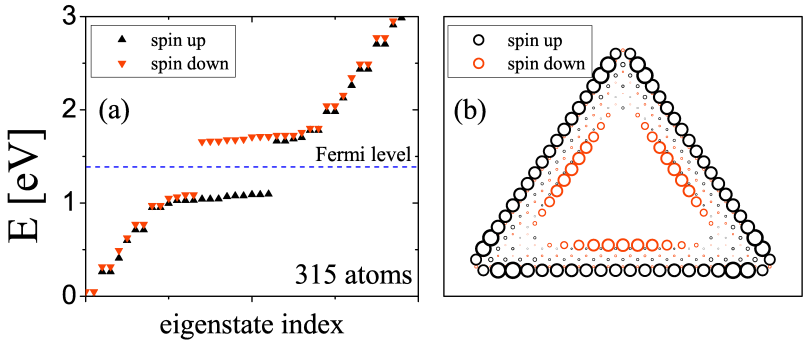

Figure 4.17: (a) Self-consistent energy spectra and (b) corresponding spin densities from mean-field Hubbard model for TGQR with the width $N_{width} = 2$ and $N = 315$ atoms. The radius of circles is proportional to the value of spin density on a given atom.

are spatially separated occupying mostly sublattice A and sublattice B, respectively. Local imbalance between the two sublattices occurs near edges, resulting in local magnetic moments, seen in Fig. 4.17(b). As a result, we observe that the outer and inner edges are oppositely spin polarized, similar to graphene nanoribbons. However, the magnetic moments are not equal resulting in local anti-ferrimagnetic state in contrast to the anti-ferromagnetic state in graphene nanoribbons.

Magnetic moment of the inner edge is the highest close to the middle of the edge and decreases toward the corners. This allows us to distinguish between two types of regions in the structure: corners and edges. Due to triangular symmetry of the system, in further analysis we can focus on only one corner and one edge. We define average magnetization in a given region as $< M >= \sum_i' M_i/N'$, where summation is over sites in a given region and N' is corresponding total number of atoms. In Fig. 4.18(a) we show average magnetization in one corner and one edge as a function of the size of TGQR for a given width, $N_{width} = 2$. Small structures ($N < 200$ atoms) reveal finite and comparable magnetic moments in both regions, consistent with Fig. 4.16(c), where most of the spin density is distributed on outer edges. There are two effects related to increasing size: the length of the internal edge increases increasing spin polarization opposite to the outer edge spin polarization (see Fig. 4.17(b)) and increase of the overall number of atoms in the edge region. The first effect leads to antiferrimagnetic coupling between opposite edges and the second one to vanishing average magnetization, seen in Fig. 4.18(a). We note here that although the average magnetization rapidly decreases with size,

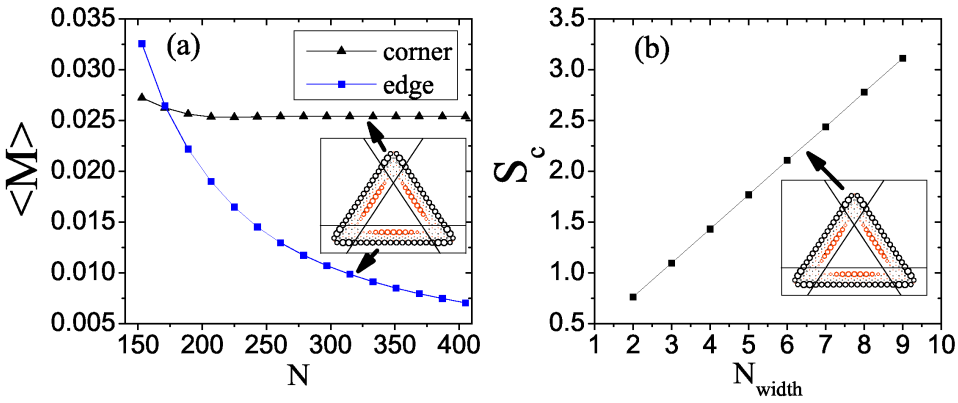

Figure 4.18: (a) Average magnetic moment as a function of size (N - number of atoms) in corner and edge regions. Structures reveal stable ferromagnetic order in corners, but a change from ferromagnetic to antiferromagnetic on edges with increasing size. (b) Total spin in corner region as a function of width. Linear dependence is due to increased number of zero-energy states.

it never approaches zero. On the other hand, average magnetization at the corner is stable and nearly independent of the size. This fact is related to the fixed number of atoms in the corner region.

According to Liebs theorem [186], the total spin of the system must be $S = 3(N_{width}+1)/2$. Moreover, the spin density for smaller structures is equally distributed along the outer edge (see Fig. 4.16(c)). Partitioning structure into six approximately equal regions, three corners and three edges (see inset in Fig. 4.18(a)), gives approximately equal total spin in each domain. In further analysis we show that this is true for arbitrary size triangular rings. In Fig. 4.18(b), we present the total spin in one corner $S_c = \sum_i' M_i$ as a function of the width of the ring. Summation is over all sites in one corner. We obtain linear dependence $S_c \sim N_{width}$, which for the best choice of cuts should be described by relation $S_c = (N_{width} + 1)/4$, which is a one sixth of the total spin S of the entire structure. In this ideal case, all six regions reveal equal total spin S_c, independently of the size of the structure. We relate this fact to the behavior in edge and corner regions. For sufficiently large structures, magnetic moments on edge region are distributed on large number of atoms, giving vanishing average magnetic moment but always finite total spin equal to $S_c = (N_{width}+1)/4$. With increasing size, the length of the inner edge increases. In order to satisfy relation $S_c = (N_{width}+1)/4$, magnetic moment on the outer edge increases proportionally to oppositely polarized magnetic moment on the inner edge, resulting in antiferromagnetic coupling between opposite edges. On

the other hand, in corners, there is always a fixed number of atoms independent of size, giving constant average magnetic moment and the total spin equal to $S_c = (N_{width} + 1)/4$. We note that above conclusion were confirmed by investigation of TGQR with width in the range $2 \leq N_{width} \leq 9$ for structures up to $N = 1500$ atoms. Thus, we can treat large TGQR as consisting of three ferromagnetic corners connected by anti-ferrimagnetic ribbons, with ribbons exhibiting finite total spin. This result can be useful in designing spintronic devices. Choosing TQGR with proper width, one can obtain a system with desired magnetic moment localized in the corners.

4.2.2 Analysis as a function of filling factor

In a previous Section, we have shown that the Hubbard model and DFT calculations describe well properties of the charge neutral system. On the other hand, in Sec. 4.1 was shown that gated TGQDs reveal effects related to electronic correlations in partially filled zero-energy shell [144]. We expect a similar behavior in TGQRs. Thus, in this Section, we use again a TB+HF+CI method described in Sec. 3.6 to analysis the magnetic properties as a function of the number electrons filling the degenerate shell.

We concentrate on the structure shown in Fig. 2.13, consisting of $N = 171$ atoms and characterized by $N_{width} = 2$, which correspond to $N_{deg} = 9$ degenerate states. In Fig. 4.19(a) we show an example of a configuration related to $N_{el} = 10$ electrons. This corresponds to a half-filled degenerate shell with all spin down states of the shell filled and one additional spin up electron. For maximal total spin $S = 4$ there are nine possible configurations corresponding to the nine possible states of spin-up electron. An energy spectrum obtained by diagonalizing full many-body Hamiltonian, Eq. 3.21, for total spin $S = 4$ is shown in Fig. 4.19(c). We see that, by the comparison with total spin states with $S = 0, 1, .., 4$, the ground state corresponding to configurations of the type a (one of which is shown in Fig. 4.19(a)) is maximally spin polarized, with the excitation gap in the $S = 4$ subspace of ~ 40 meV. However, the lowest energy excitations correspond to spin flip configurations with total spin $S = 3$, one of which is shown Fig. 4.19(b). These configurations involve spin flip excitations from the fully spin polarized electronic shell in the presence of one additional spin up electron.

The energy $E_{gap} = 4$ meV for $N_{el} = 10$, indicated by the arrow in Fig. 4.19(c), is shown in Fig. 4.20(a) together with the energy gap for all electron numbers $1 < N_{el} < 18$ and hence all filling factors. In Fig. 4.20(b), we show

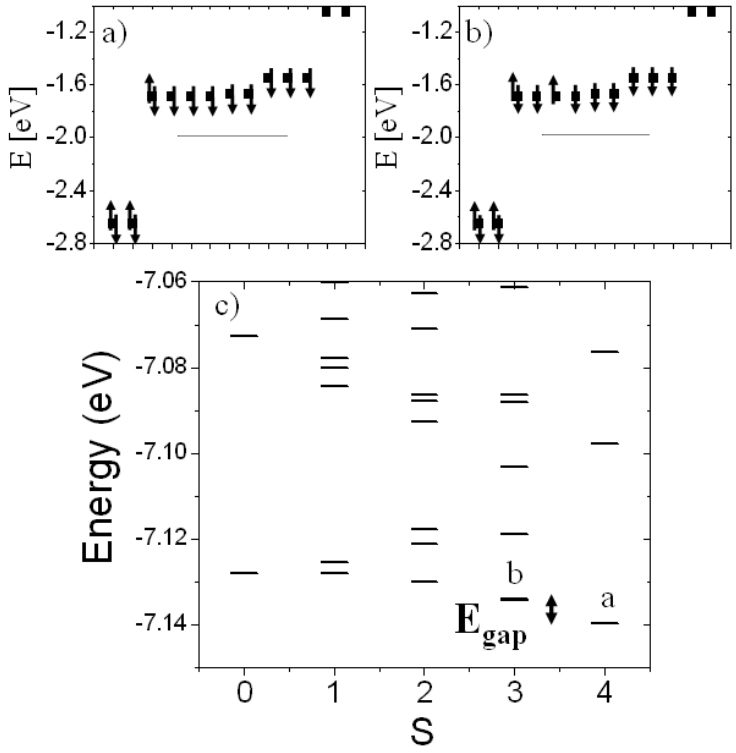

Figure 4.19: (a) and (b) Hartree-Fock energy levels for TGQR with $N_{width} = 2$ consisting of $N = 171$ atoms and filled by $N_{el} = 10$ electrons. The configuration represented by arrows in (a) corresponds to all occupied spin down orbitals and one occupied spin up orbital. The configuration represented by arrows in (b) is the configuration from (a) with one spin down flipped. (c) The low-energy spectra for the different total spin S for $N_{el} = 10$ electrons. The ground state has $S = 4$, indicated by a, with one of the configuration shown in (a). The lowest energy excited state, indicated by b, is ~ 4 meV higher in energy, corresponds to spin-flip configurations with one of the configuration shown in (b).

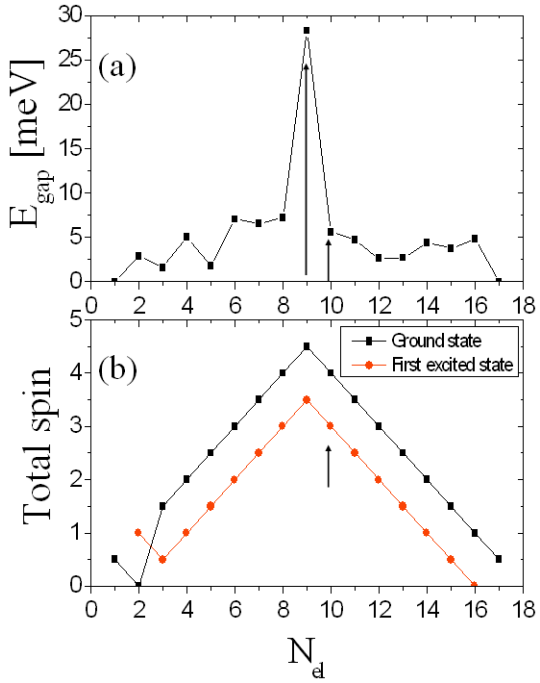

Figure 4.20: (a) Energy spin gap between ground and first excited state. Black long arrow corresponds to half-filled shell with $E_{gap} \sim 28$ meV. Significant reduction in the spin flip energy gap for one additional electron, $E_{gap} \sim 4$ meV, indicated by the small black arrow, is the signature of correlation effects. (b) Total spin of the ground and first excited state as a function of the number of electrons N_{el}. The small black arrow indicates excited state for $N_{el} = 10$ electrons with one of the configurations shown schematically with arrows in Fig. 4.19(b).

the total spin S of the ground and the first excited state as a function of the number of electrons occupying the degenerate shell. For arbitrary filling, except for $N_{el} = 2$, the ground state is maximally spin polarized. Moreover, the first excited state has total spin consistent with spin flip excitation from the maximally spin polarized ground state as discussed in detail for $N_{el} = 10$. The signature of correlation effects is seen in the dependence of the excitation gap on the shell filling, shown in Fig. 4.20(a). For the half-filling at $N_{el} = 9$, indicated by an arrow, the excitations are spin flip excitations from the spin polarized zero-energy shell. This energy gap, ~ 28 meV, is significantly larger in comparison with the energy gap of ~ 4 meV for spin flips in the presence of additional spin up electron. The correlations induced by additional spin up electron lead to a much smaller spin-flip excitation gap. This is to be compared with TGQDs where spin flip excitations have lower energy leading to full depolarization of the ground state, what was shown in Sec. 4.1 [144].

4.3 Hexagonal mesoscopic quantum rings

The results, presented in this section, were published in a paper "Spin and electronic correlations in gated graphene quantum rings", by P. Potasz, A. D. Güçlü, and P. Hawrylak, Ref. [173].

4.3.1 Analysis as a function of size

In this section, we study the ground and excited states as a function of the number of additional interacting electrons in degenerate shells of hexagonal quantum rings with different size L and $W = 1$. Figure 4.21 shows the low energy spectra for the different total spin S of half filled first shell over the Fermi energy for two thinnest rings with a) $L = 4$ and $N = 96$ atoms and b) $L = 8$ and $N = 192$ atoms. For smaller ring the ground state has total spin $S = 1$ with a very small gap to the first excited state with $S = 0$. The lowest states with larger total spin have higher energies. For $N = 192$ atoms ring the total spin of the ground state is maximal, $S = 3$. The lowest levels with different total spin have slightly higher energies. This can be understood in a following way. The splitting between levels is large for smaller structures, which is seen in Fig. 2.19. For ring with $L = 4$ and $N = 96$ atoms this value, 0.17 eV, is comparable with electronic interaction terms, e. g. 0.34 eV for two electrons occupying the lowest state. For ring with $L = 8$ and $N = 192$ atoms the electron-electron interaction terms are 0.23 eV for interaction between two

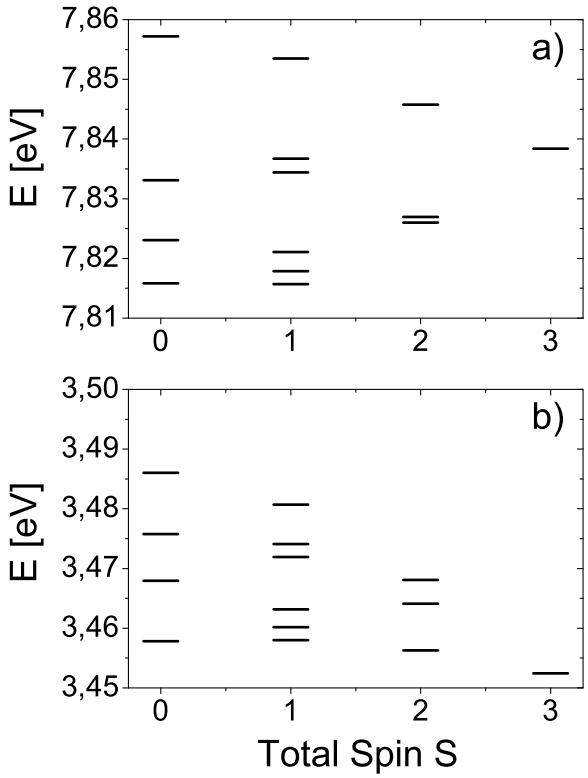

Figure 4.21: The low energy spectra for the different total spin S of half-filled first shell over the Fermi energy for two thinnest rings $W = 1$ with (a) $L = 4$ and $N = 96$ atoms and (b) $L = 8$ and $N = 192$ atoms.

particles on the first state, which is much larger then single particle energy difference 0.015 eV. From this, we clearly see that for ring with $L = 4$ it is energetically favorable to occupy low energy states by electrons with opposite spins. For ring with $L = 8$ all states have similar energies and due to exchange interactions the lowest energy state is maximally spin polarized.

The behavior of magnetic properties of the ground state for half filled shell as a function of size is shown in Fig. 4.22. In this case, the ground state spin can be explained as a result of the competition between occupation of levels with smallest single particle energies which favors opposite spin configurations, and parallel spin configurations for which exchange interactions are maximized. For rings with $L \geq 5$ the ground state is maximally spin polarized. Here, the splitting between levels is relatively small and the ground state is determined by electronic interactions. Moreover, this splitting decreases with increasing size and this is seen in the spin gap behavior (Fig. 4.22). The largest spin gap is observed for ring with $L = 6$ and it decreases with increasing L. For small rings the situation is more complicated. Here, the contributions from single particle energies and interactions are comparable. As a consequence, we observe ground

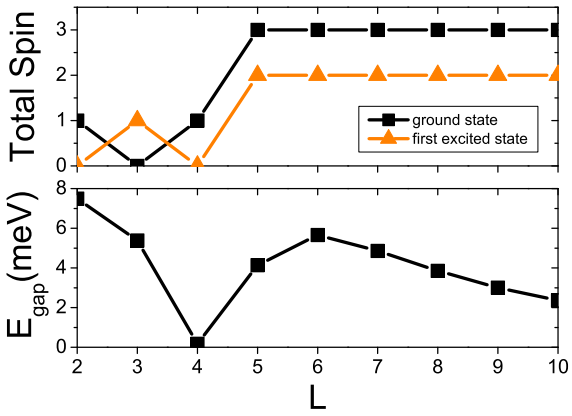

Figure 4.22: Upper: Total spin of the ground and first excited states for the half-filling of the first shell in the thinnest ring structures $W = 1$ with different sizes. Lower: Corresponding energy spin gap between ground and first excited states.

states with alternating total spin $S = 1$ and $S = 0$. For sufficiently large rings, $L > 5$, we observe stabilization of the spin phase diagram. This is connected to changes of the energy differences between levels in a shell - above a critical size these values are so small that they don't play a role anymore.

4.3.2 Analysis as a function of filling factor

In Fig. 4.23 we show the phase diagram for a ring with $L = 8$ and $N = 192$ atoms. Near the half-filling the ground state is maximally spin polarized which is related to the dominant contribution from the short-ranged exchange interaction terms, and the charge density is symmetrically distributed in the entire ring (see Fig. 2.18). Adding or removing electrons causes irregularities in the density distribution, and correlation effects start becoming important. This results in an alternating spin between maximal polarization (e.g. 3, 4, 9 extra electrons) and complete depolarization (e.g. 2, 8, 10 extra electrons) of the system.

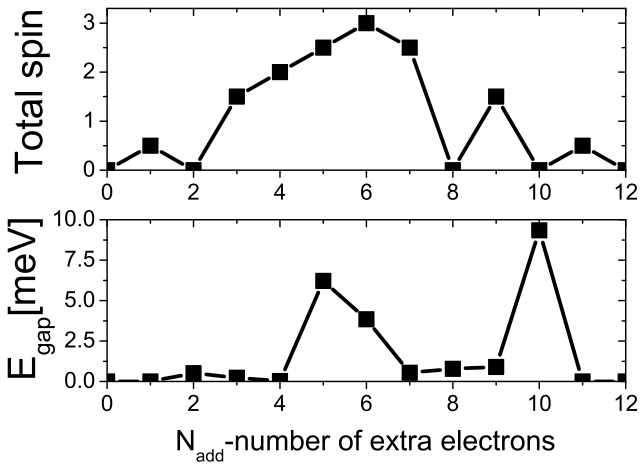

Figure 4.23: Upper: The spin phase diagram for electrons occupying the first shell over the Fermi level of the ring structure with $L = 8$ and $N = 192$ atoms. Lower: Corresponding energy spin gap between ground and first excited states.

Chapter 5

Optical properties of graphene nanostructures

The results, presented in this chapter, were published in a paper "Excitonic absorption in gate-controlled graphene quantum dots", by A. D. Güçlü, P. Potasz, and P. Hawrylak, Ref. [155].

5.1 Size, shape and type of edge dependence of the energy gap

The electronic properties of graphene quantum dots depend on the size, shape, and the character of the edge. This was illustrated by comparing electronic properties of graphene quantum dots including (i) hexagonal dot with armchair edges, (ii) triangular dot with armchair edges, (iii) hexagonal dot with zigzag edges, and (iV) triangular dot with zigzag edges (see Fig. 2.2). Due to similarity of energy spectra of structures with armchair edges, we can neglect a triangular shape structure and focus on a hexagonal one. Thus, we consider hexagonal dots with armchair and zigzag edges and triangular dot with zigzag edges. The dependence of the energy gap on the number of atoms N is plotted in Fig. 5.1. In the inset in the left down corner, the energy spectrum for $N = 114$ hexagonal quantum dot with armchair edges from Fig. 2.2(a) is redrawn. The double headed red arrow indicates the band gap separating the occupied valence band states from the empty conduction band states. In this case, the gap decays as the inverse of the square root of number of atoms N, from hundred to million atom nanostructures. This is expected for confined Dirac fermions with photon-like linear energy dispersion $E_{gap} \propto k_{min} \simeq 2\pi/\Delta x \propto 1/\sqrt{N}$ as pointed out in Refs [140, 154, 155, 170].

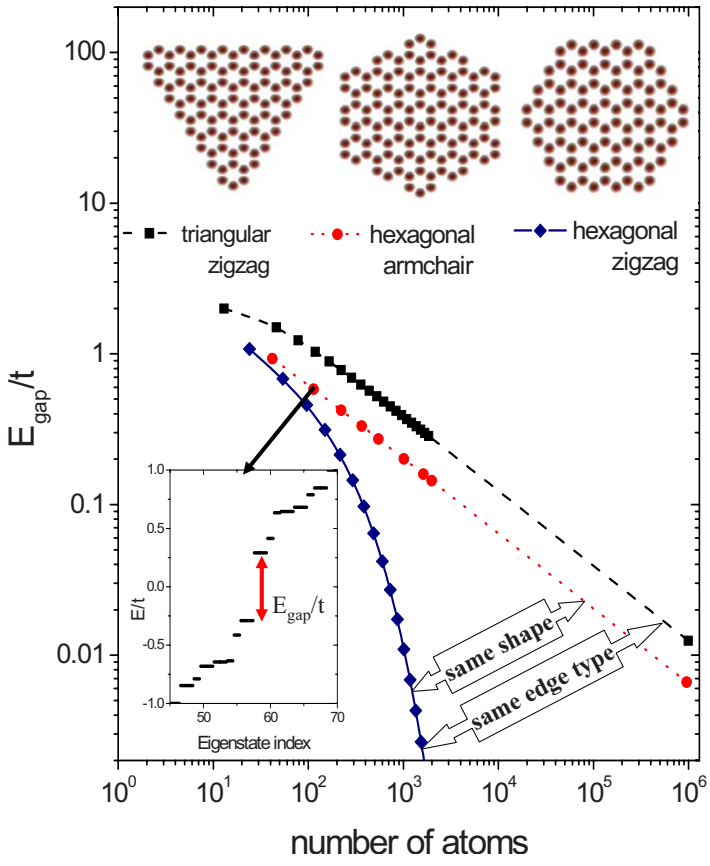

Figure 5.1: TB bandgap energy as a function of total number of atoms N for a triangular zigzag quantum dot (dashed line with black squares), hexagonal armchair quantum dot (dotted line with circles), and hexagonal zigzag quantum dot (solid line with diamonds). The inset shows the TB energy spectrum for the hexagonal armchair dot redrawn from Fig. 2.2(a).

However, in contrast with the hexagonal geometry with armchair edges, the energy gap of hexagonal structure with zigzag edges decreases rapidly as the number of atoms increases. This is due to the zigzag edges leading to localized states at the edge of the quantum dot what was shown in Fig. 2.3(c). It is similar to whispering gallery modes of photons localized at the edge of photonic microdisk [191]. In TGQD, as was shown in Sec. 2.2, in addition to valence and conduction bands, the spectrum shows a shell of degenerate levels at the Fermi level. According to results from Sec. 4.1, as the shell is half-filled at charge neutrality, there is no unique way of defining the energy gap. Here we define the band gap as the energy difference between the topmost valence (above the degenerate shell) to the lowest conduction band state (below the degenerate shell). Despite the presence of the zero-energy shell, the energy gap in the triangular zigzag structure follows the power law $E_{gap} \propto 1/\sqrt{N}$. We note that the energy gap changes from $E_{gap} \simeq 2.5$ eV (green light) for a quantum dot with $N \simeq 100$ atoms and a diameter ~ 1 nm to $E_{gap} \simeq 30$ meV for a quantum dot with $N \simeq 10^6$ atoms and a diameter ~ 100 nm.

5.2 Optical joint density of states

We compare the optical joint density of states calculated using dipole moments $\langle i|\mathbf{r}|f\rangle$ connecting initial and final states with energies E_i and E_f, respectively. We calculate it for the three structures of similar size with energy spectra from Fig. 2.2(a), (c) and (d). The dipole transitions for the hexagonal armchair structure with $N = 114$ shown in Fig. 5.2(a) are not particularly different from those for the hexagonal zigzag structure shown in Fig. 5.2(b). However, for the triangular zigzag structure we observe a group of dipole moments near $E = 0$ which is absent in the two other structures. Indeed, due to the presence of the zero-energy band in the middle of the energy gap, several different photon energies (shown using different colors online) corresponding to transitions within the zero-energy band, into and out of the zero-energy states, and valence to conduction band states are possible.

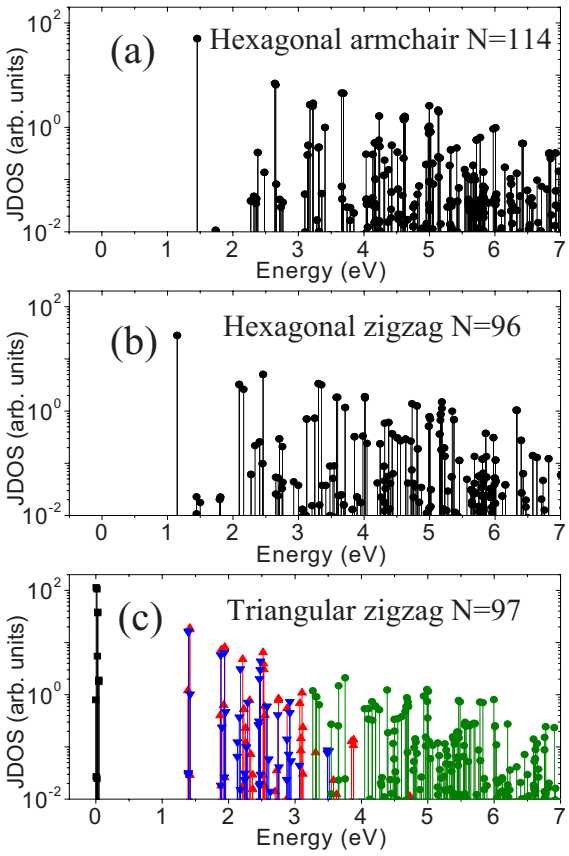

Figure 5.2: Optical joint density of states for (a) hexagonal armchair structure with $N = 114$ atoms, (b) hexagonal zigzag structure with $N = 96$ atoms, and (c) triangular zigzag structure with N=97 atoms. Due to the presence of zero-energy states in triangular zigzag structure, different classes of optical transitions exist represented by different symbols (and colors online).

5.3 Triangular graphene quantum dots with zigzag edges

5.3.1 Excitons in graphene quantum dots

In order to take into account correlation and excitonic effects, we solve the many-body Hamiltonian given by

$$\begin{aligned} H &= \sum_{s'\sigma} \epsilon_{s'\sigma} a^\dagger_{s'\sigma} a_{s'\sigma} + \sum_{s\sigma} \epsilon_{s\sigma} h^\dagger_{s\sigma} h_{s\sigma} \\ &+ \frac{1}{2} \sum_{\substack{s',p',d',f',\\ \sigma\sigma'}} \langle s'p'|V|d'f'\rangle a^\dagger_{s'\sigma} a^\dagger_{p'\sigma'} a_{d'\sigma'} a_{f'\sigma} + \frac{1}{2} \sum_{\substack{s,p,d,f,\\ \sigma\sigma'}} \langle sp|V|df\rangle h^\dagger_{s\sigma} h^\dagger_{p\sigma'} h_{d\sigma'} h_{f\sigma} \\ &+ \sum_{\substack{s',p,d,f',\\ \sigma\sigma'}} \left(\langle ds'|V_{ee}|f'p\rangle - (1-\delta_{\sigma\sigma'}) \langle ds'|V_{ee}|pf'\rangle \right) a^\dagger_{s\sigma} h^\dagger_{p\sigma'} h_{d\sigma'} a_{f'\sigma}, \end{aligned} \tag{5.1}$$

where indices (s, p, d, f) correspond to states below Fermi level, and (s', p', d', f') are above Fermi level. Operators $h^\dagger_{s\sigma}(h_{s\sigma})$ create (annihilate) a hole in the valence band of TB+HF quasi particles. Terms from the first line corresponds to kinetic energies of electrons and holes. Terms from the second line correspond to, the first term, interactions between electrons and, the second term, interactions between holes. Terms from the third line describe, the first term, attractive direct interaction and, the second term, repulsive exchange interaction between an electron and a hole. Excitonic absorption spectrum between the ground state $|GS\rangle$ and final excited states $|f\rangle$ can then be calculated using

$$A(\omega) = \sum_f |\langle GS|P|f\rangle \delta(\omega - (E_f - E_{GS})), \tag{5.2}$$

where $P = \sum_{ss'} \delta_{\sigma\bar{\sigma'}} \langle s|P|s'\rangle h_{s\sigma} a_{s'\sigma'}$ is the polarization operator. We now focus on TGQD with $N = 97$, for which exact many-body calculations can be carried out. For the charge neutral case, each state is singly occupied and all electrons have parallel spin, what was shown in Sec. 4.1. We can classify allowed optical transitions into four classes, as shown in Fig. 5.3(a): (i) from valence band to zero-energy degenerate band (VZ transitions, blue color); (ii) from zero-energy band to conduction band (ZC transitions, red color); (iii) from valence band to conduction band (VC transitions, green color); and finally, (iv) within zero-energy states (ZZ transitions, black color). As a consequence, there are three different photon energy scales involved in the absorption spectrum. VC transitions (green) occur above full bandgap (2.8 eV), VZ (blue) and ZC (red) transitions occur starting at half band gap (1.4 eV), and ZZ (black) transitions

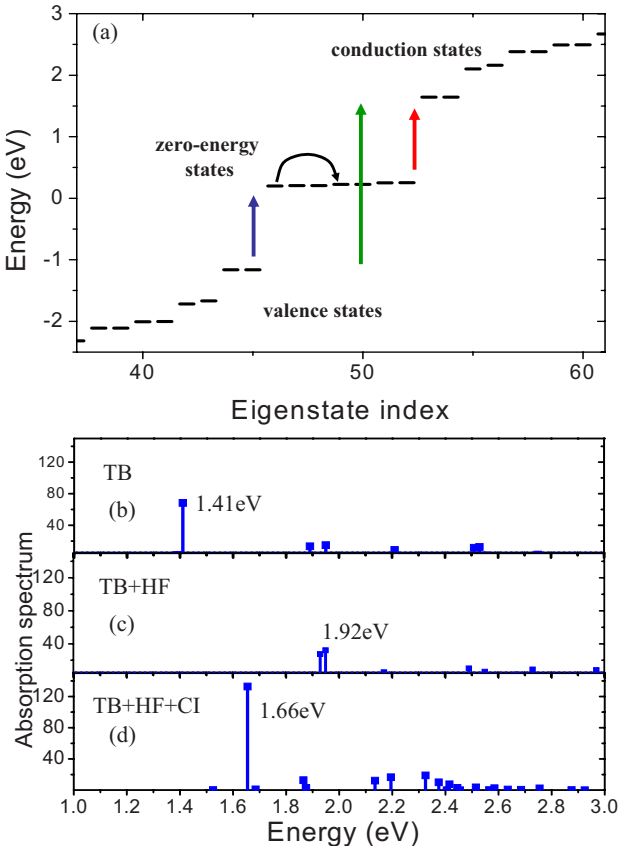

Figure 5.3: (a) Possible optical transitions in TGQD consisting of $N = 97$ atoms. The colored arrows represent optical transitions from VC (green), VZ (blue), ZC (red), and ZZ (black). (b)–(d) shows the effect of electron-electron interactions on the VZ transitions within (c) Hartree-Fock approximation, and including (d) correlations and excitonic effect obtained from exact configuration interaction calculations.

occur at tera-hertz energies. The energies corresponding to ZZ transitions are controlled by the second-nearest-neighbor tunneling matrix element t' and by electron-electron interactions. Figures 5.3(b)–5.3(d) illustrates in detail the effect of electron-electron and final-state (excitonic) interactions on the absorption spectra. Figure 5.3(b) shows detailed VZ absorption spectrum for noninteracting electrons. This spectrum corresponds to transitions from the filled valence band to half filled shell of $N_{deg} = 7$ zero-energy states. Half filling implies that each state of the zero-energy band is optically allowed. According to electronic densities of the degenerate states shown in Fig. 2.6, among the $N_{deg} = 7$ zero-energy states, there are two bulk-like states, 2.6(d) and (e), which couple strongly to the valence band resulting in the main transition at $E = 1.41$ eV. When the electron-electron interactions are turned on within Hartree-Fock level, the photon energies corresponding to optical transitions $\omega = (E_f + \sum_f) - (E_i + \sum_i)$ are renormalized by the difference in quasi particle self-energies $\sum_f - \sum_i$. The absorption spectrum, shown in Fig. 5.3(c), is renormalized with transition energies blue-shifted by 0.51 eV to $E = 1.92$ eV. Finally, when final state interactions between all interacting quasi electron and quasi hole states are taken into account, the excitonic spectrum is again renormalized from the quasi particle spectrum, with transitions red shifted from quasi particle transitions at $E = 1.92$ eV, down to $E = 1.66$ eV. As we can see, electron-electron interactions play an important role in determining energies and form of the absorption spectrum, with net blue-shift from the noninteracting spectrum by 0.25 eV.

5.3.2 Charged excitons in interacting charged quantum dots

We now turn to the analysis of the effect of carrier density on the optical properties of graphene quantum dots. The finite carrier density, controlled by either metallic gate or via doping (intercalation), has been shown to significantly modify optical properties of graphene [13, 14, 192, 193]. For a quantum dot, the metallic gate shown in Fig. 5.4(a), changes the number of electrons in the degenerate shell from $N_{deg} = 7$ to $N_{deg} + \Delta N_{deg}$. This is illustrated in Fig. 5.4(b) where four electrons were removed and three electrons remain. These remaining electrons populate degenerate shell and their properties are entirely controlled by their interaction. Alternatively, removal of electrons from charge neutral shell corresponds to addition of holes. As is clear from Fig. 5.4(b), such a removal of electrons allows intra-shell transitions ZZ, enhances VZ tran-

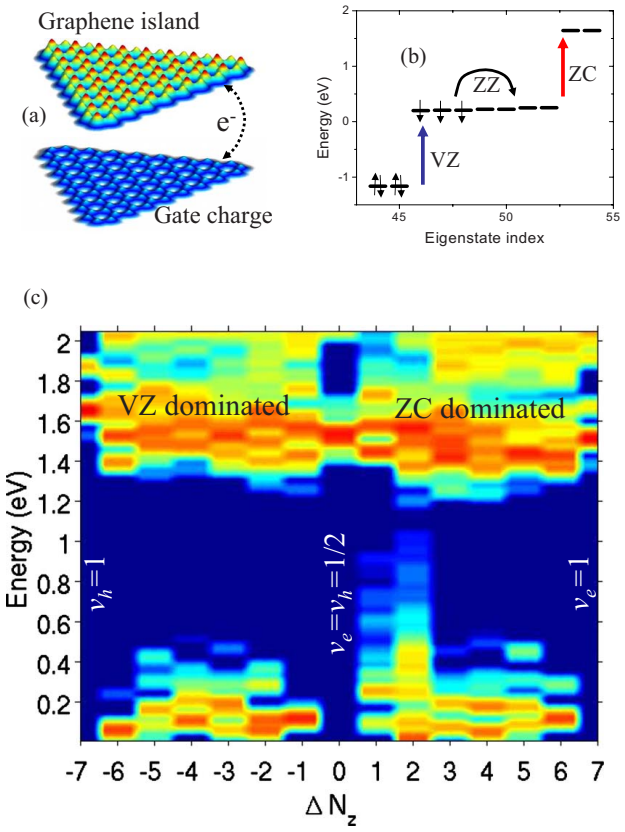

Figure 5.4: (Color online) (a) Schematic representation of TGQD with $N = 97$ carbon atoms with four electrons moved to the metallic gate. (b) Corresponding single particle TB configuration near the Fermi level. (c) Excitonic absorption spectrum in arbitrary units as a function of energy and charging ΔN_{deg}. For convenience, transitions are artificially broadened by 0.02 eV. Peaks below 0.6 eV are due to ZZ transitions, peaks above 1.2 eV are due to VZ and ZC transitions. Charge neutral case corresponds to $\Delta N_{deg} = 0$ (filling factors $\nu_e = \nu_h = 1/2$).

sitions by increasing the number of allowed final states and weakens the ZC transitions by decreasing the number of occupied initial states. Figure 5.4(c) illustrates the overall effects in the computed excitonic absorption spectra for VZ, ZC, and ZZ transitions as a function of the number of additional electrons N_{deg}. At $\Delta N_{deg} = -7$ (hole-filling factor $\nu_h = 1$), the shell is empty and VZ transitions describe an exciton built of a hole in the valence band and an electron in the degenerate shell. The absorption spectrum has been described in Figs. 5.3(b)–5.3(d) and is composed of one main excitonic peak at 1.66 eV. There are no ZC transitions and no ZZ transitions in the tera-hertz range. When we populate the shell with electrons, the VZ excitonic transition turns into a band of red-shifted transitions corresponding to an exciton interacting with additional electrons, in analogy to optical processes in the fractional quantum Hall effect and charged semiconductor quantum dots. As the shell filling increases, the number of available states decreases and the VZ transitions are quenched while ZC and ZZ transitions are enhanced. These results show that the absorption spectrum can be tuned by shell filling, which can be experimentally controlled by applying a gate voltage. This is particularly true for the ZZ transitions in the tera-hertz range, which can be turned off by either emptying/filling the shell $\Delta N_{deg} = \pm 7$ or at half filling. At half filling, electron exchange leads to spin polarization, with each state of the shell filled by a spin polarized electron. Since photons do not flip electron spin, no intra-shell transitions are allowed and the magnetic moment of graphene quantum dot is directly reflected in the ZZ absorption spectrum.

5.3.3 Terahertz spectroscopy of degenerate shell

In Fig. 5.5, we study the transitions for $\Delta N_{deg} = 0, \pm 1$ in detail. Figure 5.5(b) shows the lack of absorption for half-filled spin-polarized shell. The right hand side illustrates the fact that photons pass through since they are not able to induce electronic transitions and be absorbed. For $\Delta N_{deg} = -1$, Fig. 5.5(c), one electron is removed creating a hole in the spin polarized shell. Thus, the absorption spectrum corresponds to transitions from ground state to optically allowed excited states of the hole. The absorption spectrum for an additional electron, $\Delta N_{deg} = +1$, shown in Fig. 5.5(a), is dramatically different. The addition (but not subtraction) of an electron depolarizes the spins of all electrons present, with total spin of the ground state $S = 0$. The strongly correlated ground state has many configurations, which effectively allow for many transitions of the spin-up and spin-down electrons. This asymmetry in

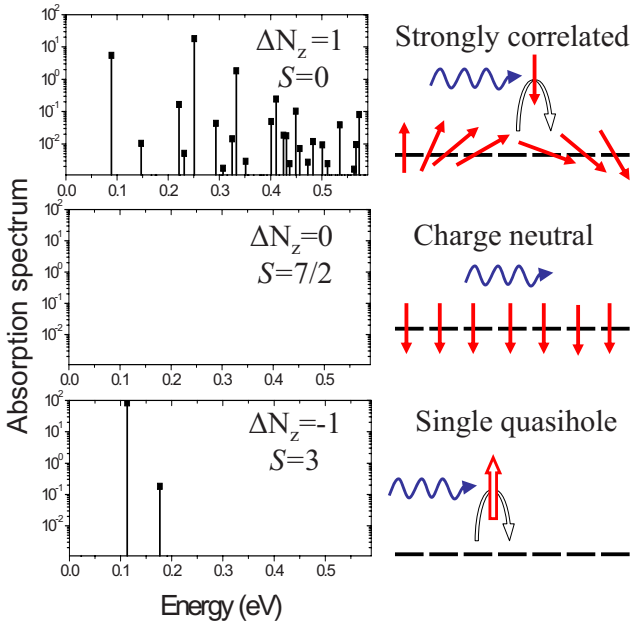

Figure 5.5: On the left: Excitonic absorption spectrum in arbitrary units at $\Delta N_{deg} = -1, 0, 1$. Corresponding ground state spins are $S = 3$ (fully polarized), $S = 7/2$ (fully polarized), and $S = 0$ (completely depolarized), respectively. On the right: The schematically representation of the physics involved in optical transitions.

the terahertz absorption spectra allows for the optical detection of charge of the quantum dot and correlated electron states in the degenerate electronic shell.

Chapter 6

Conclusions

In this thesis, I present the theoretical results describing the electronic and optical properties of graphene nanostructures. They are of significant interest not only from a scientific point of view but also due to outstanding properties with potential applications in nanoelectronics. We focus here on the analysis of graphene quantum dots as a function of size, shape, type of edges and charging. We started from a detailed description of single particle energy spectra by using the tight-binding model in a nearest neighbors approximation. In chapter 2, we have shown that as a result of size-quantization effects, the energy gap at the Fermi level opens. The magnitude of the energy gap can be controlled by the size of the dot but depends also on the type of edges in the system. We noticed similar energy spectra for both hexagonal and triangular quantum dots with armchair edges with a similar number of atoms, which suggests lack of shape dependence on the electronic properties. On the other hand, zigzag edges lead to an appearance of edge states in the vicinity of the Fermi energy. In TGQDs the edge states collapse to the zero-energy shell separated by the energy gap from the rest of the spectrum. We investigated TGQDs in detail in Section 2.2. We have shown a relation between a degree of the zero-energy degeneracy and a number of atoms belonging to each sublattice in a honeycomb graphene lattice. We proved that the degeneracy is proportional to the number of atoms on one edge of the triangle. We have derived an analytical solutions for eigenstates with energy E=0 for arbitrary size systems by solving singular eigenvalue problem of TB Hamiltonian. Next, we have classified energy levels in TGQDs according to irreducible representations of the C_{3v} symmetry group. We also considered mesoscopic quantum rings with triangular and hexagonal shapes. In TGQRs, the zero-energy degeneracy, opposite to TGQDs, is not related to the size of the system, but is determined by the width of the ring. On the other hand, in the thinnest hexagonal rings six-level degenerate shell

appears in TB energy spectrum. We explained this behavior by analyzing the evolution of the energy spectra from six independent ribbons to a ring, by slowly turning on the hopping integral between neighboring ribbons.

The next step in our studies was the inclusion of electron-electron interactions. In Chapter 3, we started from writing the many-body Hamiltonian in the second quantization form. It consists of single particle and many-body Coulomb terms. Coulomb matrix elements have been calculated by using Slater p_z orbitals localized on atomic sites of a honeycomb graphene lattice. All direct and exchange terms, and all scattering terms up to next-nearest neighbors were obtained. In Section 3.4, the many-body Hamiltonian in Hartree-Fock mean-field (MF) approximation was presented. A convenient form of HF Hamiltonian combined with TB Hamiltonian, suitable for graphene nanostructures was derived. The mean-field Hubbard model, HF Hamiltonian with an inclusion of only on-site interaction term, was also obtained. Next, we went beyond MF approximation describing configuration interaction method. We have shown a method of constructing of the many-body basis set built of configurations of electrons distributed on single particle energy levels. A Hamiltonian matrix was divided into blocks corresponding to different projection of spin onto z-axis. An example of calculations of matrix elements was presented. This method is characterized by a large computational cost due to an exponential increase of the size of the Hilbert. We have described Lanczos method which allows to find extremal eigenvalues of large matrices with matrix elements calculated "on the fly". This avoids a problem of storing matrix elements in a memory. Additionally, we have presented a method of optimizing calculations by dividing Hamiltonian into three parts corresponding to scattering of two particles within spin up and spin down subspaces, and third term with scattering of one spin up and one spin down particle. Finally, in Section 3.6 we presented a combination of TB, HF and CI methods, which allows us to study magnetism and correlation effects in graphene nanostructures.

In Chapter 4 we investigated magnetic properties of graphene quantum dots with zigzag edges. We have mostly focused on TGQDs due to the degeneracy at the Fermi energy in a single particle TB energy spectrum. We performed analysis as a function of the filling factor of the degenerate band of edge states for different sizes. Through a full analysis of the many-body energy spectrum of structures consisting of up to 200 atoms, we have confirmed the existence of the spin polarized ground state in agreement with Lieb's theorem. By studying spin exciton binding energies, we also predicted stable magnetization for structures with more than 500 atoms. The complete spin depolarization was

observed for one electron added to the charge neutral TGQD up to a critical size. Above a critical size the maximally spin polarized charged TGQD was predicted using trion binding energy analysis. We have also shown that in small systems, three electrons/holes added to the charge neutral TGQD form the spin polarized Wigner-like molecule. We relate this fact to geometrical effects and direct long-range interaction terms. For larger systems, geometry becomes less important and for the same filling we observe a spin depolarization as a result of correlations. We have also compared fully interacting model with Hubbard and extended Hubbard models. While qualitative agreement for the charge neutral system was observed, the effect of correlations can be described only with an inclusion of all direct long-range, exchange and scattering interaction terms. The edge reconstruction and the stability of zigzag edges were investigated using density functional *ab initio* methods. It was shown that hydrogen passivation stabilizes zigzag edges and *ab initio* methods do give maximally spin polarized passivated charge neutral triangles.

In Section 4.2, we described the magnetic properties and the role of correlations in triangular graphene rings. The TGQR structures exhibit the magnetic moment due to the presence of a degenerate band of states at the Fermi level. We have shown by using a mean-field Hubbard model that the total magnetization of the system is determined by the width of the structure. For TGQR with a small inner hole, only the outer edges are spin polarized, similarly to full triangle results. However, as the size of the hole is increased, the inner edges become spin polarized as well, showing antiferrimagnetic configurations. We show that TGQR with a large hole can be treated as a system consisting of three spin polarized corners connected by antiferrimagnetic ribbons. Designing structures with a given width enables us to obtain systems with arbitrary magnetic moment, opening the possibility of using TGQR in designing spintronic devices. The robustness of the total spin formation to charging is assessed. In charged graphene rings, correlation effects are found to play a role, affecting the energy required to flip a spin for different filling factors. In Section 4.3, we analyzed magnetic properties and electronic correlations in gated hexagonal mesoscopic quantum rings with zigzag edges as a function of size and number of added electrons. For the half-filling of the degenerate shell in sufficiently large ring, maximal polarization of the ground state is predicted. Away from the half filling, the correlation effects appear and the ground-state total spin alternates between maximal polarization and complete depolarization.

In chapter 5 we have studied optical properties of graphene quantum dots as a function of the size, shape and type of edges. For quantum dots with armchair

edges, the energy gap changes from $\sim$ eV for few nanometer size systems to $\sim$ meV for micrometer size structures. In an infinite limit the energy gap closes restoring the energy spectra of graphene. For quantum dots with zigzag edges, edges states are present. They are responsible for a rapid decrease of the energy gap in the hexagonal shape structure. On the other hand, in TGQDs due to a collapse of edge states to the degenerate shell on the Fermi level, the energy gap between the valence and the conduction band reveals similar behavior to that for structures with armchair edges. Next, in our studies the effect of electron-electron and electron-hole final state interactions in TGQDs is included. The change of the carrier density, and equivalently population of the degenerate shell, influence allowed optical transitions. Hence, by use of a gate voltage, one can control optical transitions simultaneously in the tera-Hertz, visible and UV spectral ranges.

Acknowledgment: This work was done in collaboration with and guidance of Devrim Guclu, and in collaboration with Oleksander Voznyy and Marek Korkusinski of Quantum Theory Group, IMS NRC.

Bibliography

[1] P. R. Wallace, Phys. Rev. **71**, 622 (1947).

[2] J. W. McClure, Phys. Rev. **108**, 612 (1957).

[3] J. C. Slonczewski and P. R. Weiss, Phys. Rev. **109**, 272 (1958).

[4] G. W. Semenoff, Phys. Rev. Lett. **53**, 2449 (1984).

[5] D. Haldane, Phys. Rev. Lett. **61**, 2015 (1988).

[6] E. J. Mele and J. J. Ritsko, Phys. Rev. Lett. **43**, 68 (1979).

[7] M. S. Dresselhaus and G. Dresselhaus, Adv. Phys. **30**, 139 (1981).

[8] D. M. Hoffman, R. E. Heinz, G. L. Doll, and P. C. Eklund, Phys. Rev. B **32**, 1278 (1985).

[9] J. Kouvetakis, R. B. Kaner, M. L. Sattler, and N. Bartlett, J. Chem. Soc., Chem. Commun **1986**, 1758 (1986).

[10] M. S. Dresselhaus, G. Dresselhaus, J. E. Fisher, Phys. Rev. B **15**, 3180 (1977).

[11] R. C. Tatar and S. Rabii, Phys. Rev. B **25**, 4126 (1982).

[12] D. P. DiVincenzo and E. J. Mele, Phys. Rev. B **29**, 1685 (1984).

[13] J. Blinowski, N. H. Hau, C. Rigaux, J. P. Vieren, R. Le Toullec, G. Furdin, A. Herold, and J. Melin, J. Phys. (Paris) **41**, 47 (1980).

[14] D. M. Hoffman, P. C. Eklund, R. E. Heinz, P. Hawrylak, and K. R. Subbaswamy, Phys. Rev. B **31**, 3973 (1985).

[15] P. Hawrylak, Solid State Com. **63**, 241 (1987).

[16] K. W.-K. Shung and G. D. Mahan, Phys. Rev. B **38**, 3856 (1988).

[17] H. P. Boehm, A. Clauss, G. O. Fischer, and U. Hofmann, Anorg. Allg. Chem. **316**, 119 (1962).

[18] H. P. Boehm, R. Setton, and E. Stumpp, Carbon **24**, 241 (1986).

[19] J. T. Grant, and T.W. Haas, Surf. Sci. **21**, 76 (1970).

[20] J. M. Blakely, J. S. Kim, and H. C. Potter, J. Appl. Phys. **41**, 2693 (1970).

[21] A. J. van Bommel, J. E. Crombeen, and A. van Tooren, Surf. Sci. **48**, 463 (1975).

[22] A. Nagashima, K. Nuka, K. Satoh, H. Itoh, T. Ichinokawa, C. Oshima, and S. Otani, Surf. Sci. **287-288**, 609 (1993).

[23] K. Seibert, G. C. Cho, W. Kütt, H. Kurz, D.H. Reitze, J. I. Dadap, H. Ahn, M. C. Downer, and A. M. Malvezzi, Phys. Rev. B **42**, 2842 (1990).

[24] Ohashi, Y., T. Koizumi, T. Yoshikawa, T. Hironaka, and K. Shiiki, TANSO **180**, 235 (1997).

[25] M. Müller, C. Kübel, and K. Müllen, Chem. Eur. J. **4**, 2099 (1998).

[26] N. Tyutyulkov, G. Madjarova, F. Dietz, and K. Müllen, J. Phys. Chem. B **102**, 10183 (1998).

[27] X. Lu, M. Yu, H. Huang and R. S Ruoff, Nanotechnology **10**, 269 (1999).

[28] K. S. Novoselov, A. K. Geim, S. V. Morozov, D. Jiang, Y. Zhang, S. V. Dubonos, I. V. Grigorieva, A. A. Firsov, Science **306**, 666 (2004).

[29] A. C. Ferrari, J. C. Meyer, V. Scardaci, C. Casiraghi, M. Lazzeri, F. Mauri, S. Piscanec, D. Jiang, K. S. Novoselov, S. Roth, and A. K. Geim, Phys. Rev. lett. **97**, 187401 (2006).

[30] K. S. Novoselov, A. K. Geim, S. V. Morozov, D. Jiang, M. I. Katsnelson, I. V. Grigorieva, S. V. Dubonos, and A. A. Firsov, Nature **438**, 197 (2005).

[31] A. K. Geim, Rev. Mod. Phys. **83**, 851 (2011).

[32] Y. Zhang, Y. W. Tan, H. L. Stormer, and P. Kim, Nature **438**, 201 (2005).

[33] K. S. Novoselov, Z. Jiang, Y. Zhang, S. V. Morozov, H. L. Stormer, U. Zeitler, J. C. Maan, G. S. Boebinger, P. Kim, A. K. Geim, Science **315**, 1379 (2007).

[34] K. S. Novoselov and A. K. Geim, Nature **6**, 183 (2007).

[35] M. L. Sadowski, G. Martinez, M. Potemski, C. Berger, and W. A. de Heer, Phys. Rev. Lett. **97**, 266405 (2006).

[36] M. I. Katsnelson, K. S. Novoselov, and A. K. Geim Nature Phys. **2**, 620 (2006).

[37] M. I. Katsnelson, Materials Today **10**, 20-27 (2007).

[38] A. F. Young and P. Kim, Nature Phys. **5**, 222 (2009).

[39] N. Stander, B. Huard, and D. Goldhaber-Gordon, Phys. Rev. Lett. **102**, 026807 (2009).

[40] Y. Lin, K. A. Jenkins, A. Valdes-Garcia, J. P. Small, Damon B. Farmer, and P. Avouris, Nano Lett. **9**, 422 (2009).

[41] K. S. Kim, Y. Zhao, H. Jang, S. Y. Lee, J. M. Kim, K. S. Kim, J.-H. Ahn, P. Kim, J.-Y. Choi, and B. H. Hong, Nature **457**, 706 (2009).

[42] F. Xia, T. Mueller, Y. Lin, A. Valdes-Garcia and P. Avouris, Nature Nanotechnology **4**, 839 (2009).

[43] T. Mueller, F. Xia, and P. Avouris, Nature Photon. **4**, 297 (2010).

[44] T. Ihn, J. Güttinger, F. Molitor, S. Schnez, E. Schurtenberger, A. Jacobsen, S. Hellmüller, T. Frey, S. Dröscher, C. Stampfer, K. Ensslin, Materials Today **44**, 20-27 (2010).

[45] J. C. Meyer, A. K. Geim, M. I. Katsnelson, K. S. Novoselov, T. J. Booth, and S. Roth, Nature **446**, 60 (2007).

[46] K.I. Bolotin, K.J. Sikes, Z. Jiang, M. Klimac, G. Fudenberg, J. Hone, P. Kim, H.L. Stormer, Solid State Comm. **146**, 351 (2008).

[47] K. I. Bolotin, K. J. Sikes, J. Hone, H. L. Stormer, and P. Kim, Phys. Rev. Lett. **101**, 096802 (2008).

[48] S.V. Morozov, K. S. Novoselov, M. I. Katsnelson, F. Schedin, D. C. Elias, J. A. Jaszczak, and A. K. Geim, Phys. Rev. Lett. **100**, 016602 (2008).

[49] R. R. Nair, P. Blake, A. N. Grigorenko, K. S. Novoselov, T. J. Booth, T. Stauber, N. M. R. Peres, A. K. Geim, Science **320**, 1308 (2008).

[50] S. Bae, H. K., Y. Lee, X. Xu, J.-S. Park, Y. Zheng, J. Balakrishnan, T. Lei, H. R. Kim, Y. I. Song, Y.-J. Kim, K. S. Kim, B. Özyilmaz, J.-H. Ahn, B. H. Hong, and S. Iijima, Nature Nanotechnology **5**, 574 (2010).

[51] Vladimir Fal'ko, Nature **3**, 151 (2007).

[52] B. Trauzettel, D. V. Bulaev, D. Loss, and G. Burkard, Nature **3**, 192 (2007).

[53] A. Rycerz, J. Tworzydlo and C. W. J. Beenakker, Nature Phys. **3**, 172 (2007).

[54] F. Schedin, A. K. Geim, S. V. Morozov, E. W. Hill, P. Blake, M. I. Katsnelson, and K. S. Novoselov, Nature **6**, 652 (2007).

[55] A. Reina, X. Jia, J. Ho, D. Nezich, H. Son, V. Bulovic, M. S. Dresselhaus, and J. Kong, Nano Lett. **9**, 30 (2009).

[56] X. Li, W. Cai, J. An, S. Kim, J. Nah, D. Yang, R. Piner, A. Velamakanni, I. Jung, E. Tutuc, S. K. Banerjee, L. Colombo, R. S. Ruoff, Science **324**, 1312 (2009).

[57] X. Li, C. W. Magnuson, A. Venugopal, J. An, J. W. Suk, B. Han, M. Borysiak, W. Cai, A. Velamakanni, Y. Zhu, L. Fu, E. M. Vogel, E. Voelkl, L. Colombo, and R. S. Ruoff, Nano Lett. **10**, 4328 (2010).

[58] C. Berger, Z. Song, T. Li, X. Li, A. Y. Ogbazghi, R. Feng, Z. Dai, A. N. Marchenkov, E. H. Conrad, P. N. First, and W. A. de Heer, J. Phys. Chem. B **108**, 19912 (2004).

[59] C. Berger, Z. Song, X. Li, X. Wu, N. Brown, C. Naud, D. Mayou, T. Li, J. Hass, A. N. Marchenkov, E. H. Conrad, P. N. First, W. A. de Heer, Science **312**, 1191 (2006).

[60] J. Hass, R. Feng, T. Li, X. Li, Z. Zong, W. A. de Heer, P. N. First, and E. H. Conrada, C. A. Jeffrey, C. Berger, Appl. Phys. Lett. **89**, 143106 (2006).

[61] J. Hass, F. Varchon, J. E. Millán-Otoya, M. Sprinkle, N. Sharma, W. A. de Heer, C. Berger, P. N. First, L. Magaud, and E. H. Conrad, Phys. Rev. Lett. **100**, 125504 (2008).

[62] J. Hass, W. A. de Heer, and E. H. Conrad, J. Phys.: Condens. Matter **20**, 323202 (2008).

[63] K. V. Emtsev, A. Bostwick, K. Horn, J. Jobst, G. L. Kellogg, L. Ley, J. L. McChesney, T. Ohta, S. A. Reshanov, J. Röhrl, E. Rotenberg, A. K. Schmid, D. Waldmann, H. B.Weber and T. Seyller, Nature Mater. **8**, 203 (2009).

[64] J. Borysiuk, R. Bożek, W. Strupiński, A. Wysmołek, K. Grodecki, R. Stępniewski, and J. M. Baranowski, J. Appl. Phys. **105**, 023503 (2009).

[65] J. Krupka and W. Strupiński, Appl. Phys. Lett. **96**, 082101 (2010).

[66] W. Strupiński, K. Grodecki, A. Wysmołek, R. Stępniewski, T. Szkopek, P. E. Gaskell, A. Grüneis, D. Haberer, R. Bożek, J. Krupka, and J. M. Baranowski, Nano Lett. **11**, 1786 (2011).

[67] W. S. Hummers and R. E. Offeman, J. Am. Chem. Soc. **80**, 1339 (1958).

[68] S. Stankovich, D. A. Dikin, G. H. B. Dommett, K. M. Kohlhaas, E. J. Zimney, E. A. Stach, R. D. Piner, S. T. Nguyen, and R. S. Ruoff, Nature **442**, 282 (2006).

[69] D. A. Dikin, S. Stankovich, E. J. Zimney, R. D. Piner, G. H. B. Dommett, G. Evmenenko, S. T. Nguyen, and R. S. Ruoff, Nature **448**, 457 (2007).

[70] M. J. McAllister, J. Li, D. H. Adamson, H. C. Schniepp, A. A. Abdala, J. Liu, M. Herrera-Alonso, D. L. Milius, R. Car, R. K. Prud'homme, and I. A. Aksay, Chem. Mater. **19**, 4396 (2007).

[71] S. Stankovich, D. A. Dikin, R. D. Piner, K. A. Kohlhaas, A. Kleinhammes, Y. Jia, Y. Wu, S. T. Nguyen, R. S. Ruoff, Carbon **45**, 1558 (2007).

[72] I. Jung, D. A. Dikin, R. D. Piner, and R. S. Ruoff, Nano Lett. **8**, 4283 (2008).

[73] K. S. Novoselov, D. Jiang, F. Schedin, T. J. Booth, V. V. Khotkevich, S. V. Morozov, and A. K. Geim, PNAS **102**, 10451 (2005).

[74] R. E. Peierls, Helv. Phys. Acta **7**, 81 (1934).

[75] R. E. Peierls, Ann. Inst. H. Poincare **5**, 177 (1935).

[76] L. D. Landau, E. M. Lifshitz, Statistical Physics, Part I, Pergamon, Oxford, UK, (1980).

[77] N. D. Mermin, Phys. Rev. **176**, 250 (1968).

[78] J. C. Meyer, C. Kisielowski, R. Erni, Marta D. Rossell, M. F. Crommie, and A. Zettl, Nano Lett. **8**, 3582 (2008).

[79] W. Bao, F. Miao, Z. Chen, H. Zhang, W. Jang, C. Dames and C. N. Lau, Nature Nanotech. **4**, 562 (2007).

[80] C. Lee, X. Wei, J. W. Kysar, J. Hone, Science **321**, 385 (2008).

[81] J. Scott Bunch, S. S. Verbridge, J. S. Alden, A. M. van der Zande, J. M. Parpia, H. G. Craighead, and P. L. McEuen, Nano Lett. **8**, 2458 (2008).

[82] T. J. Booth, P. Blake, R. R. Nair, D. Jiang, E. W. Hill, U. Bangert,¶ A. Bleloch, M. Gass, K. S. Novoselov, M. I. Katsnelson, and A. K. Geim, Nano Lett. **8**, 2442 (2008).

[83] N. Mingo and D. A. Broido, Phys. Rev. Lett. **95**, 096105 (2005).

[84] A. A. Balandin, S. Ghosh, W. Bao, I. Calizo, D. Teweldebrhan, F. Miao, and C. N. Lau, Nano Lett. **8**, 902 (2008).

[85] Z. Chen, Y.-M. Lin, M. J. Rooks, and P. Avouris, Physica E **40**, 228 (2007).

[86] M. Y. Han, B. Özyilmaz, Y. Zhang, and P. Kim, Phys. Rev. Lett. **98**, 206805 (2007).

[87] X. Jia, M. Hofmann, V. Meunier, B. G. Sumpter, J. Campos-Delgado, J. M. Romo-Herrera, H. Son, Y.-P. Hsieh, A. Reina, J. Kong, M. Terrones, M. S. Dresselhaus, Science **323**, 1701 (2009).

[88] M. Engelund, J. A. Fürst, A. P. Jauho, and M. Brandbyge, Phys. Rev. Lett. **104**, 036807 (2010).

[89] E. Cruz-Silva, A. R. Botello-Mendez, Z. M. Barnett, X. Jia, M. S. Dresselhaus, H. Terrones, M. Terrones, B. G. Sumpter, and V. Meunier, Phys. Rev. Lett. **105**, 045501 (2010).

[90] X. Li, X. Wang, L. Zhang, S. Lee, H. Dai, Science **319**, 1229 (2008).

[91] J. Cai, P. Ruffieux, R. Jaafar, M. Bieri, T. Braun, S. Blankenburg, M. Muoth, A. P. Seitsonen, M. Saleh, X. Feng, K. Müllen, R. Fasel, Nature **466**, 470 (2010).

[92] L. Zhi and K. Müllen, J. Mater. Chem. **18**, 1472 (2008).

[93] M. Treier, C. A. Pignedoli, T. Laino, R. Rieger, K. Müllen, D. Passerone, and R. Fasel, Nat. Chem. **3**, 61 (2010).

[94] M. L. Mueller, X. Yan, J. A. McGuire, and L. Li, Nano Lett. **10**, 2679 (2010).

[95] Y. Morita, S. Suzuki, K. Sato, and T. Takui, Nat. Chem. **3**, 197 (2011).

[96] J. Lu, P. S. E. Yeo, C. K. Gan, P. Wu, and K. P. Loh, Nat. Nanotechnol. **6**, 247 (2011).

[97] D. V. Kosynkin, A. L. Higginbotham, A. Sinitskii, J. R. Lomeda, A. Dimiev, B. K. Prince, and J. M. Tour, Nature (London) **458**, 872 (2009).

[98] C. Tao, L. Jiao, O. V. Yazyev, Y.-C. Chen, J. Feng, X. Zhang, R. B. Capaz, J. M. Tour,A. Zettl, S. G. Louie, H. Dai, and M. F. Crommie, Nat. Phys. **7**, 616 (2011).

[99] W. Jaskólski, A. Ayuela, M. Pelc, H. Santos, and L. Chico, Phys. Rev. B **83**, 235424 (2011).

[100] Y. W. Son, M. L. Cohen, and S. G. Louie, Phys. Rev. Lett. **97**, 216803 (2006).

[101] L. Pisani, J. A. Chan, B. Montanari, and N.M. Harrison, Phys. Rev. B **75**, 064418 (2007).

[102] O. V. Yazyev, R. B. Capaz, and S. G. Louie, Phys. Rev. B **84**, 115406 (2011).

[103] O. V. Yazyev, R. B. Capaz, and S. G. Louie, J. Phys.: Conf. Ser. **302**, 012016 (2011).

[104] H. Santos, A. Ayuela, W. Jaskólski, M. Pelc, and L. Chico, Phys. Rev. B **80**, 035436 (2009).

[105] L. Chico, H. Santos, A. Ayuela, W. Jaskólski, M. Pelc, and L. Brey, Acta Phys. Pol. A. **118**, 433 (2010).

[106] J. S. Bunch, Y. Yaish, M. Brink, K. Bolotin, and P. L. McEuen, Nano Lett. **5**, 287 (2005).

[107] L. A. Ponomarenko, F. Schedin, M. I. Katsnelson, R. Yang, E. W. Hill, K. S. Novoselov, and A. K. Geim, Science **320**, 356 (2008).

[108] C. Stampfer, J. Güttinger, F. Molitor, D. Graf, T. Ihn, and K. Ensslin, Appl. Phys. Lett. **92**, 012102 (2008).

[109] J. Güttinger, C. Stampfer, S. Hellmöller, F. Molitor, T. Ihn, and K. Ensslin, Appl. Phys. Lett. **93**, 212102 (2008).

[110] S. Schnez, J. Güttinger, M. Huefner, C. Stampfer, K. Ensslin, and T. Ihn, Phys. Rev. B **82**, 165445 (2010).

[111] T. Ihn, J. Güttinger, F. Molitor, S. Schnez, E. Schurtenberger, A. Jacobsen, S. Hellmüller, T. Frey, S. Dröscher, C. Stampfer, and K. Ensslin, Mater. Today **13**, 44 (2010).

[112] F. Molitor, J. Güttinger, C. Stampfer, S Dröscher, A. Jacobsen, T. Ihn and K. Ensslin, J. Phys.: Condens. Matter **23**, 243201 (2011).

[113] S. Schnez, F. Molitor, C. Stampfer, J. Güttinger, I Shorubalko, T. Ihn, and K. Ensslin, Appl. Phys. Lett. **94**, 012107 (2009).

[114] T. Ihn, S. Gustavsson, U. Gasser, B. Küng, T. Müller, R. Schleser, M. Sigrist, I. Shorubalko, R. Leturcq, and K. Ensslin, Solid State Commun. **149**, 1419 (2009).

[115] J. Güttinger, C. Stampfer, F. Libisch, T. Frey, J. Burgdörfer, T. Ihn, and K. Ensslin, Phys. Rev. Lett. **103**, 046810 (2009).

[116] J. G̈ttinger, T. Frey, C. Stampfer, T. Ihn, and K. Ensslin, Phys. Rev. Lett. **105**, 116801 (2010).

[117] S. K. Hämäläinen, Z. Sun, M. P. Boneschanscher, A. Uppstu, M. Ijäs, A. Harju, D. Vanmaekelbergh, and P. Liljeroth, Phys. Rev. Lett. **107**, 236803 (2011).

[118] D. Subramaniam, F. Libisch, Y. Li, C. Pauly, V. Geringer, R. Reiter, T. Mashoff, M. Liebmann, J. Burgdörfer, C. Busse, T. Michely, R. Mazzarello, M. Pratzer, and M. Morgenstern, Phys. Rev. Lett. **108**, 046801 (2012).

[119] L. Ci, Z. Xu, L. Wang, W. Gao, F. Ding, K. F. Kelly, B. I. Yakobson, and P. M. Ajayan, Nano Res. **1**, 116 (2008).

[120] L. C. Campos, V. R. Manfrinato, J. D. Sanchez-Yamagishi, J. Kong, and P. Jarillo-Herrero, Nano Lett. **9**, 2600 (2009).

[121] Y. Niimi, T. Matsui, H. Kambara, K. Tagami, M. Tsukada, and H. Fukuyama, Appl. Surf. Sci. **241**, 43 (2005).

[122] Y. Kobayashi, K.-I. Fukui, T. Enoki, K. Kusakabe, and Y. Kaburagi, Phys. Rev. B **71**, 193406 (2005).

[123] Y. Kobayashi, K. Fukui, T. Enoki, and K. Kusakabe, Phys. Rev. B **73**, 125415 (2006).

[124] Y. Niimi, T. Matsui, H. Kambara, K. Tagami, M. Tsukada, and H. Fukuyama, Phys. Rev. B **73**, 085421 (2006).

[125] C. Tao, L. Jiao, O.V. Yazyev, Y.-C. Chen, J. Feng, X. Zhang, R.B. Capaz, J.M. Tour, A. Zettl, S.G. Louie, H. Dai, and M.F. Crommie, Nature Phys. **7**, 616 (2011).

[126] Y. You, Z. Ni, T. Yu, and Z. Shen, Appl. Phys. Lett. **93**, 163112 (2008).

[127] B. Krauss, P. Nemes-Incze, V. Skakalova, L. P. Biró, K. von Klitzing, and J. H. Smet, Nano Lett. **10**, 4544 (2010).

[128] S. Neubeck, Y. M. You, Z. H. Ni, P. Blake, Z. X. Shen, A. K. Geim, and K. S. Novoselov, Appl. Phys. Lett. **97**, 053110 (2010).

[129] A. Chuvilin, J. C Meyer, G. Algara-Siller, and U. Kaiser, New J. Phys. **11**, 083019 (2009).

[130] Ç. Ö. Girit, J. C. Meyer, Rolf Erni, M. D. Rossell, C. Kisielowski, L. Yang, C. Park, M. F. Crommie, M. L. Cohen, S. G. Louie, A. Zettl, Science **323**, 1705 (2009).

[131] P. Koskinen, S. Malola, and H. Häkkinen, Phys. Rev. Lett. **101**, 115502 (2008).

[132] P. Koskinen, S. Malola, and H. Häkkinen, Phys. Rev. B **80**, 073401 (2009).

[133] K. Nakada, M. Fujita, G. Dresselhaus, and M. S. Dresselhaus, Phys. Rev. B **54**, 17954 (1996).

[134] M. Fujita, K. Wakabayashi, K. Nakada, and K. Kusakabe, J. Phys. Soc. Jpn. **65**, 1920 (1996).

[135] Y. Son, M. L. Cohen, and S. G. Louie, Nature **444**, 347 (2006).

[136] T. Yamamoto, T. Noguchi, and K.Watanabe, Phys. Rev. B **74**, 121409 (2006).

[137] M. Ezawa, Phys. Rev. B **73**, 045432 (2006).

[138] M. Ezawa, Phys. Rev. B **76**, 245415 (2007).

[139] J. Fernandez-Rossier and J. J. Palacios, Phys. Rev. Lett. **99**, 177204 (2007).

[140] J. Akola, H. P. Heiskanen, and M. Manninen, Phys. Rev. B **77**, 193410 (2008).

[141] W. L. Wang, S. Meng, and E. Kaxiras, Nano Lett. **8**, 241 (2008).

[142] M. Manninen, H. P. Heiskanen, and J. Akola, Eur. Phys. J. D **52**, 143–146 (2009).

[143] W. L. Wang, O. V. Yazyev, S. Meng, and E. Kaxiras, Phys. Rev. Lett. **102**, 157201 (2009).

[144] A. D. Güçlü, P. Potasz, O. Voznyy, M. Korkusinski, and P. Hawrylak, Phys. Rev. Lett. **103**, 246805 (2009).

[145] P. Potasz, A. D. Güçlü, and P. Hawrylak, Phys. Rev. B **81**, 033403 (2010).

[146] K. Wakabayashi, M. Sigrist, and M. Fujita, J. Phys. Soc. Jpn. **67**, 2089 (1998).

[147] A. Yamashiro, Y. Shimoi, K. Harigaya, and K. Wakabayashi, Phys. Rev. B **68**, 193410 (2003).

[148] L. Yang, M. L. Cohen, and S. G. Louie, Phys. Rev. B **101**, 186401 (2008).

[149] F. Cervantes-Sodi, G. Csanyi, S. Piscanec, and A. C. Ferrari, Phys. Rev. B **77**, 165427 (2008).

[150] M. Fernández-Rossier Phys. Rev. B **77**, 075430 (2008).

[151] J. J. Palacios, J. Fernández-Rossier, and L. Brey, Phys. Rev. B **77**, 195428 (2008).

[152] J. Jung and A. H. MacDonald, Phys. Rev. B **79**, 235433 (2009).

[153] D. Soriano and J. Fernández-Rossier, Phys. Rev. B **82**, 161302(R) (2010).

[154] Z. Z. Zhang, K. Chang, and F. M. Peeters, Phys. Rev. B **77**, 235411 (2008).

[155] A. D. Güçlü, P. Potasz, and P. Hawrylak, Phys. Rev. B **82**, 155445 (2010).

[156] M. Ezawa, Phys. Rev. B **77**, 155411 (2008).

[157] M. R. Philpott, F. Cimpoesu, and Y. Kawazoe, Chem. Phys. **354**, 1 (2008).

[158] H. P. Heiskanen, and M. Manninen, J. Akola, New J. Phys. **10**, 103015 (2008).

[159] D. P. Kosimov, A. A. Dzhurakhalov, and F. M. Peeters, Phys. Rev. B **81**, 195414 (2008).

[160] M. Ezawa, Phys. Rev. B **81**, 201402 (2010).

[161] M. Ezawa, Phys. E **42**, 703 (2010).

[162] H. Sahin, R. T. Senger, and S. Ciraci, J. Appl. Phys. **108**, 074301 (2010).

[163] I. Romanovsky, C. Yannouleas, and U. Landman, Phys. Rev. B **83**, 045421 (2011).

[164] M. Zarenia, A. Chaves, G. A. Farias, and F. M. Peeters, Phys. Rev. B **84**, 245403 (2011).

[165] P. Potasz, A. D. Güçlü, A. Wójs, and P. Hawrylak, Phys. Rev. B **85**, 075431 (2012).

[166] L. Brey and H. A. Fertig, Phys. Rev. B **73**, 195408 (2006).

[167] L. Brey and H. A. Fertig, Phys. Rev. B **73**, 235411 (2006).

[168] M. V. Berry and R. J. Mondragon, Proc. R. Soc. Lond. A **412**, 53-74 (1987).

[169] P. Recher and B. Trauzettel, Nanotechnology **21**, 302001 (2010).

[170] K. A. Ritter and J. W. Lyding, Nat Mater. **8**, 235 (2009).

[171] M.S. Dresselhaus, G. Dresselhaus, and A. Jorio, Group Theory. Application to the Physics of Condensed Matter, Springer-Verlag, Berlin, (2008).

[172] P. Potasz, A. D. Güçlü, O. Voznyy, J. A. Folk, and P. Hawrylak, Phys. Rev. B **83**, 174441 (2011).

[173] P. Potasz, A. D. Güçlü, and P. Hawrylak, Phys. Rev. B **82**, 075425 (2010).

[174] J. Hubbard, Proc. R. Soc. London Ser. A **276**, 238 (1963).

[175] K. A. Chao, J. Spałek, and A. M. Oleś, J. Phys. C: Solid State Phys. **10**, L271 (1977).

[176] K. A. Chao, J. Spałek, and A. M. Oleś, Phys. Rev. B **18**, 3453 (1978).

[177] P. Hawrylak A. Wójs, and J. A. Brum, Phys. Rev. B **55**, 11397 (1996).

[178] R. B. Laughlin Phys. Rev. Lett. **50**, 1395 (1983).

[179] B. J. Ransil, Rev. Mod. Phys. **32**, 245 (1960).

[180] S. Reich, J. Maultzsch, and C. Thomsen, and P. Ordejón, Phys. Rev. B **66**, 035412 (1960).

[181] O. V. Yazyev, Phys. Rev. Lett. **101**, 037203 (2008).

[182] A. Wensauer, M. Korkusiński, and P. Hawrylak, Solid State Commun. **130**, 115 (2004).

[183] C. Lanczos, Journal of the National Bureau of Standards, **45**, 255 (1950).

[184] B. Wunsch T. Stauber, and F. Guinea, Phys. Rev. B **77**, 035316 (2008).

[185] I. Romanovsky, Y. Yannouleas, and U. Landman, Phys. Rev. B **79**, 075311 (2009).

[186] E. H. Lieb, Phys. Rev. Lett. **62**, 1201 (1989).

[187] J. Spałek, Quantum phase transitions and critical phenomena: a new type of behavior of matter, Postępy Fizyki **57**, 200 (2006).

[188] O. Voznyy, A. D. Güçlü, P. Potasz, and P. Hawrylak, Phys. Rev. B **83**, 165417 (2011).

[189] J. M. Soler, E. Artacho, J. D. Gale, A. Garcia, J. Junquera, P. Ordejon, and D. Sanchez-Portal, J. Phys. Condens. Matter **14**, 2745 (2002).

[190] J. P. Perdew, K. Burke, and M. Ernzerhof, Phys. Rev. Lett. **77**, 3865 (1996).

[191] D. K. Armani, T. J. Kippenberg, S. M. Spillane, and K. J. Vahala, Nature (London) **421**, 925 (2003).

[192] F. Wang, Y. B. Zhang, C. S. Tian, C. Girit, A. Zettl, M. Crommie, and Y. R. Shen, Science **320**, 206 (2008).

[193] Z. Q. Li, E. A. Henriksen, Z. Jiang, Z. Hao, M. C. Martin, P. Kim, H. L. Stormer, and D. N. Basov, Nat. Phys. **4**, 532 (2008).